THE PHYSICS BEHIND AND BIOSENSING APPLICATIONS OF RESONANT MICRO- AND NANOMECHANICAL SENSORS

A Dissertation

Presented to the Faculty of the Graduate School

of Cornell University

in Partial Fulfillment of the Requirements for the Degree of

Doctor of Philosophy

by

Philip Sutton Waggoner

May 2010

THE PHYSICS BEHIND AND BIOSENSING APPLICATIONS OF RESONANT MICRO- AND NANOMECHANICAL SENSORS

Philip Sutton Waggoner, Ph.D.

Cornell University 2010

The research presented herein focuses on the use of micro- and nanoelectromechanical systems (MEMS/NEMS) as mechanical resonators employed as sensors. The thesis describes the physical mechanisms underlying their use as sensors and demonstrates their utility in biosensing applications. This field is developing in the wake of the inception and widespread propagation of MEMS devices and scanned probe microscopies like atomic force or scanning tunneling microscopy. Recently there has been growing interest in their application to biological systems and the detection of low concentrations of biomolecules, where they could enable novel or deeper understandings of these systems or the onset and progression of disease. In order to push the limits of sensitivity to such levels, a full understanding of the sensing mechanisms is needed which, once attained, will shed light on appropriate sensor design parameters, materials, functional pattering, and the use of higher resonant modes.

Two key themes that emerge from this work are the effect of device geometry and device optimization for use as biosensors. Especially important are the demonstrated applications of non-cantilever geometries and the results suggesting that these devices are also more sensitive and quantitative than cantilevers when the number of bound analytes on a device becomes very small. For biosensing applications, a “secondary mass labeling” technique has been developed that greatly improves device sensitivity to lightweight biomolecules specifically bound to the resonant sensors by effectively amplifying the mass of the analyte.

After motivating the use of these sensors and providing a detailed discussion of the technology in general in Chapters 1 and 2, the experimental details of device fabrication and use are described in Chapter 3. Chapter 4 features in-depth discussion of the mathematical derivations and physics underlying the operation of these devices as sensors. Then in Chapter 5, the preparation of these devices for biosensing is described, and two realistic examples are demonstrated for the detection of prion proteins and prostate specific antigen. Together with the high device yield and rapid readout of devices, the results presented herein show great promise for real applications of this technology in medicine or other applications.

BIOGRAPHICAL SKETCH

Philip Sutton Waggoner was born in 1983 in rural Virginia. At the age of 4, he moved to Springfield, IL where he stayed until graduating from high school in Pleasant Plains, IL. Because of the small size of his school district, he ended up going to school with most of the same people from Kindergarten to senior year, and graduated 2nd in his class of 88 in 2001. Thankfully he did not give a sad, depressing "We're all going to miss high school and each other so much" commencement speech, rather he found a way to compare high school to Star Wars and the principals to the Emperor and Darth Vader. Philip was quite active with Boy Scouts throughout high school and was able to reach the highest rank of Eagle Scout just before turning 18.

After high school, he was accepted into the Materials Science and Engineering program at the University of Illinois. In May of 2004, between his junior and senior years, he married his wife Amanda—they first met in church and kindergarten around age 5, and grew up together as merely acquaintances. Their mothers were friends, and their brothers had fought in school and Sunday school but had also become friends. Only after she had moved away and been gone for over 3 years did they start dating. There were no awkward moments meeting the other one's family, as they were already good friends through their church, boy scouts, and other pastimes.

Once deciding upon graduate school as the next step in his career, Philip applied and was accepted to multiple Ph.D. programs across the country in Materials Science or Applied Physics. Ultimately, he chose Cornell for its superior reputation in nanotechnology research, the newly constructed cleanroom facility, as well as the breadth, flexibility, and collaborative nature of Cornell, especially within the School of Applied and Engineering Physics. In addition, he did a senior research project on MEMS and NEMS sensor technologies, which drew his attention to Prof. Harold

Craighead's leading research in the field. Owing to a fortunate aligning of circumstances, interests, and opportunities, he went to Cornell and was able to join Harold's research group very quickly, thanks in part to his National Defense Science and Engineering Graduate Fellowship.

In September of 2006, Philip and Amanda had a son Jack, who was born with many unexpected medical complications associated with a condition called CHARGE Syndrome. After a three month stay in neonatal intensive care and several surgeries, Jack was able to come home from the hospital. The doctors said he would be deaf, blind and unable to walk or talk. Jack has since broken all of those negative prognoses and continues to amaze his parents, doctors, and therapists. While raising him has never been easy, it has been a very rewarding process, and he is currently communicating through sign language and is also beginning to speak a few words. Another addition to the family—a daughter, Claire—arrived in May of 2009. While having one child, let alone two, in a graduate student family is certainly not a commonly taken path, Philip and Amanda do not regret a single thing about it and will always fondly look back upon this part of their lives as a young family in Ithaca.

To my wife, Amanda

ACKNOWLEDGEMENTS

First and foremost I want to thank my wonderful wife Amanda, who has supported me every step of the way, showing amazing strength that neither she nor I knew she possessed. Even after our son, Jack, was born with CHARGE Syndrome in September of 2006 and required many surgeries while spending the first three months of his life in the neonatal ICU, she was there for me. I had to take my qualifying exams within just weeks of Jack coming home from the hospital for the first time with a feeding tube and other medical complications, and she took care of both of us, even as I studied more than anyone should really study for something. I passed all of the exams on that first try, with her help and by the grace of God. Even now as I think about and write my thesis, she is supporting me, Jack, and our newborn daughter Claire, born in May of 2009. Through it all, she has been understanding and supportive, even during those times when I needed to spend more than 24 hours straight in the lab running some tedious experiment or I had to go back in to campus to the cleanroom in the middle of the night because that was either the only time available on the SEM for weeks or it was the only time of day I could find and get a hold of Rob Ilic. And she has always been willing to lend an ear to hear about my troubles or triumphs in the lab, even though it usually causes her eyes to glaze over and her mind to drift off to somewhere more interesting. In all honesty, I would not be here writing a doctoral thesis without Amanda, who encouraged me to follow my dreams of doing research and to get my Ph.D., even when I wasn't sure I could get into grad schools.

There are so many others to thank as well. I am exceedingly grateful to my undergraduate research advisor and mentor, Prof. John Weaver. John took me under his wings early in my undergraduate studies and offered me the opportunity to do

some research in his lab. I ended up spending three years there and was able to be an author on 4 papers (even one first-authored!), go to several conferences, and become proficient in ultra high vacuum technology and transmission electron microscopy. I truly enjoyed my time spent working for John, with his unique sense of humor, conversations over the morning cups of coffee in the lab, and even the roughly 1831 drafts each paper would go through before submitting to a journal. More importantly, it was during this time that I discovered that scientific research is not a freshman chemistry lab (which I thoroughly hated) where we try to measure some value that was determined 100s of years ago nor is it that tedious ceramic pellet sintering experiment in the junior level Materials Science lab course at Illinois. Rather, research is a profession in which boundaries are pushed, those difficult questions we avoided as undergrads are instead attacked head on, we strive to improve society through a fuller understanding of our universe, and we boldly dive into the unknown armed only with our creativity, ingenuity, and the groundwork laid by scientists and engineers before us. Research was something I wanted to be a part of.

I of course would not be at this point in my education and career without the guidance and support of my Ph.D. advisor, Professor Harold Craighead, who graciously accepted the excited, young, and determined student I was into his group. I have always been so impressed by his intuition and how well he can analyze situations, experiments, and results, even when he may not be very familiar with the subject matter. I would be very happy to come away from grad school inheriting just a fraction of these qualities. I have learned a great deal from Harold, and his guidance and advice have been and will continue to be invaluable. In addition, he has always been supportive and understanding of my situation in raising a child with special needs and the frequent hospitalizations that often accompany such children. As a research advisor, Harold's "hands-off" approach has been a great asset and allowed me to take

advantage of my self-motivation, tap into my creativity, and follow my own research ideas and interests. Some of my favorite research and experiments have come from spontaneous ideas and serendipitous observations. My only regret would be that I was not able to achieve Harold's gold standard of a tricorder (for the non-Trekkies, it is a handheld sensor that can detect *anything!*).

I also want to thank my fellow graduate students and colleagues that I have worked with during my graduate studies, and I hope that both our friendships as well as our professional relationships will continue long into the future. I would like to thank Keith Aubin, in whose research footsteps I have followed, for transferring a great a deal of knowledge to me before he left for the real world, including getting me acquainted with work in the cleanroom and leaving me the building blocks for automating the measurement of resonator arrays, which has saved an immeasurably large amount of time and enabled me to do the amount of work I have in my Ph.D. research. Ben Cipriany and Christine Tan both joined the group at the same time I did and both have been great friends and great colleagues. I've learned a lot from them, being Electrical Engineering and Biomedical Engineering students, respectively, as they represent the multidisciplinary and collaborative environment of Cornell Applied Physics. Christine as well as Madhukar Varshney, with whom I've worked for several years now, are largely responsible for my knowledge and understanding of biological systems that I have acquired as a student these last several years—I had previously avoided the life sciences since 10^{th} grade Anatomy and Physiology. Madhukar worked hard on optimizing and developing the surface chemistry for prion protein detection and taught me much about studying and troubleshooting surface biochemistry.

In addition, I honestly owe one of my papers to Christine, in which we studied these unique resonators with surprisingly good qualities in air. Early one morning she

was measuring devices for a different experiment we were running and serendipitously came across some unusual resonance peaks. I initially contested that the peaks were probably just noise in the system or a sign of contamination, but she was right and eventually convinced me that they were real resonances. After some investigation, we found that the chamber pressure was higher than expected. We were both surprised to have found devices with such high quality factor at these pressures, and in the end it turned out these resonators had a lot of potential for sensing applications at or near atmospheric pressure. Without Christine's hard work and her convincing me that their properties were real, I may never have noticed. This actually turned out to be one of my favorite projects that I have worked on.

I would also like to thank the American Society of Engineering Education, through which I received the National Defense Science and Engineering Graduate Fellowship (NDSEG), a 3 year fellowship that supported me during the first part of my graduate studies. Not only did this award let me skip being a grader or a teaching assistant, allowing me to jump into a research lab much sooner than usual, it also made me more appealing for professors to take me on as a graduate student. I am grateful to the ASEE for bestowing this award to me and feel honored to have received it.

All device fabrication and scanning electron microscopy was performed at the Cornell NanoScale Facility, a member of the National Nanotechnology Infrastructure Network, which is supported by the National Science Foundation. I would like to thank the staff there for their help and advice that I have received over the years. The prostate specific antigen detection project, described in Section 5.6, was supported in part by Intel Research.

Last but most definitely not least, I would like to thank my family for their support. First, I would like to thank my parents for raising me as a good kid who at one point enjoyed doing math for fun during the summer or often ended up doing his

weekend homework on Friday afternoons and nights. Despite the fact that this makes me a nerd, it led to my work ethic and my proficiency in math and other subjects, which ultimately got me into the University of Illinois and now Cornell for my degrees. I also want to thank my wife's parents, who have been encouraging and supportive of my work. I am also very grateful for their help in tough times while Jack has been hospitalized, as they have more than once come to help us take care of ourselves, retain our sanity, and allow me to continue working through difficult times.

TABLE OF CONTENTS

LIST OF FIGURES

LIST OF TABLES

CHAPTER 1

INTRODUCTION AND MOTIVATION

1.1 The Sensor Age

Although it is said our society is currently in the information age, we are also quietly in a 'sensor' age—we are constantly striving to study, understand, monitor, and control our environment. If one spends just a moment considering the sensors near and around them, it can be surprising how much is nearby. There are sensors that illuminate our path or open doors for us, literally. Thermostats are ubiquitous in homes and offices today, sensing the temperature and giving feedback to adjust the temperature. Humidifiers or dehumidifiers sense the relative humidity and similarly react appropriately. We have radar sensors which can monitor the speed of motor vehicles or baseball pitches. Breathalyzer sensors can measure the percentage of alcohol in one's system. There are sensors for radioactive materials and x-rays. There are heart rate sensors that simply stick to one's skin and oximeters that can sense blood oxygenation with a simple toe or finger fixture. Radio frequency identification tags are used with sensors present at store fronts or in distribution facilities so that companies can prevent shoplifting and keep track of the ebb and flow of inventory and shipping.

The primary agent in sustaining this sensor age is the advance of technology through innovative research, engineering, and development. In the last 10 to 20 years, there has been a groundswell of interest in and a commensurate, widespread effort to seek out technologies that would enable ultrasensitive sensing of trace materials in both macro- and microscopic environments. With the advent of chemical and

biological weapons and in the wake of terrorist attacks and the tragedy of September 11th, 2001, there is tremendous interest from the defense industry in trace detection. International governments and safety organizations are in need of such technologies, especially with growing concerns over potential global epidemics of avian or swine flu or SARS. In recent years, environmental concerns about global warming and greenhouse emissions present another market for improved sensors for gas analysis, looking for pollutants and carbon emissions at the sources.

The field of medicine has also become more dependent upon cellular and molecular sensing and is a major driving force for improving sensors. The human body provides a number of microenvironments available for study, such as blood, saliva, or urine, that could hold the answers that would enable improved diagnostics or even the ultimate limit of disease detection at its onset. Blood tests are routinely used to check for white cell counts indicating infection, testing enzyme levels looking for organ function, or monitoring cholesterol levels. Diabetes has in fact led to a gold standard of miniaturized sensors and home medicine now that patients with diabetes can monitor their blood sugar levels at home or on the go with handheld testing equipment. Ovulation and pregnancy tests are additional examples of easy-to-use and inexpensive sensors that are available for home use. The quest for early cancer diagnostics is leaning on the search for disease biomarkers, such as proteins, DNA, or cellular signals that reflect disease onset or progression. Some biomarkers have also been found to correlate with prognosis as well. In addition, pharmaceutical and epigenetic research is motivating improved sensing at a molecular level.

Now, society is investing in improved sensor technologies for all of these applications and more, with the hope that they may illuminate our path and open doors for us.

1.2 Sense and Sensitivity

In order to study these microenvironments or trace materials in our macroenvironment, some thought needs to be put into the sensors. For instance, it would not make sense to use a sensor the size of a dining room table to try to detect a part-per-billion concentration of sulfur dioxide from the air or five bacteria from a liter of lake water. The sensor needs to be considerably closer to the size of the analyte—otherwise, what device property could be significantly changed by such a small perturbation so that it would be measurable? While a weightlifter hoisting 300 kg of weight would not feel the difference if a fly were to land on the weights, an ant carrying a crumb certainly would if the same fly landed on that crumb. From another perspective, one could not detect the impedance of bacteria using alligator clips and a multimeter, rather microelectrodes are required.

These arguments lead to an important reason supporting sensor miniaturization—it is easier to detect small changes in a quantity if that quantity itself is small to begin with. Assuming that there are now sensors small enough, what quantities are important to detect and report? Device sensitivity to small changes in mass is one type of sensitivity that is intuitively comparable to macroscale measurements and would accurately describe binding of single small entities such as bacteria, viruses, nanoparticles, or individual molecules. Sensors with a very high absolute mass sensitivity could permit discrete sensing and enumeration of analytes; for instance, some micro- and nanoscale devices have demonstrated sensitivity to mass changes on the order of attograms (10^{-18} g) or less.[1-4] Sensors that work on larger scales typically measure changes in mass uniformly distributed over the sensor. As a result, sensitivities for these techniques, such as quartz crystal microbalance and surface plasmon resonance, are often discussed in terms of mass per unit area. While

this value can be translated into a value for total mass measured, the size of these devices restricts absolute mass sensitivity to the range of nanograms to picograms. However, this begs the following question to be asked: does it make sense to report the detection of 100 pg or 10 pg/mm^2 of some protein? Despite the impressively low mass, the answer should be no. Was this protein detected from a liter? A milliliter? A nanoliter? This of course points to *concentration*, which is the key quantity used in atmospheric, aqueous, and medical sensing applications when looking for some substance.

For many applications the figure of merit of a sensor system is the detectable concentration of a chemical of interest in a medium that contains mixtures of other compounds often at much higher concentrations. In these cases, the chemical specificity and affinity of the chemical binding layer are the critical and usually limiting features of a sensor. The fluid dynamics and the kinetics of analyte binding, diffusion, and transport to the receptor layer on the devices are also important.[5] It is important to realize, however, that the sensitivity of a technique is ultimately a function of much more than just the physical limits of the sensor itself.

For medical diagnostic devices, the sensitivity to a low concentration of a disease-marker compound in a body fluid is the important parameter. For example, prostate specific antigen (PSA) is currently used as a biomarker for prostate cancer at concentrations in the range of 0.1 to 10 ng/mL. In other systems, sensitivity on the order of pM or fM may be desirable. However, these low concentration target compounds are in serum or other body fluids that have other constituents at much higher concentrations. These ubiquitous biomolecules can non-specifically bind to receptor molecules or device surfaces and reduce the sensitivity of the system, if not causing false positives or negatives. Therefore, blocking chemistries and other

measures taken to reduce non-specific binding also play a significant role in determining the overall sensitivity of a sensor system.

1.3 Labeled vs. Label-free Biological Detection

As biomedical research continues to find new proteins or chemical markers associated with a disease or condition, interest grows in detecting these markers as an alternative to symptomatic diagnosis. Ideally, one would be tested for these markers periodically, giving insight into the onset of disease. In addition, developing techniques that could detect sufficiently low quantities would lead to the ultimate of early detection of disease.[6] As a result, current research in this field is focused on maximizing sensitivity, reducing false positives and negatives, and creating highly-multiplexed systems for parallel detection of any number of biomolecules of interest. Effective systems would have far-reaching impact.

A technique commonly used to improve sensitivity involves further labelling proteins or other biomolecules with radioactive species, quantum dots, fluorescent markers, enzymes, or even other biomolecules, such as antibodies or DNA and RNA aptamers.[7] These labeling schemes are then coupled with multiplexed bioassays, designed to detect an assortment of molecules. Typically, receptors with specific binding affinities to desired analytes are immobilized on a substrate, where the sample will be introduced. While these receptor-analyte systems are highly specific, interactions with other entities either by non-specific physisorption or cross-reactivity of the receptor with another biomolecule are still present and affect all types of binding assays.

Two examples of labeled detection include immunoassays, which use antibody receptors to bind their specific antigens in the sample solution, and protein microarrays,[8] used to detect protein binding to a wide variety of biological molecules. Detection is usually signaled in one of the following ways: studying the competitive binding of labeled and unlabeled analytes, using labeled molecules specific to immobilized analytes thus forming a sandwich assay, or performing an Enzyme-linked Immunosorbent Assay, or ELISA, where an enzyme-active substrate is added that changes color or fluoresces upon interaction with enzyme-linked analytes.[7] Some other examples of labeled biosensing include immunoprecipitation (IP) and yeast two-hybrid (YTH) systems.[8]

It is important to keep in mind that the definition of "label-free" is often under contention, and can mean different things. One popular version is that label-free sensors are those which do not require additional reagents, such as sandwich antibodies, labeled or unlabeled, and can detect native analyte binding alone. Another meaning refers to chemically modifying either the analyte or a secondary "label" with a fluorescent tag, biotin, or nanoparticle, for example, that could potentially interfere with the chemical activity of the molecule. While adding and detecting a secondary, specific label for an analyte is not direct, it can be more sensitive and only has the disadvantage of taking an extra step to add to the protocol that adds to time and cost. However, labeling practices that involve covalent linking to molecules, such as biotinylation or fluorescent tagging often attach these linkers to the analytes or secondary labels in a random way, which depending on the binding site(s) could interfere with the function of the protein, reducing its chemical activity. Also, new labels and labeling techniques often must be developed to complement newly discovered proteins of interest.[9] In addition, as the size of the molecule relative to its label decreases, steric hindrance may become a problem in binding experiments with

those molecules.[8] As the desired detection limits move into pM concentrations and beyond, some labeled detection techniques become increasingly difficult, such as fluorescence techniques where it can be very difficult to distinguish very few fluoresced photons from the background.

This has encouraged the development of a wide variety of label-free detection systems that are equally or more sensitive than labeled detection techniques. Some of the most common include surface plasmon resonance (SPR), quartz crystal oscillators, calorimetry, nanowire and nanotube-based transistors, and micro- or nanoelectromechanical systems (MEMS or NEMS).[8-10] SPR is one of the more common techniques in label-free detection. It is a probe of the local index of refraction just outside a thin metallic film, typically functionalized gold, that is exposed to the sample solution. Changes in the excited plasmons in the metal are induced by analyte binding events that modify the local index of refraction. Quartz crystal oscillators are commonly used devices that can detect any adsorbed mass and have been used in both thin film deposition as well as biological detection. Upon applying an AC voltage to the crystal, mechanical resonance will occur; the resonant frequency is inversely proportional to the square root of the oscillator mass. Therefore, adsorbed mass effectively increases the sensor mass and decreases the resonant frequency accordingly. Field-effect transistor-based devices have also been made from nanowires or carbon nanotubes that show changes in conductance upon binding of charged molecules.[9] Quartz crystal microbalances (QCMs) have demonstrated sensitivities on the order of 1 ng/cm^2 in fluid[11] or 10 pg/cm^2 in vacuum[12] while the best SPR systems have sensitivities of ~100 pg/cm^2.[9] It should be noted, however, that these sensor systems may also be used for “labeled” detection that amplifies the signal or improves sensitivity in some way.

1.4 The Potential of MEMS and NEMS Sensors

MEMS and NEMS devices[13,14] create opportunities for novel, labeled or label-free detectors with high sensitivity and very high levels of multiplexing. Devices with small physical dimensions have exhibited excellent sensitivity and therefore potential for appropriately redundant and multiplexed sensor arrays. For example, IBM has developed the "Millipede," a fully-integrated microcantilever array of 1024 devices that occupies a small area.[15] One can imagine such an array with the ability to detect numerous analytes from a single sample. This level of bulk fabrication and sensor multiplexing is not easily accessible in other techniques like SPR or QCM. In addition, recent research has demonstrated detection of biological masses from picograms to attograms (10^{-12} to 10^{-18} g) and sensitivity to concentrations on the order of nM or less.

The planar processing techniques used to create MEMS and NEMS sensors allow flexibility in the sensor system architecture in order to optimize the mass transport and fluid flow for a given sensor requirement. For example, the size and number of devices can be chosen based on the sample volume and design of a lab-on-a-chip system. Arrays of small devices can be particularly advantageous in optimizing the sensitivity of the individual elements, increasing the sampling area with large numbers of devices and arranging the spacing and functionalization for the most efficient flow or diffusion-based delivery of analyte to the surface. Theoretical modeling of nanoscale sensors operating in fluid have demonstrated that using arrays of devices in a constrained volume can actually improve the overall sensor response in the limit of dilute analytes.[16] These improvements are dependent on the fill fraction of the sensors on the surface; the spacing can be optimized to the diffusion length of the

analyte, such that the fluid volume sampled by each sensor does not overlap with that of its neighbors.

MEMS and NEMS sensors are versatile platforms that can be used to detect any kind of analyte as long as a specific binding chemistry exists. Similar to current techniques, if there are antibodies, complementary single-stranded DNA molecules (ssDNA), aptamers, or particular polymer(s) which specifically capture analytes, MEMS and NEMS sensors can be used to detect their presence. Considering this, their small size, and their high sensitivities, MEMS and NEMS sensors represent a promising technological field that could be an important part of the future of sensing.

REFERENCES

1. B. Ilic, H. G. Craighead, S. Krylov, W. Senaratne, C. Ober, and P. Neuzil, "Attogram detection using nanoelectromechanical oscillators," *J. Appl. Phys*. **95**(7) (2004) 3694-3703.

2. K. L. Ekinci, X. M. H. Huang, and M. L. Roukes, "Ultrasensitive nanoelectromechanical mass detection," *Appl. Phys. Lett*. **84**(22) (2004) 4469-4471.

3. B. Ilic, Y. Yang, K. Aubin, R. Reichenbach, S. Krylov, and H. G. Craighead, "Enumeration of DNA Molecules Bound to a Nanomechanical Oscillator," *Nano Lett*. **5**(5) (2005) 925-929.

4. Y. T. Yang, C. Callegari, X. L. Feng, K. L. Ekinci, and M. L. Roukes, "Zeptogram-Scale Nanomechanical Mass Sensing," *Nano Lett*. **6**(4) (2006) 583-586.

5. T. M. Squires, R. J. Messinger, and S. R. Manalis, "Making it stick: convection, reaction and diffusion in surface-based biosensors," *Nat. Biotechnol.* **26**(4) (2008) 417-426.

6. M. M. Elrick, J. L. Walgren, M. D. Mitchell, and D. C. Thompson, "Proteomics: Recent Applications and New Technologies," *Bas. & Clin. Pharmacol. & Toxicol*. **98** (2006) 432-441.

7. C. Hempen and U. Karst, "Labeling strategies for bioassays," *Anal. Bioanal. Chem*. **384** (2006) 572-583.

8. N. Ramachandran, D. N. Larson, P. R. H. Stark, E. Hainsworth, and J LaBaer, "Emerging tools for real-time label-free detection of interactions on functional protein microarrays," *FEBS Journal* **272** (2005) 5412-5425.

9. M. A. Cooper, "Label-free screening of bio-molecular interactions," *Anal. Bioanal. Chem.* **377** (2003) 834-842.

10. J. Homola, S. S. Yee, G. Gauglitz, “Surface plasmon sensors: review,” *Sens. Actuators, B* **54** (1999) 3-15.

11. Q-Sense AB. Västra Frölunda, Sweden [Online]. Available: http://www.q-sense.com

12. A. W. Warner, in *Ultra Micro Weight Determination in Controlled Environments*, ed. S. P. Wolsky and E. J. Zdanuk, Interscience, New York, 1969, ch. 5, pp. 137-161.

13. H. G. Craighead, “Nanoelectromechanical Systems,” *Science* **290** (2000) 1532-1535.

14. K. L. Ekinci and M. L. Roukes, “Nanoelectromechanical systems,” *Rev. Sci. Inst*. **76** (2005) 061101.

15. W. P. King, T. W. Kenny, K. E. Goodson, G. L. W. Cross, M. Despont, U. T. Dürig, H. Rothuizen, G. Binnig, and P. Vettiger, “Design of Atomic Force Microscope Cantilevers for Combined Thermomechanical Writing and Thermal Reading in Array Operation,” *J. Microelectromech. Syst.* **11**(6) (2002) 765-774.

16. J. Bishop, A. Chagovetz, and S. Blair, “Effects of fill fraction on the capture efficiency of nanoscale molecular transducers,” *Nanotechnology* **17** (2006) 2442-2448.

CHAPTER 2

MEMS AND NEMS SENSOR TECHNOLOGY*

MEMS and NEMS technology can trace its roots back to the development of atomic force microscopy (AFM), which demonstrated the utility of a cantilevered sharp tip in mechanically probing a surface.[2] This tip can either be scanned in contact with the surface, using cantilever deflection to map sample topography via the tip-sample interaction force, or resonantly excited slightly above the sample, monitoring changes in the resonant properties of the cantilever that arise as a result of the surface. Since then, the versatility of this technique has been demonstrated by the development of numerous new sensing modes, e.g. capacitance or magnetic-based AFM, as well as applications of cantilevers and similar MEMS and NEMS devices as sensors.

Recently, micro- and nanometer scale cantilevers have been studied as sensors using physical principles that are similar to those found in atomic force microscopy. These cantilevers are generally operated in either the static deflection mode, where binding on one side of a cantilever causes an unbalanced surface stress that results in a measurable deflection up or down, or the dynamic, resonant mode, where binding on the cantilever increases mass and thus decreases the resonant frequency, much like quartz crystal microbalances. Cantilevered devices have been demonstrated as highly versatile sensors using mechanical, optical, electrostatic, and electromagnetic methods for actuating or detecting cantilever motion.

With appropriate chemical functionalization, MEMS and NEMS can become sensitive detectors of different chemical or biological entities. Their size and design flexibility suggest the possibility of incorporation in microfluidics and miniaturized

* This chapter is a modified and more focused form of a detailed review of MEMS and NEMS sensors written by P.S. Waggoner and H.G. Craighead in Reference [1].

lab-on-a-chip formats. While the static deflection mode sensors are a more mature technology, resonant mode devices have also shown high sensitivities and may be more flexible in their design and use, as they can be smaller than static mode devices and also possess a spectrum of resonances in which some modes can be more sensitive than others. The state of the art of these two categories of MEMS and NEMS sensors are further discussed below, along with examples of demonstrated sensor applications, and a comparison between the two, setting the stage for the following discussions and experiments in the present work.

2.1 Deflection-based Sensors

For sensor systems where analyte binding induces surface stress, flexible cantilevers functionalized on one side are used to transduce that stress into a measurable deflection. The operating principles and physics behind deflection-based MEMS and NEMS sensors will be briefly discussed in the following. In addition, some of the most recent developments in this field will be highlighted. More comprehensive reviews that focus on deflection-based cantilever sensors have been presented.[3-5]

2.1.1 Operating Principles

Deflection-based MEMS and NEMS sensors of all types operate on the physical principles described by G. G. Stoney while studying tension and delamination of thin metal films in 1909.[6] Observing that when metals are deposited under tension

they can sometimes bend the substrate, he developed what is now known as Stoney's formula,

$$R = \frac{Et^2}{6\sigma(1-\upsilon)} \tag{2-1}$$

where R is the radius of curvature, E is the Young's modulus, t is the thickness of the substrate, σ is the surface stress, and n is the Poisson's ratio of the substrate. The radius of curvature is proportional to the out-of-plane deflection divided by the square of the cantilever length. As a result, cantilevers used for static deflection measurements are typically long, on the order 100s of micrometers, in order to maximize the deflection out of plane and, therefore, the signal from small radii of curvature. By far, the most common way to measure this deflection is to use optical reflection; a laser is focused on the cantilever and reflected onto a position sensitive detector that can detect small displacements of the beam.

Silicon or silicon nitride cantilevers are generally used because of the widespread use of silicon in microelectronics and also the compatibility and availability of fabrication methods for cantilevers and integrated circuitry. However, upon inspection of Equation (2-1), it is evident that the cantilever radius of curvature can be further decreased if a less stiff material were used. To this end, silicon dioxide[7] and SU-8[8-10] cantilevers have been used to attain larger cantilever deflections. In addition, SU-8 is minimally responsive to pH, unlike silicon devices.[10]

Adsorption-induced bending of cantilevers was seen initially in the formation of alkanethiol self-assembled monolayers (SAM) on a gold coated cantilever.[11] Soon after, this concept was applied to detect DNA hybridization using ssDNA molecules as immobilized receptors on a microcantilever.[12] This technique was demonstrated to be

sensitive to single base pair mismatches, since cantilevers with such mismatched receptor molecules did not support hybridization. Prostate specific antigen was detected at low concentrations using immunoassay techniques on microcantilevers.[13]

The physical mechanisms underlying adsorption or binding-induced surface stresses have been much debated. There has been evidence and suggestions of electrostatic repulsion, steric repulsion, configurational entropy, ssDNA surface (or grafting) density, hydration forces, and osmotic pressure.[11,12,14-16] These arguments were unified in a comprehensive study by Stachowiak *et al*. in which the ssDNA grafting density was measured as a function of immobilizing salt concentration, and two concentration-dependent regimes were observed.[17] The authors conclude that osmotic forces dominate at low salt concentrations, until the grafting density allowed by the salt becomes large enough that hydration forces begin to dominate, after which the grafting density saturates and further increasing salt concentrations has no effect.

Recent work on the subject has suggested that binding events need to occur in a connected manner before surface binding can result cantilever deflection, using a model based on percolation theory.[18] This work agrees with the intermolecular effects discussed above that fall off quickly with distance. In addition, this describes a fundamental limit of detection for static mode cantilever sensors, where such low concentrations of analyte would only bind sparsely on the device surface and fail to produce a measurable cantilever deflection.

2.1.2 Sensor Examples

A variety of gaseous and liquid-based chemical sensors have been developed to detect changes in environmental conditions or particular chemical vapors. Ji ***et al.***

observed the bending responses of several cantilever material and coating combinations in solution as a function of pH.[19] Sensitivity to pH values ranging from 2 to 12 was demonstrated, while not all material combinations were sensitive across that entire pH range. Cantilevers functionalized with a variety of polymer coatings have been studied as an artificial nose, demonstrating the ability to detect, in the gas phase, a number of alcohols, solvents, and natural flavors.[20] Alkane-thiol self-assembled monolayers were recently used to detect toluene and water vapor with gold-coated silicon nitride cantilevers.[21] Microscale sensors using a polycarbonate film have been used to sense a wide range of carbon dioxide concentrations.[22] Trinitrotoluene vapors have been detected at concentrations as low as 120 ppt using silicon oxide cantilevers coated with a thiol-based self assembled monolayer.[23] In addition, mercury vapor adsorption to a gold-coated cantilever can produce significant surface stress and has been used in deflection-based sensors.[24]

Recently, static mode cantilever biosensors have demonstrated detection of several different analytes with both traditional and novel sensor designs. *Salmonella* bacteria strains have been detected using cantilevers functionalized with antibodies to the bacteria; a deflection was detected with as few as 25 bacteria attached to the device.[25] Cantilevers coated with a specific layer of short peptide chains were used to detect a concentration of roughly 10^8 *Bacillus subtilis* spores per mL due to static deflection of the device.[26] Creatin kinase and myoglobin were detected simultaneously within a liquid cell, at moderate concentrations of about 20 μg/mL.[27] Sensors for DNA transcription factors have also been constructed, using microcantilevers functionalized with double-stranded DNA.[28] Single-chain Fv antibody fragments were used in a cantilever array to detect engineered peptide antigens.[29] A unique method of surface chemistry using calixarene-derived Calixcrown linkers was used to sense the cancer biomarkers C-reactive protein and

PSA at concentrations of 10 to 100 ng/mL.[30] Taq DNA polymerase has been sensed using aptamer-functionalized, interdigitated cantilevers that are transduced by diffractive methods.[31] Single-stranded DNA molecules with single base pair mismatches have been detected at concentrations as low as 10 nM using piezoresistive cantilevers.[32] Concentrations of biotin as low as 100 pg/mL have been detected using a silicon cantilever that has a built-in MOSFET at the base of the sensor.[33] Since the conductivity of silicon is strain dependent, deflections of the cantilever are read out as changes in the source to drain current of the transistor.

Conformational change has recently been presented as a new mechanism causing cantilever deflection. The stimuli responsible for inducing the conformational change are therefore available to be sensed by cantilevers functionalized with these biomolecules. Specialized DNA molecules have been shown to reversibly change from a folded, 4-stranded conformation into an elongated, duplex formation depending on the pH of the solution.[34] Other examples include conformational changes in human estrogen receptors with or without estradiol[35] and the membrane protein bacteriorhodopsin.[36]

2.2 Resonant Sensors

Resonant micro- and nanoscale sensors consist of cantilevers operated in the dynamic mode as well as any other devices that can be excited at a stable resonant frequency. Recent work has demonstrated that these devices are now capable of measuring masses on the order of attograms and less.[37-40] Resonating MEMS sensors have been used for some time, as mechanical sensors of force, flow, pressure, and acceleration[41] or as chemical sensors, while their application to biology is a more

recent development. Despite the more common use of deflection-based cantilevers as biosensors due to their ability to function in fluid environments, resonant devices have shown superior ability to measure extremely small masses, and recent work has demonstrated new possibilities for improving device sensitivities and operating resonant sensors in fluid with enhanced mass resolution.

2.2.1 Operating Principles

Resonant mechanical devices are commonly modelled as harmonic oscillators with a resonant frequency, f_0, given by

$$f = \frac{1}{2\pi}\sqrt{\frac{k}{m}} \tag{2-2}$$

where k is the spring constant and m is the mass of the oscillator. If some added material changes the mass or spring constant by comparatively small amounts, Δm or Δk, respectively, the change in frequency, $\Delta f = f - f_0$, due to that material can be approximated to the first order by

$$\frac{\Delta f}{f_0} = \frac{1}{2}\left(\frac{\Delta k}{k} - \frac{\Delta m}{m}\right) \tag{2-3}$$

An increase in the spring constant, according to Equation (2-3), would lead to an increase in resonant frequency while additional mass would decrease the frequency. The spring constant is proportional to the flexural rigidity of the resonator, D, given by the product of stiffness or Young's modulus, E, and the second moment of the cross

section, *I*, a geometric term describing the cross-sectional effect on the flexibility of the device. For instance, *I* for cantilevers is proportional to wt^3, where *w* is the width of the cantilever. So, if a fairly stiff or relatively thick film were added to the cantilever, it would become more rigid and act more like a composite beam, causing the resonant frequency to increase. It is important to note that the thickness plays a role in both the added mass and flexural rigidity of the resonator and can dictate which dominates the frequency shift, especially when the thickness of the added layer approaches that of the device.[42,43] For a resonant sensor functionalized to specifically bind a particular analyte, knowing the resonant frequency before and after the binding step allows one to associate the change in frequency with an amount of bound analyte, and more importantly with a more meaningful quantity like concentration.

Related effects were observed when Thundat *et al.* studied the adsorption of mercury to gold-coated, resonant cantilevers.[24] On some sensors, gold was only deposited near the free end of the cantilever, in which case a decrease in resonant frequency was observed with increased exposure to mercury, signifying adsorption and detection of added mass. However, in cases where a complete film of gold was used, the frequency was found to increase with exposure, suggesting that mercury adsorption increases the flexural rigidity of the beam. More recently, these effects were observed in bacteria adsorption to a resonant cantilever sensor.[44] Using inkjet-deposited droplets of bacteria placed along cantilevers, it was demonstrated that near the clamped end the frequency increases due to stiffness effects while near the cantilever tip the frequency decreases due to the mass effects. A recent study using cantilevers measuring only 30 nm in thickness demonstrated similar effects.[42] As protein multilayers were deposited on the devices, resonant frequency initially decreased but eventually became a large positive shift as the thickness of the added layers surpassed that of the device. Despite a decrease in the composite Young's

modulus of the beam, a two- or threefold increase in device thickness after functionalization can increase the flexural rigidity by a factor of 10 or more, as it is proportional to t^3. These works suggest that the mechanical properties of the analyte can be important at high coverages.

For resonant sensors, the quality factor is another important quantity that determines absolute mass sensitivity and frequency shift resolution. The quality factor, Q, is defined as $Q = f_0 / \Delta f_{fwhm}$, where f_0 is the resonant frequency and Δf_{fwhm} is the full-width at half maximum of the resonance peak. Q is also a measure of the losses of the system, in that it is proportional to the energy stored in the resonance over the energy lost per cycle. The decreasing width at half-maximum facilitates interpretation of frequency shifts since sharper peaks allow higher resolution of peak frequency shifts and, therefore, increased sensitivity to added mass. Assuming that a particular fraction of the resonant peak full width at half-maximum can be resolved, Δf in Equation (2-3) is proportional to f_0 / Q. Solving for the minimum detectable mass (while neglecting stiffness effects) using the above approximation yields the following:

$$\Delta m_{\min} \propto \frac{m}{Q} \tag{2-4}$$

Decreasing the initial sensor mass, m, and increasing quality factor both reduce the minimum detectable mass of the device. Naturally, the progression to more sensitive resonant sensors has encouraged the development and use of resonant nanoelectromechanical systems. This is in direct contrast to deflection-based microcantilever devices, whose radius of curvature signal requires increasing device length in order to maximize sensitivity. Equation (2-4) also suggests operation of

these devices in vacuum as opposed to in air or liquid, where viscous damping losses significantly reduce *Q*.

Quartz crystal microbalances are large scale resonant sensors, similarly measuring mass by monitoring the resonant frequency of the crystal. Despite having relatively large masses, the sensitivity of QCMs is maintained due to high quality factors. While in vacuum MEMS and NEMS sensors surpass the sensitivity of QCMs, in air or liquid, the QCM typically performs much better. Recently, however, nanomechanical beams are becoming competitive with QCMs in terms of mass sensitivity per unit area when used in air.[45] Beams measuring 2 μm × 165 nm × 125 nm were found to resonate at 140 MHz with a quality factor of ~400. Using a conservative estimate that one can resolve frequency shifts that are 10% of the peak width at half maximum, Equation (2-4) reveals that these devices have a mass per unit area sensitivity of 2.5 ng/cm^2.

2.2.2 The Surface Stress Debate

While surface stress constitutes the basis of deflection-based sensors, it is not always an issue for resonance-based cantilever sensors and can often go unnoticed. Although several different models have been proposed to describe how surface stress changes the resonant properties of cantilevers, others have questioned whether the two are even connected. Much debate over this topic persists in the literature, and at this time no consensus has been reached. It is noted, however, that both stress and surface stress are plausible sensing mechanisms for doubly-clamped beam resonators that are constrained between two clamping points, however, such sensor systems are difficult to find in the literature. Detailed discussion of the effect of stress on the resonant

frequency and quality factor of doubly-clamped beams can be found in Reference [46].

In many of these models, surface stresses are allowed to affect the stiffness of the resonators and are sometimes considered as a perturbation of the spring constant. So, if the percent change in spring constant exceeds that of the mass, the spring constant then dictates the frequency shift. However, in this model, the spring constant can either increase or decrease the resonant frequency depending on whether the stress is compressive or tensile, which may become problematic if this change is on the same order of magnitude as the change in mass.

Surface stress-induced frequency shifts were first suggested in 1975 to explain unexpected resonant frequency behaviors of GaAs resonators.[47] The surface stress, assumed to present on both sides of the cantilevers, was treated as an axial force per unit length. A response to this publication was made that refuted this model and pointed out that in classical beam theory strain-independent surface stresses have no effect on the resonant frequency of a cantilever.[48] Alternative mechanisms were suggested based on surface elasticity (strain-dependent surface stress) and changes in elastic constants, however both were estimated to be negligible in this situation.

Despite the comments made by Gurtin *et al.*,[48] the axial force model is claimed to describe resonant frequency shifts.[49-52] A simplified, one-dimensional version of this model has also been developed that treats cantilevers as strings with no flexural rigidity.[53] Changes in surface stress are modeled through changes in the spring constant of the cantilever. This model has also been cited in resonant biosensor papers.[54,55]

Surface elasticity arguments have been broached again and further developed by Lu *et al.*, who question this model, suggesting that it considerably overestimates external forces and that a taut string is not the best model for a cantilever.[56] They

continue to model the cantilever by adding surface stress effects directly into the equations of motion, rather than as a perturbation in spring constant, and find that stress-related frequency shifts are inversely proportional to the Young's modulus and thickness of the beam. The model also shows that binding on both sides of the cantilever, while not producing a static deflection since the stresses should roughly balance, can still change the resonant frequency. They suggest that these effects will only be observed in cases where very thin cantilevers with high quality factors are used and the material system is right for creating large surface stresses. In one example of such a system, exposure of thin, single crystal silicon cantilevers to acetylene or oxygen environments have shown large increases in resonant frequency upon adsorption of the gases.[57] However, for the small surface stresses typically observed with biosensors, they suggest that frequency shifts due to strain-dependent surface stress will be negligible.

Lachut and Sader have questioned these one-dimensional models based on axial forces[47,53] and stated that they violate Newton's third law.[58] They continue by noting that surface stress on both sides of a free, isolated plate will flatten it slightly, depending on its dimensions, Young's modulus, and Poisson's ratio. However, if the plate is fixed at one end as a cantilever, the fixed end is not allowed to deform, resulting in non-uniform deformation of the cantilever along its length. Finite element analysis is used to show that this non-uniform, in-plane deformation of the cantilever due to the clamping restraints is the only way in which surface stress may affect the resonant frequency. The authors point out that this effect is quite small and cannot account for the frequency shifts discussed in the literature. Recently published work from these authors have demonstrated that geometry can play quite a significant role in how surface stresses affect resonant frequency.[59] However, they still hold that most

resonant cantilever sensors in the literature that are claimed to transduce surface stress are likely due to some other mechanism.

Interestingly, a deflection-based cantilever sensor for bacterial spores was also resonantly excited in order to measure a frequency shift upon spore attachment.[26] While showing a tip deflection due to surface stress, a negative frequency shift was observed that corresponded to an approximate spore mass which was comparable to previously reported values. These results suggest that surface stress either has no effect on the resonance or that it is insignificant compared to mass-related effects.

2.2.3 Actuation and Detection Mechanisms

While static deflection-based cantilever sensors are mostly read out using laser deflection, there is a wider variety of techniques used to actuate and detect resonant MEMS and NEMS devices. They can be interchanged and paired based on the specific applications or availability of apparatus. These methods of actuation and detection are discussed below, highlighting advantages and disadvantages as well.

Thermal excitation is a simple way in which resonance can be excited. Heat is imparted to the device which then excites resonance by thermal expansion stresses or by using a bilayer of materials with different thermal expansion coefficients. In some cases, even thermal fluctuations in ambient conditions can excite device oscillation and support sensor operation.[60] Another method, compatible with semiconductor processing techniques, is to fabricate resistors near the resonators that will excite the devices via Joule heating. Modulation of the heating source at the resonant frequency of the devices excites oscillation. This has been used to actuate dome-shaped MEMS resonators[61] as well as conventional cantilever sensors.[62]

Resonant sensors can also be driven electrostatically or magnetically, and resonance can be monitored using capacitance, encouraging integration with CMOS technology. Out-of-plane resonance has been excited using electrostatic fields between gold films on and near the cantilever.[63] In addition to the fundamental mode, the torsional[64] and in-plane[65] modes have been actuated in this way. Recently, an analogous technique has been described for detecting or exciting any dielectric resonator using its polarizability and a non-uniform electric field.[66]

Magnetically excited devices generally use a microfabricated wire loop on the cantilever on which an alternating current is driven in a static magnetic field to generate out-of-plane excitation using the Lorentz force.[67] Doubling back the wire loop near the center of the cantilever creates an opposite Lorentz force from the end and allows excitation of the second flexural mode using the same external magnetic field.[68] Cantilevers made from magnetostrictive materials can also be excited using a varying magnetic field.[69]

Oftentimes, the electromagnetic nature of these excitation mechanisms and their fabrication fit well with piezoresistive detection via built-in resistors[62,70] or CMOS circuits.[67] This method is implemented using a Wheatstone bridge, consisting of four resistors, three constant and one variable.[71] The piezoresistive element operates as the variable resistor which changes as the cantilever is strained during deflection or resonance. This technique is sometimes favored compared to others since the resonance probe is built-in, is easily coupled with resistive heating or other on-device excitation methods, and can be encapsulated to protect from a liquid environment.

Another method for excitation of resonance takes advantage of piezoelectric materials. Simply attaching the resonator device chip externally to a driven piezoelectric device can induce resonance. Recently, piezoelectric layers have also

been incorporated into multilayer cantilever sensors which can be used to electrically excite motion, detect resonances, or both.[54,55,72,73]

In contrast to the above methods that require extra layers of fabrication and addressable electronics, optical excitation and readout offers an external method that can greatly simplify fabrication, minimizing the number of processing steps required. It is also particularly useful for reading large arrays of sensors that would present a formidable problem for other techniques, especially if each device requires electrical connections. A focused laser beam, modulated at device resonance, can act as a localized heat source which thermally excites oscillation.[74,75] Direct illumination of the device is not required, as resonance has been observed in silicon nitride cantilevers when the laser was focused over 160 μm from the clamped end.[75] Another advantage to optical excitation is that it can be applied to a wide variety of device geometries, opening up resonant sensors to creativity and innovation unhindered by electrical integration requirements. For example, parametric amplification of isolated, disk-shaped resonators has been demonstrated using a modulated laser beam, greatly amplifying the signal amplitude and improving force sensitivity.[76]

Optical techniques can also be used to measure device resonance. For larger cantilevers, optical deflection is an option, but as devices become smaller the reflected signal diminishes. However, optimized placement of the detection beam can assist in measuring not only the fundamental mode but also higher modes of cantilever resonance.[77] A more flexible method uses the thin film stack of device layer, sensing medium, and substrate as a Fabry-Pérot interferometer.[78] Using a laser to illuminate a region of the device oscillating out-of-plane, the reflected light will be modulated due to the changing gap height between the sensor and substrate. HeNe laser illumination has been used to detect oscillation in nanomechanical systems with feature sizes significantly less than the wavelength of light (633 nm).[79] Interferometric detection

has also been used to detect in-plane modes, where the varying overlap of device and laser provide the modulation of the reflected beam, rather than a changing vacuum gap beneath the device.[80]

Some recent studies have demonstrated unique methods to detect sensor resonance. One method places an electrode just within the range of motion of a cantilever resonating in-plane so that the cantilever will physically hit the electrode once every cycle, sending an electrical signal each time.[81] A new type of optical detection has been demonstrated using linear silicon nitride optical waveguides that have been patterned into cantilevers.[82,83] When at rest, light passes through the cantilever and across the relatively small gap between its tip and the remaining waveguide. Device resonance modulates the light that is able to pass through the rest of the waveguide, which can be used to monitor the resonant frequency.

2.2.4 Sensor Examples

Micromechanical devices have been applied as atmospheric gas sensors for several common gases. The detection of water vapor was demonstrated using phosphoric acid-coated cantilevers.[84] Wang *et al.* reported that oxidation of nanomechanical cantilevers resulted in significant increase in resonant frequency due to the induced surface stresses on the single crystal silicon devices.[57] Nanomechanical beams coated with palladium have been applied as hydrogen gas sensors for pressures above 10^{-5} Torr, due to the significant uptake of hydrogen in this metal.[85] A micromechanical, membrane-type resonant sensor has been developed for specific detection of carbon dioxide, using a coating of single walled carbon nanotubes as the active layer.[86] One particularly clever sensor used deposited films of PtO_2 for

detection of hydrogen in air.[87] Hydrogen will chemically react with the platinum oxide, reducing it into platinum, water, and heat, which decreases the amount of mass on the cantilever, producing an increase in resonant frequency.

In addition to atmospheric gas sensing, chemical vapors have also been detected with reasonable success using resonant MEMS and NEMS devices. Mercury vapor, which adsorbs well to gold, has been detected using cantilevers decorated with gold islands.[24] Octane and toluene vapors at concentrations on the order of hundreds of parts per million have been detected using piezoresistive cantilevers functionalized with a layer of polyetherurethane.[62] More recent work using polyetherurethane and polydimethylsiloxane layers on cantilevers, driven both electrostatically and magnetically, has demonstrated detection of 1-butanol, toluene, and n-octane as well as relative detection of binary mixtures of butanol and octane.[88] These devices have also demonstrated the ability to detect other volatile organic vapors, including several alkanes and alcohols.

In the last several years, resonant MEMS and NEMS devices have been increasingly studied as ultrasensitive biological detectors. Ilic *et al.* fabricated cantilevers for the detection of *E. coli* bacteria; as few as 16 cells, or about 6 pg total, were detected in air using ambient thermal noise to excite resonances, despite the low quality factor due to viscous damping.[60] Using cantilevers coated with antibodies specific to the bacteria, resonator frequency shifts were found to increase in magnitude linearly with the number of cells, determined from scanning electron micrographs. In further work with *E. coli*, cantilevers with lengths on the order of 10 micrometers, rather than 100s of micrometers in the previous study, were able to measure the frequency shift due to a single cell (665 fg) adsorbed at the end of the cantilever.[89] Gold-coated silicon cantilevers, actuated in air, were shown to detect 5.5 fg of a thiol-based SAM.[74] Recently, cells were inkjet-printed on large cantilever resonators in

order to detect virus binding to proteins expressed on the cells, opening a new door to cell-based work with resonant sensors.[90]

A creative method using gold nanoparticles was developed in order to amplify very low DNA binding signals from resonating cantilevers.[91] A three-part ssDNA complex bound with thiol-gold chemistry was used, consisting of a bound receptor molecule, the analyte, and a gold-bead functionalized molecule. Following hybridization, silver is selectively nucleated on the gold beads, significantly increasing the bound mass, and thus the resonant signal from the sensor. Although this method requires complicated chemistry, DNA concentrations of 0.05 nM could be detected. Another innovative design placed microfluidic channels inside of a cantilever which then adds mass by adsorption of analyte internally.[92] Although this device was subject to significant frequency drifts over several minutes, ~1 Hz frequency shifts due to binding of 1 mg/mL BSA were detectable. Changes in fluid density were also measured using this resonant frequency shift since the microfluidic channel volume was known. Recent work has further developed this concept towards biosensing applications.[93,94]

Pairing resonant detection with SEM, AFM or other imaging techniques allows one to associate frequency shifts, and therefore mass shifts, with the number of large analytes present on the sensors. Surface micromachined devices force a factor of two correction since the cantilever underside can not be observed. Vaccinia viruses were characterized this way using silicon microcantilevers, allowing measurement of average virus mass.[95] The dry mass of *Listeria innocua* bacteria have also been measured with this counting technique, using critical-point drying to dry cantilevers and bacterial cells before resonant detection.[96]

Piezoelectric actuation and detection has been implemented in resonant MEMS biosensors, allowing actuation and detection to take place internally. Unfortunately,

these devices require much more fabrication than other sensors for similar sensitivities, due to encapsulation requirements for the electrically active parts. Yeast cells have been detected using piezoelectric layers bonded to stainless steel cantilevers functionalized to adsorb the negatively-charged cells from water.[72] However, the millimeter scale of these devices reduced sensitivity, which was only demonstrated for 1 mg/mL concentrations of yeast.

Microcantilevers with an encapsulated piezoelectric layer have been used to detect various concentrations of prostate specific antigen, and sensitivity to concentrations as low as 10 pg/mL were reported.[54] When comparing theoretical mass shifts for these relatively large cantilevers to those found experimentally, experimental values were two orders of magnitude larger than expected. Since bending of the cantilever was observed, they attributed the larger shift to surface stress effects.

While single cell detection has been demonstrated with cantilevers operated in air, sensitivities are limited by losses associated with viscous damping. Operation in vacuum removes these losses, leaving only intrinsic loss mechanisms and leading to order of magnitude improvements in quality factor and sensitivity. Indeed, detection of single baculovirus particles, with masses of 1.5 fg, was made possible using polysilicon nanomechanical cantilevers operated in vacuum.[97] Shortly after, a few attograms of thiol-based self-assembled monolayer were detected in vacuum using 4 μm long, 500 nm wide, and 150 nm thick cantilevers.[37] To enhance sensitivity, small gold dots were fabricated at the free end of the nanoscale cantilevers where the mass-related response is greatest, enabling detection of such little mass. In recent years, nanomechanical resonant biosensors have pushed the limits of sensitivity to the point of single molecule detection. Using cantilevers functionalized similarly with a gold dot, single dsDNA molecules (1587 bp) with a mass of 1.65 ag were detected.[39] Observing many cantilevers revealed approximately discrete frequency jumps

corresponding to a handful of DNA molecules. Recent work has now demonstrated atomic mass resolution for gold deposition on carbon nanotube resonators.[98]

2.3 Comparisons and Limitations

Static deflection-based cantilevers are versatile in that they can be operated in air or liquid, allowing real-time analysis, provided that there are no turbulences or significant fluctuations in temperature of the liquid. This is an important advantage they hold over resonant sensors which are subject to viscous damping effects. However, there have been recent advances in resonant sensing that are improving the sensitivity of these devices in fluid. The use of higher resonant modes of sensors operated in air has been demonstrated to improve sensitivity and reduce viscous losses.[99-103] Results showing higher quality factors for higher resonant modes suggest similar improvements for devices used in liquids.[104,105] The higher resonant frequencies associated with higher modes also help to reduce the hydrodynamic loading of the devices, which will further increase sensitivity. Recent work to put fluidic channels inside of cantilevers shows promise for allowing real-time biosensing from solution with the high sensitivity of resonant sensors operated in vacuum.[92-94]

Much would be gained by integrating these sensors into a microfluidic system as a part of an on-chip system with concentrating, filtering, and other components built in. For such lab-on-a-chip applications, deflection-based sensors may be used but would require some additional attention. Because the sensitivity of deflecting cantilevers is proportional to the square of the length they tend to be long. Avoiding stiction creates constraints in microfluidic integration. While resonant sensors are

small enough to be placed at a high density within microfluidic channels, viscous damping must still be addressed.

One inherent limit to static deflection-based devices comes as a result of the need for one-sided functionalization, which almost always involves a gold/cantilever bilayer structure in order to utilize the gold-thiol linking chemistry. Despite the strong affinity of this binding relationship, the gold-device layer structure can increase background noise, since the bilayer structure is sensitive to temperature fluctuations, as well as other environmental conditions to which the surfaces respond differently.

Another limit to this technique of stress detection is that it is limited to the near monolayer regime. Single molecule adsorption can not generate a measurable deflection in a realistic device; for example, the lower limit for detection of DNA hybridization using deflecting cantilevers was found to be $\sim 2\times10^{10}$ hybridized molecules per mm^2.[16] These conclusions are reinforced by recent work from Ndieyira *et al.* that used a percolation theory to define a lower limit on this technique, as it relies on nearest-neighbor interactions in order to produce a measurable cantilever deflection.[18] On the other hand, resonance-based biosensors have exceeded the absolute mass detection capabilities of deflection-based devices, supporting single cell, virus, and double-stranded DNA molecule detection. Analytes on the order of attograms have been weighed with nanomechanical sensors using frequency shift measurements. This detection regime is likely inaccessible to deflecting biosensors, since in this regime surface-bound analytes are likely few and far between. However, these ultrasensitive resonant devices must be operated in vacuum to avoid viscous fluid damping, while the deflection-based sensors are almost always used in liquid. One unique advantage of resonance-based MEMS and NEMS biosensors over deflection based systems is that devices can be of arbitrary shape, allowing more

flexible applications utilizing higher or unique resonant modes that could have improved sensitivity or higher quality factors.

A range of noise processes, ambient fluctuations and chemical processes have a significant effect on sensitivity of both kinds of MEMS sensors. However, it is important to keep in mind that in many cases the mechanical device and instrumental limitations are not the most significant factors affecting the signal-to-noise ratio. Chemical specificity and associated non-specific binding of non-target compounds is often the most significant limit in sensing performance. Dealing with chemical processes compatible with the NEMS or MEMS devices is important. Some noise effects result from fluctuations in the mechanical elements, but the detection systems in many cases may be a significant source of noise. For instance, in optical measurement systems, there is noise in the intensity and phase of the detected signal, in addition to photodetector shot noise.[106] Due to the DC nature of their signals, static deflection-based systems are particularly susceptible to $1/f$ noise, also referred to as flicker noise. In fact, this noise is often the main factor which limits device sensitivity by increasing the value of the minimum detectable deflection.[107,108] Though this noise is not entirely understood, some studies have observed that flicker noise in piezoresistive cantilevers is dependent on geometry, dopant concentration and distribution, as well as thermal annealing treatments.[107,109] While temperature control systems can be used, small thermal fluctuations and drift may have a significant effect on metalized cantilevers, where the gold coating used for single-sided functionalization has a significantly different thermal expansion coefficient relative to the cantilever. External vibrations and thermal variations can also affect resonant devices, however.

In resonant detection systems, the frequency width of the resonant response is the fundamental limit on sensitivity, and this feature, usually discussed in terms of the

mechanical quality factor, Q, can be influenced by many factors.[110,111] In fluids, viscous damping is the primary dissipation mechanism that limits the Q and broadens the resonance. This factor motivates the device designs that optimize the ratio of oscillator mass to Q. In the low pressure regime, viscous damping is eliminated but chemical coatings can also contribute to mechanical losses and degrade the quality factor.

REFERENCES

1. P.S. Waggoner and H.G. Craighead, "Micro- and nanomechanical sensors for environment, chemical, and biological detection," *Lab Chip* **7** (2007) 1238-1255.

2. G. Binnig, C. F. Quate, and C. Gerber, "Atomic Force Microscope" *Phys. Rev. Lett.* **56**(9) (1986) 930-933.

3. C. Ziegler, "Cantilever-based biosensors," *Anal. Bioanal. Chem*. **379** (2004) 946-959.

4. N. V. Lavrik, M. J. Sepaniak, and P. G. Datskos, "Cantilever transducers as a platform for chemical and biological sensors," *Rev. Sci. Inst*. **75**(7) (2004) 2229-2253.

5. L. G. Carrascosa, M. Moreno, M. Alvarez, and L. M. Lechuga, "Nanomechanical biosensors: a new sensing tool," *Trends Anal. Chem*. **25**(3) (2006) 196-206.

6. G. G. Stoney, "The Tension of Metallic Films Deposited by Electrolysis," *Proc. Roy. Soc. London Ser. A* **82**(553) (1909) 172-175.

7. Y. Tang, J. Fang, X. Yan, and H.-F. Ji, "Fabrication and characterization of SiO_2 microcantilever for microsensor application," *Sens. Actuators, B* **97** (2004) 109-113.

8. J. H. T. Ransley, M. Watari, D. Sukumaran, R. A. McKendry, and A. A. Seshia, "SU8 bio-chemical sensor microarrays," *Microelectron. Eng.* **83** (2006) 1621-1625.

9. L. Gammelgaard, P. A. Rasmussen, M. Calleja, P. Vettiger, and A. Boisen, "Microfabricated photoplastic cantilever with integrated photoplastic/carbon based piezoresistive strain sensor," *Appl. Phys. Lett*. **88** (2006) 113508.

10. M. Calleja, J. Tamayo, M. Nordström, and A. Boisen, "Low-noise polymeric nanomechanical biosensors," *Appl. Phys. Lett.* **88** (2006) 113901.

11. R. Berger, E. Delamarche, H. P. Lang, C. Gerber, J. K. Gimzewski, E. Meyer, H.-J. Güntherodt, "Surface Stress in the Self-Assembly of Alkanethiols on Gold," *Science* **276** (1997) 2021-2024.

12. J. Fritz, M. K. Baller, H. P. Lang, H. Rothuizen, P. Vettiger, E. Meyer, H.-J. Güntherodt, Ch. Gerber, and J. K. Gimzewski, "Translating Biomolecular Recognition into Nanomechanics," *Science* **288** (2000) 316-318.

13. G. Wu, R. H. Datar, K. M. Hansen, T. Thundat, R. J. Cote, and A. Majumdar, "Bioassay of prostate-specific antigen (PSA) using microcantilevers," *Nat. Biotechnol*. **19** (2001) 856-860.

14. G. Wu, H. Ji, K. Hansen, T. Thundat, R. Datar, R. Cote, M. F. Hagan, A. K. Chakraborty, and A. Majumdar, "Origin of nanomechanical cantilever motion generated from biomolecular interactions," *Proc. Natl. Acad. Sci. USA* **98**(4) (2001) 1560-1564.

15. M. F. Hagan, A. Majumdar, and A. K. Chakraborty, "Nanomechanical Forces Generated by Surface Grafted DNA," *J. Phys. Chem. B* **106**(39) (2002) 10163-10173.

16. R. McKendry, J. Zhang, Y. Arntz, T. Strunz, M. Hegner, H. P. Lang, M. K. Baller, U. Certa, E. Meyer, H.-J. Güntherodt, and Ch. Gerber, "Multiple label-free biodetection and quantitative DNA-binding assays on a nanomechanical cantilever array," *Proc. Natl. Acad. Sci. USA* **99**(15) (2002) 9783-9788.

17. J. C. Stachowiak, M. Yue, K. Castelino, A. Chakraborty, and A. Majumdar, "Chemomechanics of Surface Stresses Induced by DNA Hybridization," *Langmuir* **22**(1) (2006) 263-268.

18. J. W. Ndieyira, M. Watari, A. D. Barrera, D. Zhou, M. Vogtli, M. Batchelor, M. A. Cooper, T. Strunz, M. A. Horton, C. Abell, T. Rayment, G. Aeppli and R. A. McKendry, "Nanomechanical detection of antibiotic-mucopeptide binding in a model for superbug drug resistance," *Nat. Nanotechnol.* **3** (2008) 691–696.

19. H.-F. Ji, K. M. Hansen, Z. Hu, and T. Thundat, "Detection of pH variation using modified microcantilever sensors," *Sens. Actuators, B* **72** (2001) 233-238.

20. M. K. Baller, H. P. Lang, J. Fritz, Ch. Gerger, J. K. Gimzewski, U. Dreshler, H. Rothuizen, M. Despont, P. Vettiger, F. M. Battiston, J. P. Ramseyer, P. Fornaro, E. Meyer, and H.-J. Güntherodt, "A cantilever array-based artificial nose," *Ultramicroscopy* **82** (2000) 1-9.

21. S.-H. Lim, D. Raorane, S. Satyanarayana, and A. Majumdar, "Nano-chemo-mechanical sensor array platform for high-throughput chemical analysis," *Sens. Actuators, B* **119** (2006) 466-474.

22. R. A. Potyrailo, A. Leach, W. G. Morris, S. K. Gamage, "Chemical Sensors Based on Micromachined Transducers with Integrated Piezoresistive Readout," *Anal. Chem*. **78**(16) (2006) 5633-5638.

23. P. Li, X. Li, G. Zuo, J. Liu, Y. Wang, M. Liu, and D. Jin, "Silicon dioxide microcantilever with piezoresistive element integrated for portable ultraresoluble gaseous detection," *Appl. Phys. Lett.* **89**(7) (2006) 074104.

24. T. Thundat, E. A. Wachter, S. L. Sharp, and R. J. Warmack, "Detection of mercury vapor using resonating microcantilevers," *Appl. Phys. Lett.* **66**(13) (1995) 1695-1697.

25. B. L. Weeks, J. Camarero, A. Noy, A. E. Miller, L. Stanker, and J. J. De Yoreo, "A Microcantilever-Based Pathogen Detector," *Scanning* **25** (2003) 297-299.

26. B. Dhayal, W. A. Henne, D. D. Doomeweerd, R. G. Reifenberger, and P. S. Low, "Detection of *Bacillus subtilis* Spores Using Peptide-Functionalized Cantilever Arrays," *J. Am. Chem. Soc.* **128** (2006) 3716-3721.

27. Y. Arntz, J. D. Seelig, H. P. Lang, J. Zhang, P. Hunziker, J. P. Ramseyer, E. Meyer, M. Hegner, and Ch. Gerber, "Label-free protein assay based on a nanomechanical cantilever array," *Nanotechnology* **14** (2003) 86-90.

28. F. Huber, M. Hegner, Ch. Gerber, H.-J. Güntherodt, and H. P. Lang, "Label free analysis of transcription factors using microcantilever arrays," *Biosens. Bioelectron*. **21** (2006) 1599-1605.

29. N. Backmann, C. Zahnd, F. Huber, A. Bietsch, A. Plückthun, H.-P. Lang, H.-J. Güntherodt, M. Hegner, and Ch. Gerber, "A label-free immunosensor array

using single-chain antibody fragments," *Proc. Natl. Acad. Sci. USA* **102**(41) (2005) 14587-14592.

30. K. W. Wee, H. Y. Kang, J. Park, J. Y. Kang, D. S. Yoon, J. H. Park, and T. S. Kim, "Novel electrical detection of label-free disease marker proteins using piezoresistive self-sensing micro-cantilevers," *Biosens. Bioelectron*. **20** (2005) 1932-1938.

31. C. A. Savran, S. M. Knudsen, A. D. Ellington, and S. R. Manalis, "Micromechanical Detection of Proteins Using Aptamer-Based Receptor Molecules," *Anal. Chem*. **76**(11) (2004) 3194-3198.

32. R. Mukhopadhyay, M. Lorentzen, J. Kjems, and F. Besenbacher, "Nanomechanical Sensing of DNA Sequences Using Piezoresistive Cantilevers," *Langmuir*, **21**(18) (2005) 8400-8408.

33. G. Shekhawat, S.-H. Tark, and V. P. Dravid, "MOSFET-Embedded Microcantilevers for Measuring Deflection in Biomolecular Sensors," *Science* **311** (2006) 1592-1595.

34. W. Shu, D. Liu, M. Watari, C. K. Riener, T. Strunz, M. E. Wellend, S. Balasubramanian, and R. A. McKendry, "DNA Molecular Motor Driven Micromechanical Cantilever Arrays," *J. Am. Chem. Soc*. **127**(48) (2005) 17054-17060.

35. R. Mukhopadhyay, V. V. Sumbayev, M. Lorentzen, J. Kjems, P. A. Andreasen, and F. Besenbacher, "Cantilever Sensor for Nanomechanical Detection of Specific Protein Conformations," *Nano Lett*. **5**(12) (2005) 2385-2388.

36. T. Braun, N. Backmann, M. Vögtli, A. Bietsch, A. Engel, H.-P. Lang, C. Gerber, and M. Hegner, "Conformational Change of Bacteriorhodopsin Quantitatively Monitored by Microcantilever Sensors," *Biophys. J*., **90**(8) (2006) 2970-2977.

37. B. Ilic, H. G. Craighead, S. Krylov, W. Senaratne, C. Ober, and P. Neuzil, "Attogram detection using nanoelectromechanical oscillators," *J. Appl. Phys*. **95**(7) (2004) 3694-3703.

38. K. L. Ekinci, X. M. H. Huang, and M. L. Roukes, "Ultrasensitive nanoelectromechanical mass detection," *Appl. Phys. Lett*. **84**(22) (2004) 4469-4471.

39. B. Ilic, Y. Yang, K. Aubin, R. Reichenbach, S. Krylov, and H. G. Craighead, "Enumeration of DNA Molecules Bound to a Nanomechanical Oscillator," *Nano Lett*. **5**(5) (2005) 925-929.

40. Y. T. Yang, C. Callegari, X. L. Feng, K. L. Ekinci, and M. L. Roukes, "Zeptogram-Scale Nanomechanical Mass Sensing," *Nano Lett*. **6**(4) (2006) 583-586.

41. G. Stemme, "Resonant silicon sensors," *J. Micromech. Microeng*. **1** (1991) 113-125.

42. K. Gupta, P. R. Nair, D. Akin, M. R. Ladisch, S. Broyles, M. A. Alam, and R. Bashir, "Anomalous resonance in a nanomechanical biosensor," *Proc. Natl. Acad. Sci. U.S.A.* **103** (2006) 13362.

43. J. Tamayo, D. Ramos, J. Mertens, and M. Calleja, "Effect of the adsorbate stiffness on the resonance response of microcantilever sensors," *Appl. Phys. Lett.* **89** (2006) 224104.

44. D. Ramos, J. Tamayo, J. Mertens, M. Calleja, and A. Zaballos, "Origin of the response of nanomechanical resonators to bacteria adsorption," *J. Appl. Phys.* **100** (2006) 106105.

45. S. S. Verbridge, L. M. Bellan, J. M. Parpia, and H. G. Craighead, "Optically driven resonance of nanoscale flexural oscillators in liquid," *Nano Lett.* **6**(9) (2006) 2109.

46. S. S. Verbridge, D. F. Shapiro, H. G. Craighead, and J. M. Parpia, "Macroscopic tuning of nanomechanics: Substrate bending for reversible control of frequency and quality factor of nanostring resonators," *Nano Lett.* **7**(6) (2007) 1728.

47. J. Lagowski, H. C. Gatos, and E. S. Sproles Jr., "Surface stress and the normal mode of vibration of thin crystals: GaAs," *Appl. Phys. Lett.* **26** (1975) 493.

48. M. E. Gurtin, X. Markenscoff, and R. N. Thurston, "Effect of surface stress on the natural frequency of thin crystals," *Appl. Phys. Lett.* **29** (1976) 529.

49. P. Lu, F. Shen, S. J. O'Shea, K. H. Lee, and T. Y. Ng, "Analysis of surface effects on mechanical properties of microcantilevers," *Mater. Phys. Mech.* **4** (2001) 51.

50. K. S. Hwang, K. Eom, J. H. Lee, D. W. Chun, B. H. Cha, D. S. Yoon, T. S. Kim, and J. H. Park, "Dominant surface stress driven by biomolecular interactions in the dynamical response of nanomechanical microcantilevers," *Appl. Phys. Lett.* **89** (2005) 173905.

51. J. Dorignac, A. Kalinowski, S. Erramilli, and P. Mohanty, "Dynamical Response of Nanomechanical Oscillators in Immiscible Viscous Fluid for *In Vitro* Biomolecular Recognition," *Phys. Rev. Lett.* **96** (2006) 186105.

52. G.-F. Wang and X.-Q. Feng, "Effects of the surface elasticity and residual surface tension on the natural frequency of microbeams," *Appl. Phys. Lett.* **90** (2007) 231904.

53. G. Y. Chen, T. Thundat, E. A. Wachter, and R. J. Warmack, "Adsorption-induced surface stress and its effects on resonance frequency of microcantilevers," *J. Appl. Phys.* **77** (1995) 3618.

54. J. H. Lee, K. H. Yoon, K. S. Hwang, J. Park, S. Ahn, and T. S. Kim, "Label free novel electricxal detection using micromachined PZT monolithic thin film cantilever for the detection of C-reactive protein," *Biosens. Bioelectron.* **20** (2004) 269.

55. K. S. Hwang, J. H. Lee, J. Park, D. S. Yoon, J. H. Park, and T. S. Kim, "*In-situ* quantitative analysis of a prostate-specific antigen (PSA) using a nanomechanical PZT cantilever," *Lab Chip* **4** (2004) 547.

56. P. Lu, H. P. Lee, C. Lu, and S. J. O'Shea, "Surface stress effects on the resonance properties of cantilever sensors," *Phys. Rev. B* **72** (2005) 085405.

57. D. F. Wang, T. Ono, and M. Esashi, "Thermal treatments and gas adsorption influences on nanomechanics of ultra-thin silicon resonators for ultimate sensing," *Nanotechnology* **15** (2004) 1851-1854.

58. M. J. Lachut and J. E. Sader, "Effect of Surface Stress on the Stiffness of Cantilever Plates," *Phys. Rev. Lett.* **99** (2007) 206102.

59. M. J. Lachut and J. E. Sader, "Effect of surface stress on the stiffness of cantilever plates: Influence of cantilever geometry," *Appl. Phys. Lett.* **95** (2009) 193505.

60. B. Ilic, D. Czaplewski, H. G. Craighead, P. Neuzil, C. Campagnolo, and C. Batt, "Mechanical resonant immunospecific biological detector," *Appl. Phys. Lett*. **77**(3) (2000) 450-452.

61. R. B. Reichenbach, M. K. Zalalutdinov, K. L. Aubin, R. Rand, B. H. Houston, J. M. Parpia and H. G. Craighead, "Third-Order Intermodulation in a Micromechanical Thermal Mixer," *J. Microelectromech. Syst*. **14**(6) (2005) 1244–1252.

62. D. Lange, C. Hagleitner, A. Hierlemann, O. Brand, and H. Baltes, "Complementary Metal Oxide Semiconductor Cantilever Arrays on a Single Chip: Mass-Sensitive Detection of Volatile Organic Compounds," *Anal. Chem.* **74**(13) (2002) 3084-3095.

63. S. J. O'Shea, P. Lu, F. Shen, P. Neuzil, and Q. X. Zhang, "Out-of-plane electrostatic actuation of microcantilevers," *Nanotechnology* **16** (2005) 602-608.

64. S. Evoy, D. W. Carr, L. Sekaric, A. Olkhovets, J. M. Parpia, and H. G. Craighead, "Nanofabrication and electrostatic operation of single-crystal silicon paddle oscillators," *J. Appl. Phys*. **86**(11) (1999) 6072-6077.

65. E. Forsen, G. Abadal, S. Ghatnekar-Nilsson, J. Teva and J. Verd, R. Sandberg, W. Svendsen, F. Perez-Murano, J. Esteve, E. Figueras, F. Campabadal, L. Montelius, N. Barniol, and A. Boisen, "Ultrasensitive mass sensor fully integrated with complementary metal-oxide-semiconductor circuitry," *Appl. Phys. Lett*. **87** (2005) 043507.

66. Q. P. Unterreithmeier, E. M. Weig, and J. P. Kotthaus, "Universal transduction scheme for nanomechanical systems based on dielectric forces," *Nature* **458** (2009) 1001.

67. D. Lange, C. Hagleitner, C. Herzog, O. Brand, and H. Baltes, "Electromagnetic actuation and MOS-transistor sensing for CMOS-integrated micromechanical resonators," *Sens. Actuators, A* **103** (2003) 150-155.

68. D. Jin, X. Li, J. Liu, G. Zuo, Y. Wang, M. Liu, and H. Yu, "High-mode resonant piezoresistive cantilever sensors for tens-femtogram resoluble mass sensing in air," *J. Micromech. Microeng.* **16** (2006) 1017.

69. S. Li, L. Orona, Z. Li, and Z.-Y. Cheng, "Biosensor based on magnetostrictive microcantilever," *Appl. Phys. Lett*. **88** (2006) 073507.

70. J. L. Arlett, J. R. Maloney, B. Gudlewski, M. Muluneh, and M. L. Roukes, "Self-Sensing Micro- and Nanocantilevers with Attonewton-Scale Force Resolution," *Nano Lett*. **6**(5) (2006) 1000-1006.

71. J. Thaysen, A. Boisen, O. Hansen, and S. Bouwstra, "Atomic force microscopy probe with piezoresistive read-out and a highly symmetrical Wheatstone bridge arrangement," *Sens. Actuators, A* **83** (200) 47-53.

72. J. W. Yi, W. Y. Shih, R. Mutharasan, and W.-H. Shih, "*In situ* cell detection using piezoelectric lead zirconate titante-stainless steel cantilevers," *J. Appl. Phys*. **93**(1) (2003) 619-625.

73. G. Y. Kang, G. Y. Han, J. Y Kang, I.-H. Cho, H.-H. Park, S.-H. Paek, T. S. Kim, "Label-free protein assay with site-directly immobilized antibody using self-actuating PZT cantilever," *Sens. Actuators, B* **117** (2006) 332-338.

74. N. V. Lavrik and P. G. Datskos, "Femtogram mass detection using photothermally actuated nanomechanical resonators," *Appl. Phys. Lett*. **82**(16) (2003) 2697-2699.

75. B. Ilic, S. Krylov, K. Aubin, R. Reichenbach, and H. G. Craighead, "Optical excitation of nanoelectromechanical oscillators," *Appl. Phys. Lett.* **86** (2005) 193114.

76. M. Zalalutdinov, A. Olkhovets, A. Zehnder, B. Ilic, D. Czaplewski, H. G. Craighead, and J. M. Parpia, "Optically pumped parametric amplification for micromechanical oscillators," *Appl. Phys. Lett*. **78**(20) (2001) 3142-3144.

77. T. E. Schäffer and H. Fuchs, "Optimized detection of normal vibration modes of atomic force microscope cantilevers with the optical beam deflection method," *J. Appl. Phys*. **97** (2005) 083524.

78. D. Carr and H. G. Craighead, "Fabrication of nanoelectromechanical systems in single crystal silicon using silicon on insulator substrates and electron beam lithography," *J. Vac. Sci. Technol. B* **15**(6) (1997) 2760.

79. S. S. Verbridge, J. M. Parpia, R. B. Reichenbach, L. M. Bellan, and H. G. Craighead, "High quality factor resonance at room temperature with nanostrings under high tensile stress," *J. Appl. Phys*. **99** (2006) 124304.

80. B. Ilic, S. Krylov, M. Kondratovich, and H. G. Craighead, "Selective Vibrational Detachment of Microspheres Using Optically Excited In-Plane Motion of Nanomechanical Beams," *Nano Lett.* **7** (2007) 2171.

81. S. Dohn, O. Hansen, and A. Boisen, "Cantilever based mass sensor with hard contact readout," *Appl. Phys. Lett.* **88** (2006) 264104.

82. L. M. Lechuga, J. Tamayo, M. Álvarez, L. G. Carrascosa, A. Yufera, R. Doldán, E. Peralías, A. Rueda, J. A. Plaza, K. Zinoviev, C. Domínguez, A. Zaballos, M. Moreno, C. Martínez-A., D. Wenn, N. Harris, C. Bringer, V. Bardinal, T. Camps, C. Vergnenègre, C. Fontaine, V. Díaz, and A. Bernad, "A highly sensitive microsystem based on nanomechanical biosensors for genomics applications," *Sens. Actuators, B* **118** (2006) 2-10.

83. G. P. Nordin, S. Kim, J. W. Noh, W. Hu, R. Anderson, Y. Qian, J. Song, and S. Ness, "Progress toward parallel microcantilever array readout enabled by in-plane photonic transduction," *International Workshop on Nanomechanical Cantilever Sensors*, 2008, Mainz, Germany.

84. T. Thundat, G. Y. Chen, R. J. Warmack, D. P. Allison, and E. A. Wachter, "Vapor Detection Using Resonating Microcantilevers," *Anal. Chem.* **67**(3) (1995) 519-521.

85. X. M. H. Huang, M. Manolidis, S. C. Jun, and J. Hone, "Nanomechanical hydrogen sensing," *Appl. Phys. Lett.* **86** (2005) 143104.

86. A. Zribi, A. Knobloch, and R. Rao, "CO_2 detection using carbon nanotube n etworks and micromachined resonant transducers," *Appl. Phys. Lett.* **86** (2005) 203112.

87. T. Thundat and L. Maya, "Monitoring chemical and physical changes on sub-nanogram quantities of platinum dioxide," *Surf. Sci.* **430** (1999) L546-L552.

88. D. Then, A. Vidic, and Ch. Ziegler, "A highly sensitive self-oscillating cantilever array for the quantitative and qualitative analysis of organic vapour mixtures," *Sens. Actuators, B* **117** (2006) 1-9.

89. B. Ilic, D. Czaplewski, M. Zalalutdinov, H. G. Craighead, P. Neuzil, C. Campagnolo, and C. Batt, "Single cell detection with micromechanical oscillators," *J. Vac. Sci. Technol., B* **19**(6) (2001) 2825-2828.

90. T. Braun, M. K. Ghatkesar, N. Backmann, W. Grange, P. Boulanger, L.Letellier, H.-P. Lang, A. Bietsch, C. Gerber, and M. Hegner, "Quantitative time-resolved measurement of membrane protein-ligand interactions using microcantilever array sensors," *Nat. Nanotechnol.* **4** (2008) 179.

91. M. Su, S. Li, and V. P. Dravid, "Microcantilever resonance-based DNA detection with nanoparticle probes," *Appl. Phys. Lett*. **82**(20) (2003) 3562-3564.

92. T. P. Burg and S. R. Manalis, *Appl. Phys. Lett*., 2003, **83**(13), 2698-2700.

93. T. P. Burg, A. R. Mirza, N. Milovic, C. H. Tsau, G. A. Popescu, J. S. Foster, and S. R. Manalis, "Vacuum-Packaged Suspended Microchannel Resonant Mass Sensor for Biomolecular Detection," *J. Microelectromech. Syst.* **15**(6) (2006) 703-708.

94. T. P. Burg, M. Godin, S. M. Knudsen, W. Shen, G. Carlson, J. S. Foster, K. Babcock, and S. R. Manalis, "Weighing of biomolecules, single cells and single nanoparticles in fluid," *Nature* **446** (2007) 1066.

95. L. Johnson, A. K. Gupta, A. Ghafoor, D. Akin, and R. Bashir, "Characterization of vaccinia virus particles using microscale silicon cantilever resonators and atomic force microscopy," *Sens. Actuators, B* **115** (2006) 189-197.

96. A. Gupta, D. Akin, and R. Bashir, "Detection of bacterial cells and antibodies using surface m icromachines thin silicon cantilever resonators," *J. Vac. Sci. Technol., B* **22**(6) (2004) 2785-2791.

97. B. Ilic, Y. Yang, and H. G. Craighead, "Virus detection using nanoelectromechanical devices," *Appl. Phys. Lett*. **85**(13) (2004) 2604-2606.

98. K. Jensen, K. Kim, and A. Zettl, "An atomic-resolution nanomechanical mass sensor," *Nat. Nanotechnol.* **3** (2008) 533-537.

99. C. L. Spiel, R. O. Pohl, and Alan T. Zehnder, "Normal modes of a Si(100) double-paddle oscillator," *Rev. Sci. Inst*. **72**(2) (2001) 1482-1491.

100. L. B. Sharos, A. Raman, S. Crittenden, and R. Reifenberger, "Enhanced mass sensing using torsional and lateral resonances in microcantilevers," *Appl. Phys. Lett*. **84**(23) (2004) 4638-4640.

101. R. Sandberg, K. Mølhave, A. Boisen, and W. Svendsen, "Effect of gold coating on the *Q*-factor of a resonant cnatilever," *J. Micromech. Microeng*. **15** (2005) 2249-2253.

102. S. Dohn, R. Sandberg, W. Svendsen, and A. Boisen, "Enhanced functionality of cantilever based mass sensors using higher modes," *Appl. Phys. Lett*. **86** (2005) 233501.

103. A. R. Kadam, G. P. Nordin, and M. A. George, "Use of thermally induced higher order modes of a microcantilever for mercury vapor detection," *J. Appl. Phys*. **99** (2006) 094905.

104. S. Basak, A. Raman, and S. V. Garimella, "Hydrodynamic loading of microcantilevers vibrating in viscous fluids," *J. Appl. Phys*. **99**(11) (2006) 114906.

105. M. K. Ghatkesar, T. Braun, V. Barwich, J.-P. Ramseyer, C. Gerber, M. Hegner, and H. P. Lang, "Resonating modes of vibrating microcantilevers in liquid," *Appl. Phys. Lett.* **92** (2008) 043106.

106. G. G. Yaralioglu, A. Atalar, S. R. Manalis, and C. F. Quate, "Analysis and design of an interdigital cantilever as a displacement sensor," *J. Appl. Phys.* **83**(12) (1998) 7405-7415.

107. X. Yu, J. Thaysen, O. Hansen, and A. Boisen, "Optimization of sensitivity and noise in piezoresistive cantilevers," *J. Appl. Phys.* **92**(10) (2002) 6296-6301.

108. J. Polesel-Maris, L. Aeschimann, A. Meister, R. Ischer, E. Bernard, T. Akiyama, M. Giazzon, P. Niedermann, U. Staufer, R. Pugin, N. F. de Rooij, P. Vettiger, and H. Heinzelmann, "Piezoresistive cantilever array for life sciences applications," *J. Phys.: Conf. Series* **61** (2007) 955-959.

109. J. A. Harley and T. W. Kenny, "High-sensitivity piezoresistive cantilevers under 1000 Å thick," *Appl. Phys. Lett.* **75**(2) (1999) 289-291.

110. K. Y. Yasamura, T. D. Stowe, E. M. Chow, T. Pfafman, T. W. Kenny, B. C. Stipe, and D. Rugar, "Quality factors in micron- and submicron-thick cantilevers," *J. Micromech. Syst.* **9** (2000) 117.

111. K. L. Ekinci, Y. T. Yang, and M. L. Roukes, "Ultimate limits to inertial mass sensing based upon nanoelectromechanical systems," *J. Appl. Phys*. **95**(5) (2004) 2682-2689.

CHAPTER 3

EXPERIMENTAL PROCEDURES

In this chapter, the common themes of device fabrication and interfacing with fabricated resonators will be discussed in detail. The majority of this material will be applicable in each of the following experiments discussed in later chapters and sections. Additional fabrication or experimental procedures performed in particular experiments will be discussed in full detail alongside them later.

3.1 Device Fabrication

Resonator fabrication begins with bare, single-side polished silicon wafers; a schematic of the fabrication process is shown in Figure 3-1. Neither the crystal orientation nor the doping type or concentration is important for these experiments. In order to create free-standing resonators that are able to move separately from the substrate, a sacrificial layer must be added between the resonator device layer and the silicon substrate. As purchased wafers are first cleaned using the widely accepted RCA cleaning process. The silicon wafers are then thermally oxidized in order to grow a 1.5-2.0 μm thick sacrificial film of silicon dioxide, using a wet oxide, HCl-free growth process at 1100° C for several hours (roughly 6-8).

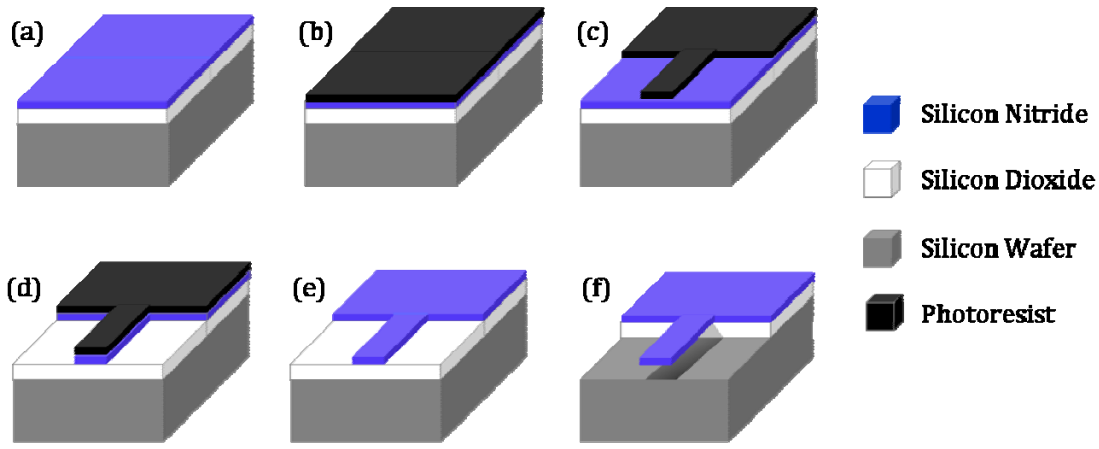

Figure 3-1. Schematic of device processing. (a) First, the device stack is grown, and then (b) a layer of photoresist is spun on and (c) patterned using photolithography. (d) Devices are cut in the silicon nitride using a CF_4 reactive ion etch. (e) After removing the photoresist, (f) the sacrificial silicon dioxide is removed by dipping in hydrofluoric acid, freeing the devices to resonate.

Following oxide growth, the device layer is then deposited. A low-stress silicon nitride device layer is used because it forms into high quality films and has properties that are useful for resonant MEMS sensor applications. This material is silicon-rich when compared to stoichiometric silicon nitride, Si_3N_4, also known as high stress nitride. This is also an important point when considering surface functionalization that will be discussed later. The silicon nitride films are grown using low pressure chemical vapor deposition in which dicholorosilane (SiH_2Cl_2) and ammonia (NH_3) gases are used to form silicon nitride at 800° C on all wafer surfaces. Due to the nature of the LPCVD film growth, several baffle wafers (3-5) are needed before and after device wafers in the tube furnace in order to produce a uniform gas flow over the wafers which will translate into more uniform film thicknesses.

Both the silicon dioxide and the silicon nitride films are studied after growth using a Woollam spectroscopic ellipsometer in order to measure thicknesses and the

optical constants of the films. Typical runs observe the sample using wavelengths of 300-1000 nm at three angles, 65, 70, and 75 degrees. The optical properties of the silicon nitride are very important for the resonators because they are always measured optically and are sometimes excited using another laser source, which will be discussed in the next section. As a reference, the real part of the index of refraction, n_r, and extinction coefficient, κ, of 93 ± 0.91 nm thick, low stress silicon nitride are shown in Figure 3-2 as a function of wavelength. Together, these values form the complex index of refraction, n, given by $n_r + i\kappa$.

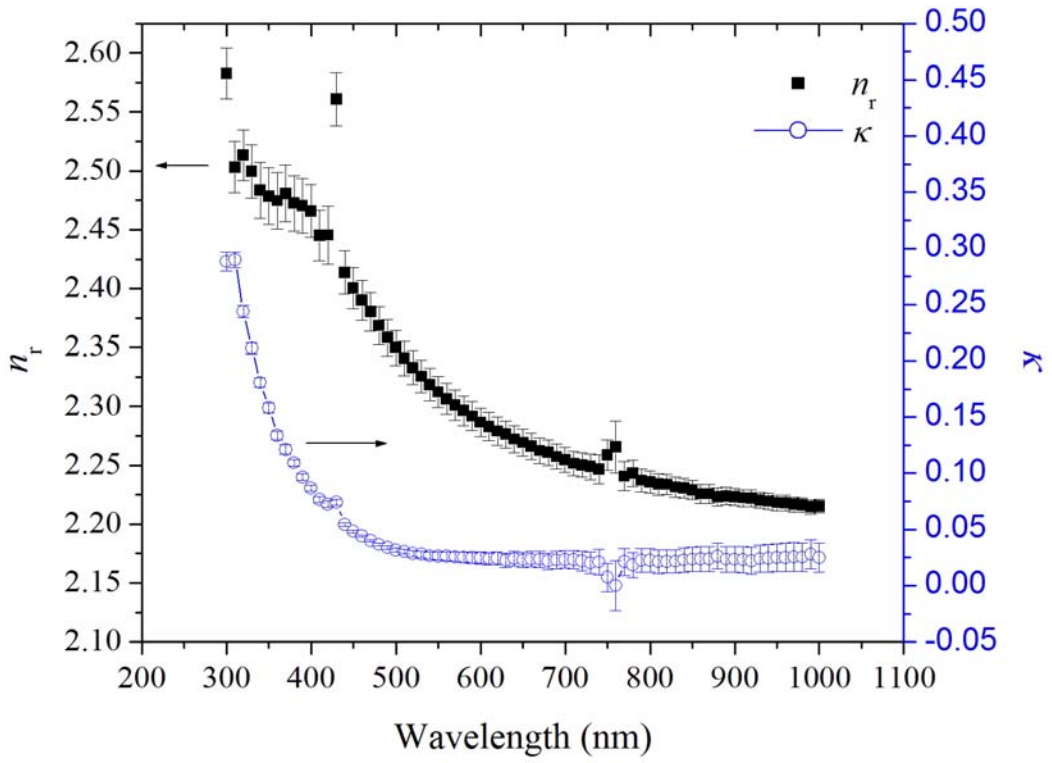

Figure 3-2. Optical properties of low stress, LPCVD silicon nitride measured using ellipsometry.

Next, resonators are patterned into the device layer using photolithography, a technique based the use of photoresists, materials whose solubility changes when exposed to light. After exposure, the resist is then developed, where the parts exposed to light become either soluble (positive resist) or insoluble (negative resist) in the developer chemical, leaving a desired pattern in the remaining photoresist that can act as a stencil to material deposition or removal. First, a CAD design of the desired resonator chip layout must be printed onto a chrome-plated, quartz mask. This is done using a Heidelberg DWL 66 laser pattern generator to expose the desired pattern in the photoresist-coated mask. After developing the photoresist, the exposed chrome is chemically etched away. Once the remaining resist is cleaned off, the mask is then ready to be used to transfer the pattern to device wafers again using photolithography. To do so, a device wafer is spin-coated with a photoresist (typically SPR700-1.2 or SPR955-CM 0.9) at 4000 RPM. After a pre-exposure bake, the wafers are then patterned using a GCA Autostep 200 automated wafer stepper. Then, light (365 nm) is passed through the pattern printed on the mask and then a column of optics that reduces the pattern by a factor of 5, ultimately projecting the design on a photoresist-coated device wafer. Typically, each mask pattern contains roughly two to four thousand resonators in a small area (3 x 3 mm), that are then printed almost 180 times on a single 100 mm wafer.

After developing the resist for 60s in 300 MIF, the device wafer now has photoresist features defining where the resonators will ultimately be. Resonators are then cut out of the device layer in an Oxford PlasmaLab 80+ reactive ion etcher. Initially, a CHF_3/O_2 "Nitride etch" process was used to directionally etch through all silicon nitride not protected by photoresist. Afterwards, the remaining photoresist needs to be stripped from the wafer prior to dicing it into individual chips. However, even after the wafers were left for an extended time in a 70° C bath of *n*-methyl

pyrrolidone (1165 stripper) and tetramethyl ammonium hydroxide (TMAH), a significant amount of polymerized resist is typically left behind on many devices that can be quite difficult to remove. If not removed, the resist will degrade the properties of the resonator and prevent chemical functionalization on the top device surface. From time to time, some of the resist may eventually come off when devices are released in HF, leaving resonator-shaped "ghosts" like those shown in Figure 3-3 which can land on and compromise neighboring devices. However, a CF_4 reactive ion etch process was found to both efficiently etch through the silicon nitride and leave behind very few photoresist residues. The remaining residue was cleaned by exposing the wafer to an oxygen plasma for 3-4 minutes after the hot solvent bath.

Prior to dicing the wafer, a thick layer of Shipley 1818 photoresist is spun on the wafer in order to protect the thin resonators from debris produced while the wafer is diced. This protective resist is soft-baked only briefly so that it can easily be removed later when the chips are needed. After the wafer is cut such that each die sits in the middle of a 6.35 x 6.35 mm square, the resonator chips are ready for long term storage. When needed, chips are first rinsed in acetone and isopropanol prior to being left overnight in 1165 stripper. Then, chips are dipped in 49% HF for roughly 90-100 seconds in order to etch the sacrificial oxide from beneath the devices, freeing them from the substrate and allowing them to vibrate. Scanning electron micrographs of several different released resonators are shown in Figure 3-4. The large square regions are device anchors that are required in order to prevent the resonators from floating away from the surface when the oxide is removed from beneath them.

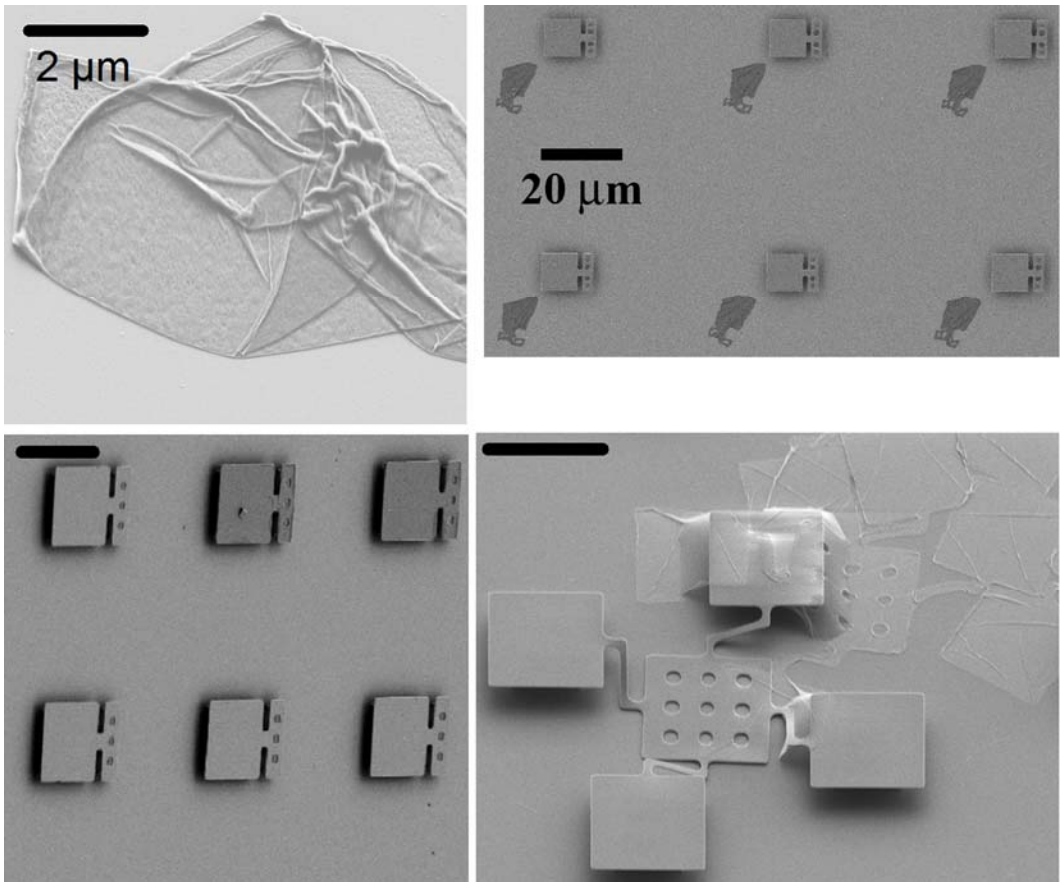

Figure 3-3. Assorted images of photoresist ghosts either on or redeposited on devices and the substrate. In the lower left image, note that two of the six devices shown still have the resist layer bound to the devices, while others do not, posing a problem for subsequent device functionalization. Unlabeled scale bars represent 10 µm.

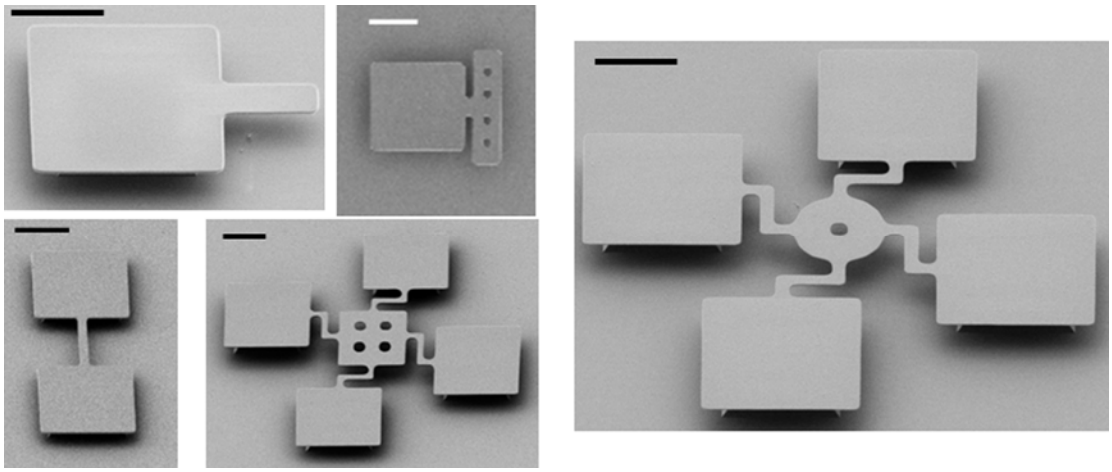

Figure 3-4. SEM images of several different device geometries. Scale bars are 5 μm.

3.2 Resonant Excitation and Detection

In order to excite and detect the motion of the nanomechanical resonators, device chips are mounted within a vacuum chamber that is mounted on a three-dimensional motorized stage. The vacuum ($P < 1$ mTorr) is necessary to avoid the effects of viscous damping, which reduce quality factors by several orders of magnitude in air or liquids. Chips are mounted just behind a vacuum glass window in order to allow laser(s) and imaging optics to reach the devices. In addition, an electrical feedthrough is also present on the vacuum chamber, allowing electrical components to be present in vacuum.

Device resonance is typically excited in one of two ways. First, a 405 nm modulated laser beam can be focused on the device in order to create periodic thermal oscillation in the device. As a result of thermal expansion of the nitride as well as mismatch between the thermal expansion silicon nitride and the silicon dioxide anchor, devices will then resonate when the modulation frequency is tuned to one of their resonant frequencies. This, however, assumes that the device layer will absorb

the incident laser wavelength, which is affirmed by data in Figure 3-2 showing an elevated extinction coefficient, κ, as ultraviolet wavelengths are approached. The physics underlying this excitation method have been previously studied.[1]

This process is, however, a double-edged sword, in that excessive laser powers will induce a thermal drift which will also cause the resonant frequency to drift. In the case of doubly clamped beams, the resonance can become highly unstable as well. In addition, this is a localized excitation method that works well with singly clamped devices like cantilevers or cantilevered paddles but does not for devices with multiple clamping points. In these cases, resonances are often non-linear and unstable due to the non-uniform excitation.

The second method of excitation is based on an external piezoelectric element that works equally well for all device geometries due to the widespread excitation. Resonator chips are mounted on an inexpensive piezoelectric buzzer (on the order of $1) purchased from Radio Shack. While these buzzers are made for audible frequencies up to 20 kHz, they do surprisingly well in the 1-100 MHz range, too. By simply driving them with a modulated source from a spectrum analyzer (using the aforementioned electrical feedthrough on the vacuum chamber), the piezoelectric material translates the electrical input signal into mechanical vibrations, shaking entire resonators as well as entire chips of resonators. Not only does this excitation technique avoid heating the devices, it makes it much easier to excite higher order and more complex resonant modes that would require tedious accuracy to focus the excitation laser at just the right location so as to set up thermal gradients in the right way to incite device motion. Figure 3-5 is a diagram showing how individual devices are addressed and excited.

However, these buzzers were often observed to add “shoulders” to resonator peaks or additional phantom resonances to the reflected laser signal. Their presence

depended on the drive power and the chip or array location on the piezoelectric buzzer. They were not found to significantly affect peak frequency measurement as long as the real signal is larger and far enough away in frequency. In addition, the *Q* values of these phantom modes are always ~1000 or less and do not depend on chamber pressure. Optical excitation can be (and was) used to confirm these observations.

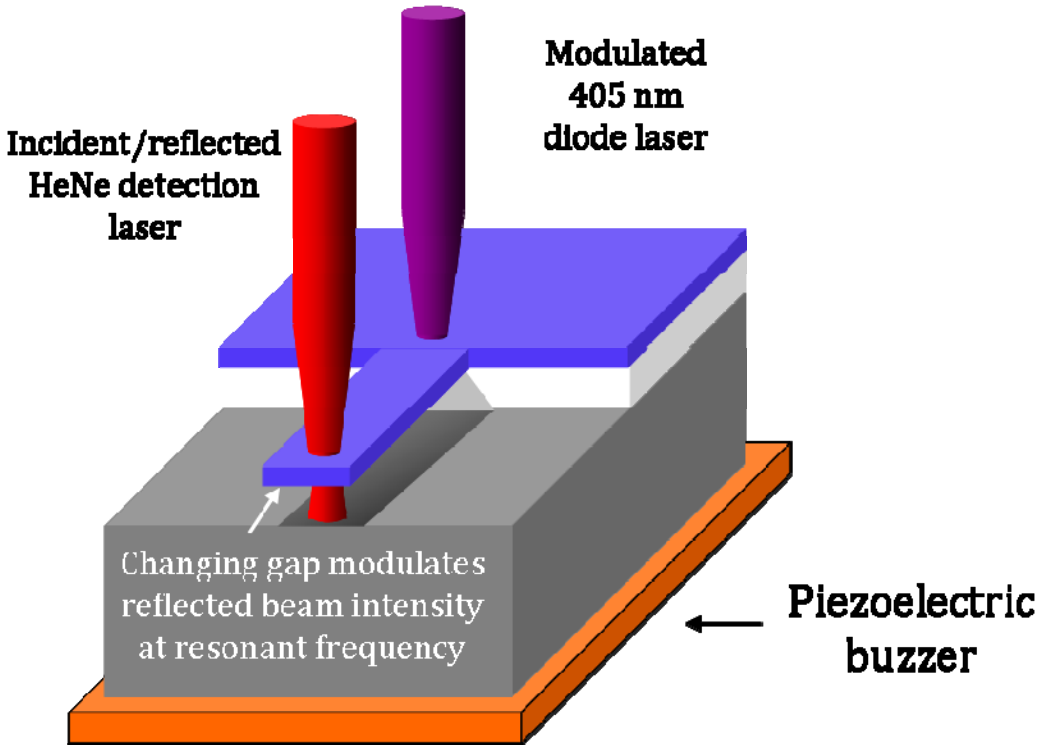

Figure 3-5. Diagram depicting how each device is addressed. Resonance can be excited either with a modulated 405 nm diode laser or by an external piezoelectric buzzer and is detected using optical interference of an incident red HeNe laser, which is described below.

Resonant motion is detected using the optical interference of an incident 632.8 nm HeNe laser with a vibrating device, initially used by Carr and Craighead.[2] Thin film interference is a well understood phenomenon where light interferes with itself when passing through and reflecting from films with thicknesses on the order of the wavelength of light. In fact, this is very commonly used in instruments that measure film thickness—by scanning the incident wavelength and knowing the films and their optical properties, *n* and *k*, the thickness of one or even several films can be determined.

In this case, however, to measure the device resonance, a single wavelength is used, and the materials, their optical properties, and their thicknesses are known. The gap between a resonating device and the chip surface, created by etching the sacrificial layer of silicon dioxide, changes periodically at the resonant frequency of the device. So, as the device modulates this gap thickness, it also modulates the intensity of the reflected HeNe laser beam. This reflected beam then is focused onto a fast photodetector that separates the AC portion of the laser power and sends this signal to a spectrum analyzer which can then find the resonant frequency of the device. While using higher laser powers can increase the amplitude of reflected signals, it also increases the amount of laser power absorbed by the device, which could result in undesirable heating effects. Typically, laser powers at the chip range from 20-100 μW but will vary based on how much of the beam intersects with the device cross-section. In-plane (lateral) modes have also been detected using this technique, where device motion modulates the amount of resonator area interacting with the incident laser beam rather than the gap thickness below the device layer.[3]

This technique, however, is very sensitive to the film thicknesses, and some time needs to be spent considering the appropriate thicknesses to deposit while fabricating devices. It is entirely possible that the thin film interference will result in

perfect destructive interference and no beam would be reflected! Or, it could be at such a configuration that the reflectivity is not very sensitive to changes in gap thickness, perhaps at a local maxima or minima, and excessive laser power must be used in order to get a measurable signal. The underlying mathematics and optical physics have been described in detail elsewhere,[4] but will be briefly discussed below:

As the incident laser beam approaches the device stack it can reflect from or transmit through interfaces between differing indices of refraction and be attenuated by passing through media with non-zero extinction coefficients. These interactions can be approached using a matrix based approach using the convention that E^+ refers to the electric field of light moving along the direction of the incident laser beam (towards the silicon substrate) and E^- refers to light moving in the opposite direction. These can be described by the following relationships

$$\begin{pmatrix} E_i^+ \\ E_i^- \end{pmatrix} = \frac{1}{2}\begin{pmatrix} 1+\alpha_i & 1-\alpha_i \\ 1-\alpha_i & 1+\alpha_i \end{pmatrix}\begin{pmatrix} E_{i+1}^+ \\ E_{i+1}^- \end{pmatrix} = I_i \begin{pmatrix} E_{i+1}^+ \\ E_{i+1}^- \end{pmatrix}$$
$$\begin{pmatrix} E_0^+ \\ E_0^- \end{pmatrix} = \begin{pmatrix} e^{-i\delta_i} & 0 \\ 0 & e^{i\delta_i} \end{pmatrix}\begin{pmatrix} E_f^+ \\ E_f^- \end{pmatrix} = T_i \begin{pmatrix} E_f^+ \\ E_f^- \end{pmatrix} \quad (3\text{-}1)$$

where

$$\alpha_i = \frac{n_{i+1}}{n_i}$$
$$\delta_i = 2\pi \frac{d_i}{\lambda} n_i \quad (3\text{-}2)$$

and n_i and d_i are the complex index of refraction and the thickness of the i^{th} layer, respectively. So, as the light passes through the resonator device layer, two interfacial matrices, *I*, and one transmission matrix, *T*, will be needed to describe the interaction.

This powerful method works for any number of films, allowing the matrices to be multiplied, forming a single matrix describing the film stack, *M*, such that

$$\begin{pmatrix} E_0^+ \\ E_0^- \end{pmatrix} = I_0 T_0 I_1 T_1 \cdots T_n I_n \begin{pmatrix} E_n^+ \\ 0 \end{pmatrix} = M \begin{pmatrix} E_n^+ \\ 0 \end{pmatrix} \tag{3-3}$$

While this formulation allows for light to be incident from both directions, in the present setup, light is only incident from one side of the film stack (no light originates from the silicon wafer), simplifying the electric field term on right hand side of Equation (3-3). The reflection and transmission coefficients, *R* and *T*, describe the percentage of light reflected from and transmitted through a film stack and are related to the intensities of light rather than the electric field. Because intensity scales as the square of the electric field, the reflection and transmission coefficients will depend on the square of elements in the film stack matrix, *M*, and are given by the following

$$\begin{aligned} R &= \frac{I_0^-}{I_0^+} = \left| \frac{M_{21}}{M_{11}} \right|^2 \\ T &= \frac{I_n^+}{I_0^+} = \frac{n_{r,n}}{n_{r,0}} \frac{1}{\left| M_{11} \right|^2} \\ A &= 1 - R - T \end{aligned} \tag{3-4}$$

where *A* is the percentage of light absorbed by the film stack.

Using the measured values for low stress silicon nitride, shown in Figure 3-2, with the accepted values for the complex index of refraction of silicon, *A*, *R*, and *T* can be calculated. Figure 3-6 shows these values as a function of gap thickness, formerly the silicon dioxide thickness between silicon nitride and the silicon wafer, for 632.8 nm wavelength light incident on the present film stack of vacuum, 90 nm low stress

silicon nitride, vacuum gap, and the silicon wafer. It is useful to note the amount of light absorbed by the device layer, which in this case varies only slightly and is less than 10% of the incident power at any gap thickness. If possible, this should be kept at a minimum to avoid thermal drift and instabilities or drifts in resonant frequency.

Knowing this periodic behavior, it is necessary to select and grow the appropriate film thicknesses in order to facilitate and optimize readout of device resonances. It is important to keep in mind that small changes in the gap thickness due to device motion (roughly on the order of 0.1 to 1 nm) need to be translated into measurable perturbations of the reflection coefficient, so using film thicknesses near local extrema (such as near 1725 or 1875 nm) must be avoided. Rather, regions with the highest slope of R with respect to changing gap thickness should be used. The data in Figure 3-6, however, changes with the silicon nitride thickness; to fully analyze the detection sensitivity, a contour plot is more appropriate for finding the optimal film stack, such as the one shown in Figure 3-7(a).

To more clearly show the most sensitive film stack thickness combinations, the sensitivity to device resonance, given by the absolute value of the partial derivative of the reflection coefficient with respect to gap thickness, is shown in Figure 3-7(b). The regions of highest sensitivity result in high amplitude resonance peaks read out by the spectrum analyzer and minimize the amount of laser power absorbed by the devices. Typically around 90 nm of silicon nitride is used for resonators, because thinner devices are more sensitive to added material, as will be discussed later. While the periodic nature of Figures 3-6 and 3-7 allow several silicon oxide thicknesses to be used with 90 nm thick silicon nitride, such thin devices are often susceptible to stiction, a phenomenon where MEMS or NEMS devices are flexible enough to come in contact with the substrate where they remain permanently stuck. Typically this process occurs after device release in hydrofluoric acid. As the rinse water is dried

from the device chips, small water menisci form underneath devices and pull them down to the silicon surface. When a force is applied to cantilevers, the tip deflection is proportional to the square of the length over the cube of its thickness, so for such thin devices, a large silicon dioxide thickness is required to avoid device stiction and maximize yield. When 90 nm silicon nitride films are used, gap thicknesses ranging from 1810 to 1870 are optimal; typical silicon dioxide growths have resulted in 1825-1840 nm thicknesses, where stiction is rarely observed, except for when devices are too long, or excessive release times in HF are used. 6 μm long cantilevers typically survive the initial release, but begin to stick later if used for sensing and additional materials are added to them.

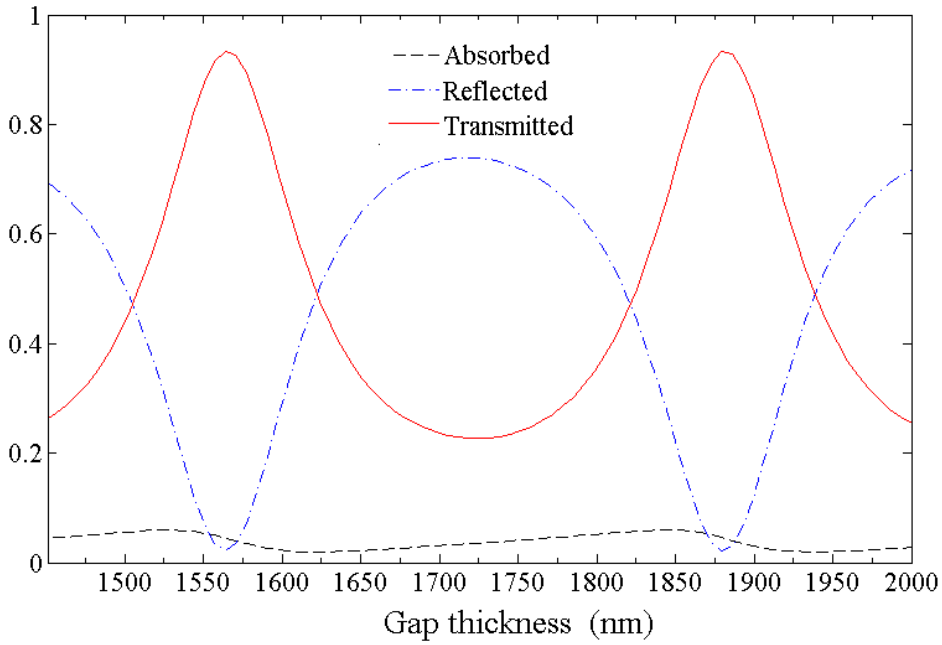

Figure 3-6. Plot of absorbed, reflected, and transmitted light from a device stack with 90 nm thick device layer and an incident wavelength of 632.8 nm (HeNe).

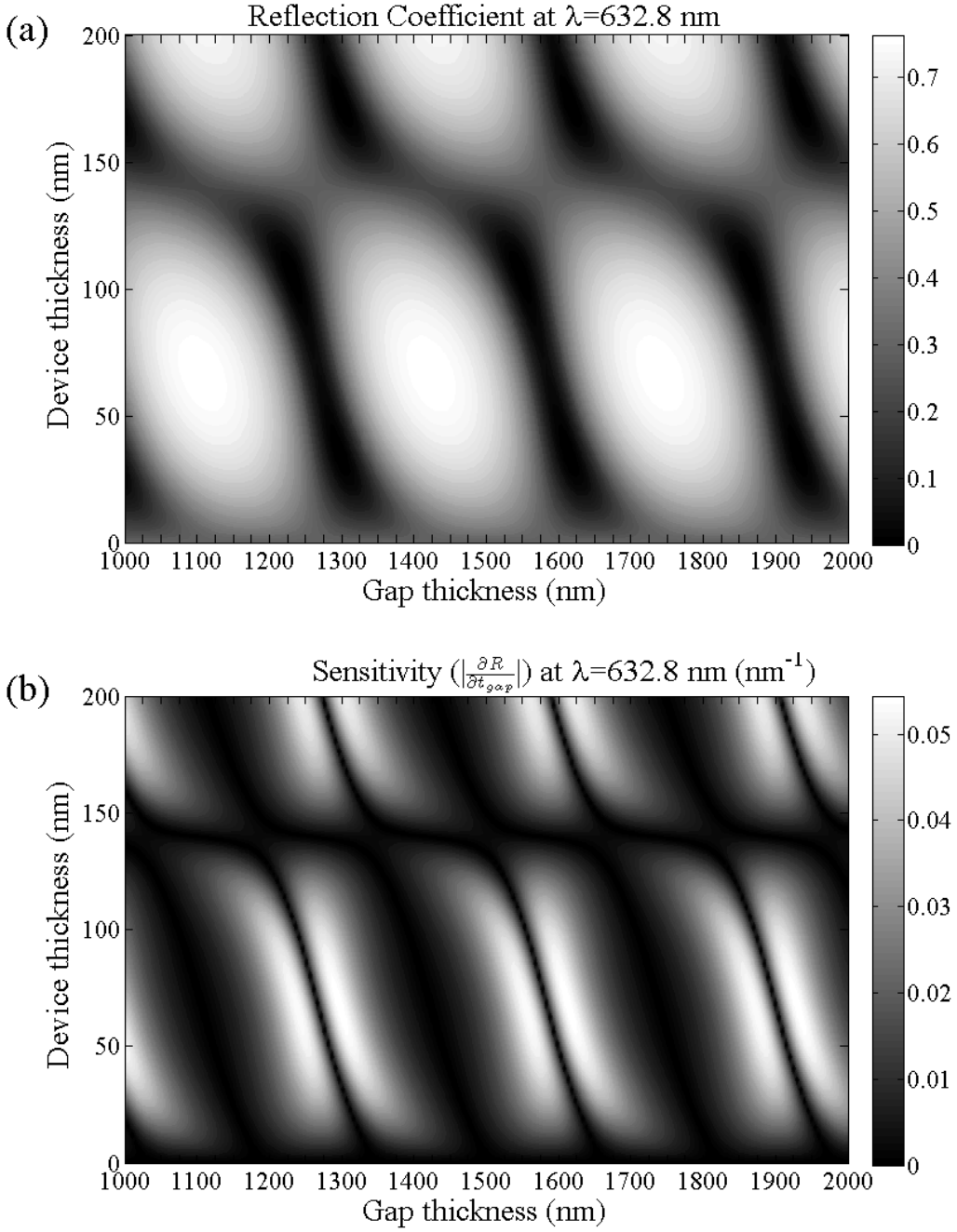

Figure 3-7. (a) Reflection coefficient from the device film stack as a function of low stress silicon nitride thickness and underlying gap thickness. (b) Sensitivity as a function of the same variables, given by the absolute value of the derivative of reflectance with respect to the gap thickness. The higher the sensitivity, the greater the amplitude of modulation is in the reflected laser beam.

The experimental apparatus used to interface the devices with the lasers and electronics is shown schematically in Figure 3-8. The detection laser, a linearly polarized, 30 W HeNe laser (632.8) and the optional 405 nm diode laser used for device excitation are combined and sent towards the sample chamber at a standard beamsplitter. The diode laser first passes through an electro-optic modulator (EOM) which is used to modulate the intensity of the input beam at a particular frequency, which is then tuned to the device resonant frequency allowing optical excitation of device resonance. It then enters the optical path through two extra mirrors in order to allow alignment of the blue laser separately from the red, which is very important for optical excitation where the diode laser must be focused near a clamping point of the device and the HeNe laser must be focused farthest away from clamping points where out-of-plane motion maximizes the interference effects and therefore the strength of the output signal. This combining beamsplitter is a convenient location at which to monitor laser powers, as long as the effects of the remaining optical components on the laser powers are known such that laser power incident upon each device can be known. Here and in a two other locations are optical filters that allow the red, detection laser to pass while blocking the excitation beam. Just before combining the beams, each laser path goes through a rotating, variable neutral density filter allowing the powers of each laser to be changed separately.

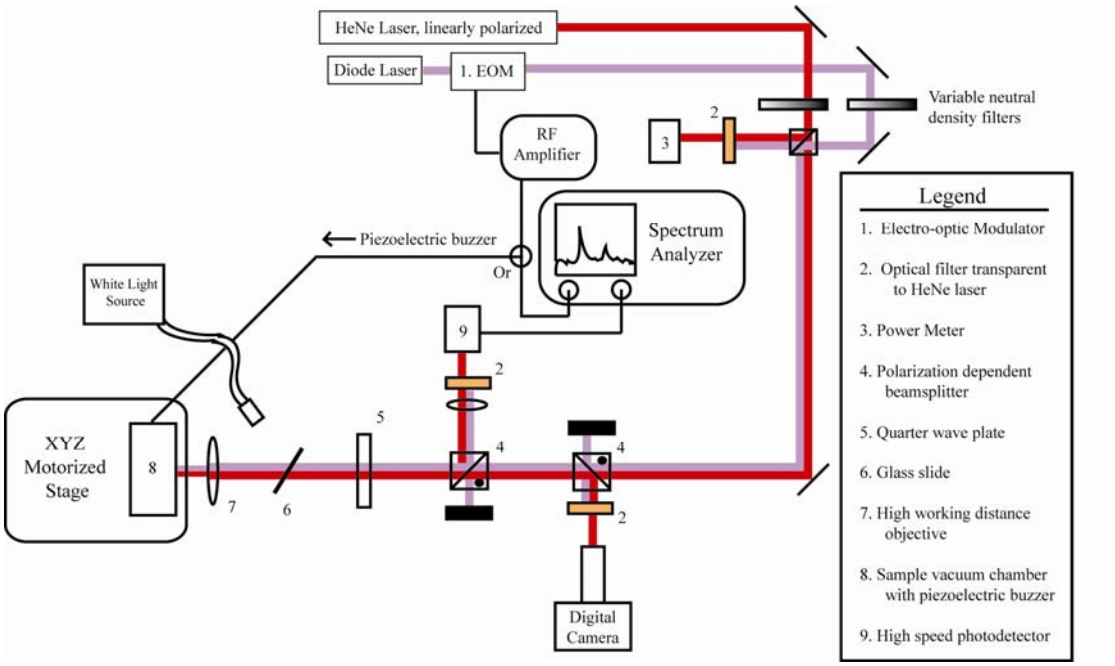

Figure 3-8. Schematic of the optical bench setup used to excite and read out device resonances.

The next two optical components are polarizing beamsplitters, used essentially to minimize losses in the detection, HeNe laser. Because these beamsplitters split the incident beam into two orthogonal linearly polarized states, proper rotation of the HeNe laser will allow the beam to pass straight through both with nearly no loss in power. Next, a quarter wave plate is used to change the linearly polarized light into circular polarization. This is useful because once the light reflects off of the device stack and re-enters the quarter waveplate, it is converted back into linear polarization, but orthogonal to the incident polarization, meaning that most of the reflected beam will be diverted to the high speed photodetector, avoiding potential losses in signal going through the beamsplitter.

A 20x long working distance objective is used to focus the white light and lasers onto the resonators. The long working distance is required because of the

separation needed for the vacuum chamber window behind which the devices are mounted. The glass slide is used to couple in white light from a fiber optic illuminator, allowing visualization of the devices and therefore providing the capability to align laser spot(s) to them. The white light and a small amount of the laser beams will pass back through the polarizing beamsplitters to a digital camera, which provides a live view of the devices and lasers, facilitating laser alignment. A removable filter is often placed in front of the camera to block out the detection beam when not aligning it.

The majority of the reflected detection laser will be diverted towards and focused on the high speed photodetector. Another filter is present to block out the modulated excitation laser if used. The photodetector decomposes the input power into an AC component and a DC offset; the AC portion is then sent to the spectrum analyzer which then transforms the signal into frequency space and allows study of the device resonance(s). The spectrum analyzer outputs the swept frequencies to either the EOM or the piezoelectric element located in the sample vacuum chamber as it reads in the device response from the photodetector.

A radio frequency (RF) amplifier is needed to significantly boost the amplitude of the swept signal into 10s of volts as required by the EOM. In addition, the EOM requires a DC offset of 60-70 V, which attenuates the input beam to some degree but more importantly sets a mid-point to the modulation, which can determine the linearity of the drive. For instance, Figure 3-9 shows the output diode laser power as a function of the DC offset in the EOM. When the boosted AC signal is added to this offset, the output power then oscillates up and down this curve depending on the amplitude. So, it is very important to avoid setting the DC offset to around 120 V, as modulation in the voltage will result in very little modulation of the beam intensity, though it could be used for 2f frequency excitation. The curve is fairly linear around 50 to 80 V as

well as 180-240 V, meaning either would work well for maximizing the amplitude of modulation and thus device excitation.

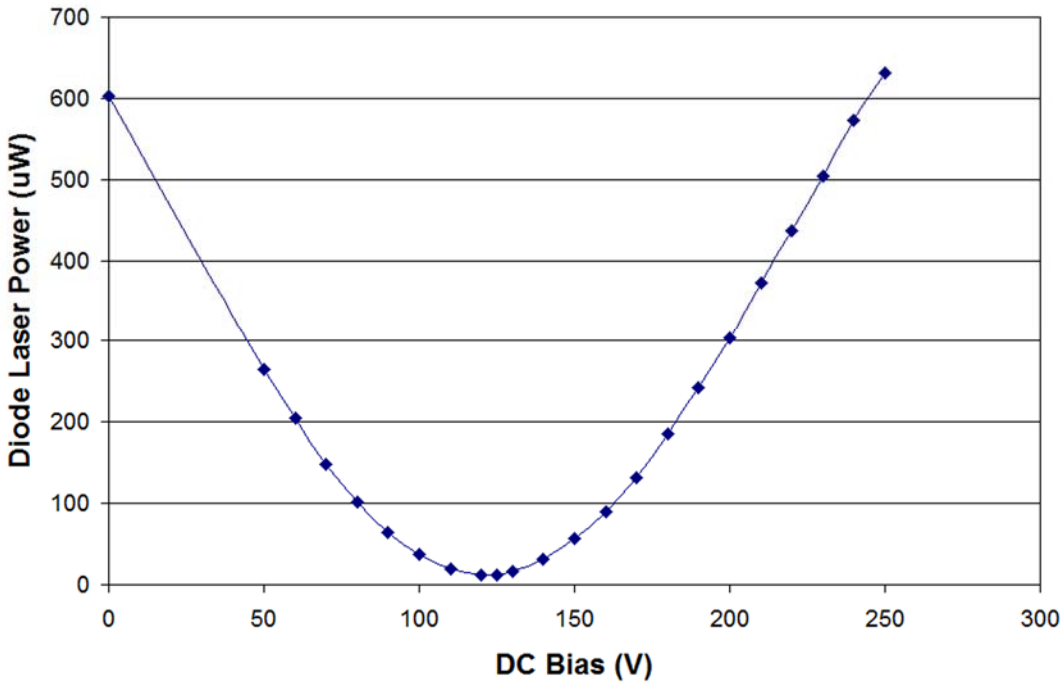

Figure 3-9. Plot of the EOM attenuation characteristics used to modulate excitation laser power.

3.3 Resonator Arrays

The small size of these resonators encourages fabrication of large arrays of them in fairly small areas (ranging from the orders of 0.01 to 10 mm^2) simply from the standpoints of geometry, efficiency, and thriftiness. However, do any good reasons for doing this exist, either from an experimental or application-based standpoint? Certainly, statistics dictates that larger sample sizes are more representative of the behavior of entire populations, so having many devices on each chip would improve

the measurements accordingly. Also, the use of high density arrays would allow for rapid prototyping and characterization of devices as many different sizes and geometries could be located in close proximity on a single chip. On-chip redundancy offers several reasons to have multiple arrays of devices on each chip as well: to allow for accidental scratches, unfortunate dust or debris that lands on the surface, or imperfections that may arise during fabrication or experiments. In terms of sensor applications, it is more compelling if many resonators agree with a particular detection event, rather than having just one or two devices doing the sensing. In addition, high densities of arrays on chip are analogous to microarray techniques and may ultimately lead to high levels of multiplexing on a miniaturized platform. It should be noted that optical drive and detection as well as external piezoelectric excitation all lend themselves well to high density arrays of devices, as they are independent of device separation, unlike electrical techniques which need electrical access to each device individually on-chip, taking up much real estate.

The above material discusses the mechanisms and apparatus used to measure a single device after some time is spent positioning the device appropriately such that the laser is focused on the proper area. In addition, after first finding the resonance signal in the reflected light, the spectrum analyzer must be configured to zoom in on the peak and take several averages of the zoomed-in spectrum in order to have sufficient data points along the curve and reduce the effects of noise. Then the resonant frequency can finally be determined. If available, this data can be output to a computer that then fits the resonance peak to a Lorentzian curve and accurately determines the resonant frequency and quality factor. This process quickly becomes time-consuming when wanting to measure more than just a few devices.

In order to solve this problem, the two limiting components—the spectrum analyzer and stage— can be automated and controlled using a computer and GPIB

communication. This is done using LabVIEW (National Instruments) software, a graphical programming environment typically used for automation, data collection and analysis, and more. Figure 3-10 shows schematically how this fits together with the current setup.

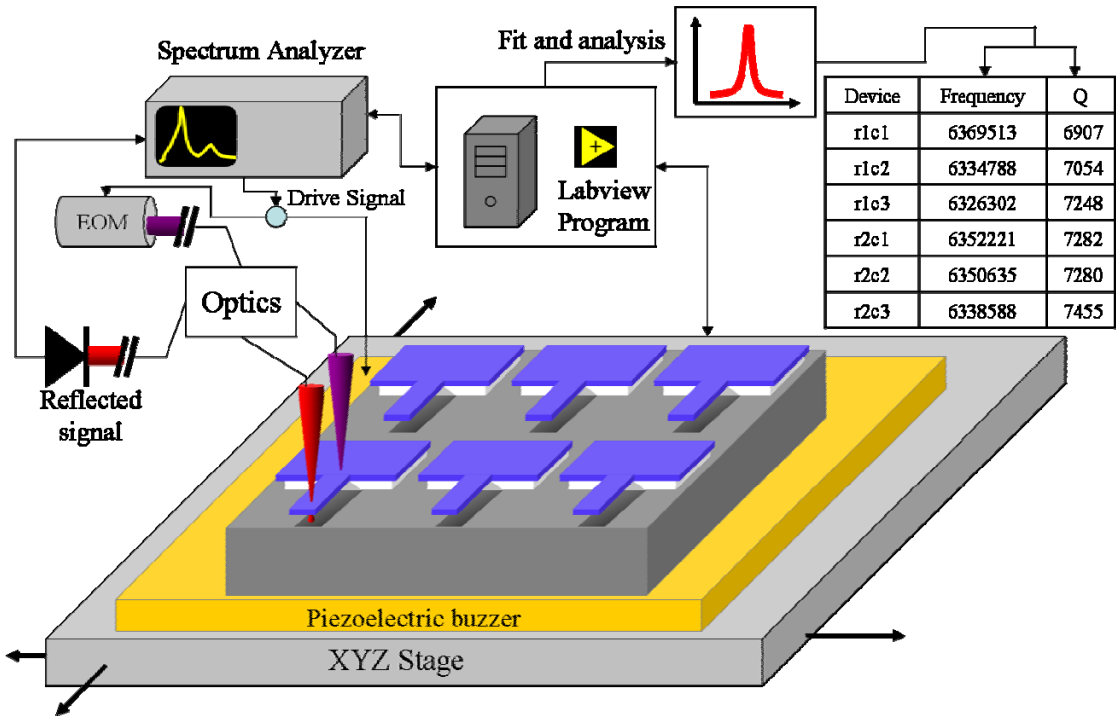

Figure 3-10. Schematic of automated setup where a computer controls the spectrum analyzer and motorized stage, analyzes the data, and returns it in an easy-to-read and use format.

While the groundwork for this automation was previously laid, consisting of basic communication and analysis routines set up for single device measurement as well as one developed to measure a single array. Essentially, this program searches for a device peak in a spiral pattern, then moves to the next device in the array, repeats the spiral search, and so on until measuring the entire predetermined array. However, this array program wrote an individual data file for each resonator that later had to be

opened in order to extract frequency and quality factor data that would later be needed to analyze frequency shifts in sensor experiments, for instance. After optimizing the data output format, a summary file containing devices, frequencies, and quality factors, like that shown in Figure 3-10, was added to the output, significantly reducing analysis time. With this program, devices could be measured one array at a time, which typically took anywhere from 30-60 seconds per device, depending on the amount of searching necessary to find the peak.

After further optimizing the communication and analytical algorithms, this measurement time was reduced an order of magnitude to about 4-6 seconds per device! Another layer of automation was added to the design so that a single routine could measure any number of arbitrarily chosen arrays of devices from a large 'superarray' of arrays on chip. Without these rapid, automated readout capabilities, much of the work to be presented below would not have been possible due to the sheer multitude of devices that needed to be measured and analyzed. Such rapid automation is also encouraging for future applications of arrayed micro and nanomechanical resonators.

REFERENCES

1. B. Ilic, S. Krylov, K. Aubin, R. Reichenbach, and H. G. Craighead, "Optical excitation of nanoelectromechanical oscillators," *Appl. Phys. Lett.* **86** (2005) 193114.

2. D. Carr and H. G. Craighead, "Fabrication of nanoelectromechanical systems in single crystal silicon using silicon on insulator substrates and electron beam lithography," *J. Vac. Sci. Technol. B* **15**(6) (1997) 2760.

3. B. Ilic, S. Krylov, M. Kondratovich, and H. G. Craighead, "Selective Vibrational Detachment of Microspheres Using Optically Excited In-Plane Motion of Nanomechanical Beams," *Nano Lett.* **7** (2007) 2171.

4. K. L. Aubin, "Radio Frequency Nano/Microelectromechanical Resonators: Thermal and Nonlinear Dynamics Studies," Ph.D. Dissertation, Cornell University, Ithaca, NY, 2005.

CHAPTER 4

RESONANT MEMS SENSOR PHYSICS*

This chapter highlights and expands upon key issues briefly introduced in Section 2.2 that are crucial for describing the work discussed in the remainder of this thesis. Initially, the focus will be on cantilever resonators, as they are the canonical device geometry, their equations of motion have straightforward solutions, and they are the most commonly used resonant sensor geometry in the literature. These early sections will lay the groundwork for addressing more interesting geometries and the more complex questions broached and answered in later sections. Based on the discussion in Section 2.2.2 and recent theoretical work[3,4] surface-stress effects are neglected in the remainder of this work since they are very small in magnitude for singly-clamped cantilevers and the topic still under much debate in the literature.

A major focus of this chapter is studying the effect of device geometry, which is explored once the traditional cantilever case is fully introduced. Deviations from the simple rectangular cantilever are rarely found in the sensing literature, which could be attributed to tradition as well as the relative simplicity of the mathematics involved. It is unclear whether more complex device geometries would work better or be more sensitive than cantilevers, but it is not obvious that they would be any worse. As is fully discussed below, it was found that more complex resonator designs can outperform cantilever devices when the material sensed by the cantilever is bound sparsely across the device. In this case, device sensitivity becomes a strong function of analyte binding location. Also discussed in this chapter is the effectiveness of using higher harmonics or higher resonant modes of devices for sensing.

* Some parts of this chapter can be found in full detail in the literature. Sections 4.3, 4.4.1, and 4.5 are adapted from Reference [1]. Section 4.4.2 highlights results published by P.S. Waggoner *et al.*[2]

4.1 Underlying Physical Concepts

4.1.1 Sensing Pathways

The frequency and mode shape for resonant mechanical sensors can be derived from classical beam theory for simple beam geometries. Flexural vibrations of beams, cantilevered or doubly clamped alike, are described by the following differential equation, derived from dynamic equilibrium[5]

$$\frac{\partial^2}{\partial x^2}\left(EI\frac{\partial^2 v}{\partial x^2}\right) = -\rho A\frac{\partial^2 v}{\partial t^2} \tag{4-1}$$

where E is Young's modulus or stiffness, I is the second moment of area (also called second moment of inertia), v represents the transverse displacement of the beam during vibration, ρ is density, and A is the cross-sectional area of the beam given by the product of width, w, and thickness, t. Note that the product of E and I is called the flexural rigidity, often designated by D. For beams of constant cross section, the flexural rigidity is constant along the length of the beam, allowing simplification of Equation (4-1) to

$$\frac{\partial^4 v}{\partial x^4} = -\frac{1}{a^2}\frac{\partial^2 v}{\partial t^2} \tag{4-2}$$

where

$$a = \sqrt{\frac{EI}{\rho A}} \tag{4-3}$$

This expression can be solved using separation of variables with a solution of the form

$$v(x,t) = X(x)\left(A\cos\omega t + B\sin\omega t\right) \tag{4-4}$$

that when inserted into Equation (4-2) gives the following

$$\frac{d^4X}{dx^4} = \frac{\omega^2}{a^2}X \tag{4-5}$$

After making the following substitutions

$$\begin{aligned} k^4 &= \frac{\omega^2}{a^2} \\ X(x) &= e^{rx} \end{aligned} \tag{4-6}$$

we obtain the following

$$\begin{aligned} &\frac{d^4X}{dx^4} - k^4X = 0 \\ &e^{rx}\left(r^4 - k^4\right) = 0 \end{aligned} \tag{4-5}$$

Solving this equation for r gives solutions of $\pm k$ and $\pm ik$ and leads to an expression for $X(x)$ of the form

$$X(x) = A\sin kx + B\cos kx + C\sinh kx + D\cosh kx \tag{4-6}$$

Applying the proper boundary conditions allows determination of resonant frequencies and mode shapes. For cantilevered beams, the boundary conditions are as follows

$$X(0) = 0 \qquad \left.\frac{dX}{dx}\right|_{x=0} = 0 \qquad \left.\frac{d^2X}{dx^2}\right|_{x=l} = 0 \qquad \left.\frac{d^3X}{dx^3}\right|_{x=l} = 0 \tag{4-7}$$

Applying these to Equation (4-6) results in an expression for the mode shape and a restricted set of allowed values for k, given by the following

$$\begin{aligned} X(x) &= A(\cos kx - \cosh kx) + B(\sin kx - \sinh kx) \\ k_i l &= \{1.875, \quad 4.694, \quad 7.855, \quad 10.996, \quad \cdots\} \end{aligned} \tag{4-8}$$

The fundamental mode and its harmonics come from Equation (4-8), where adjacent modes are subject to the usual orthogonality conditions imposed by eigenvalue equations. The first three resonant mode shapes for a cantilever are shown in Figure 4-1.

After solving for k, it can be placed back into Equation (4-6) to give an equation for the resonant frequency of each mode

$$f = \frac{\omega}{2\pi} = \frac{a k_i^{\,2}}{2\pi} = \frac{k_i^{\,2}}{2\pi}\sqrt{\frac{EI}{\rho A}} \tag{4-9}$$

Beams with other clamping configurations, such as doubly-clamped or fixed-fixed beams, have a similar form as Equation (4-9), but with different values of k_i as defined by the slightly different boundary conditions.

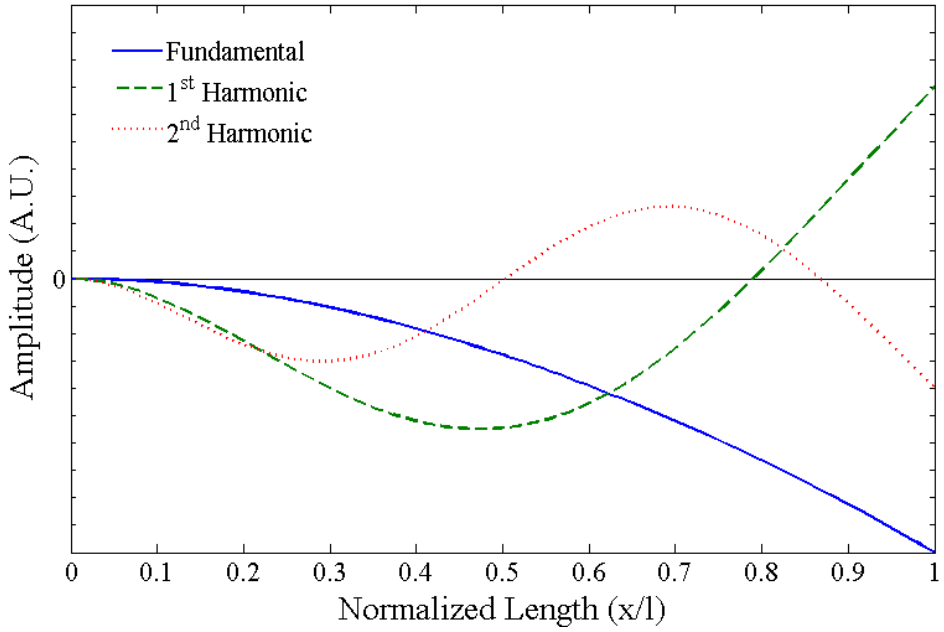

Figure 4-1. Plot of first three flexural vibration modes of a cantilever.

Applying Equation (4-9) to the fundamental mode then gives

$$f_0 = \frac{3.515}{2\pi}\sqrt{\frac{EI}{\rho A l^4}} = \frac{3.515}{2\pi}\sqrt{\frac{D}{ml^3}} \tag{4-10}$$

For a cantilever with a rectangular cross section, I is given simply by $wt^3/12$ for transverse resonant modes. Expanding Equation (4-10) with expressions for I and A, results in

$$f_0 = \frac{3.515}{2\pi}\frac{t}{l^2}\sqrt{\frac{E}{12\rho}} \tag{4-11}$$

While Equation (4-11) is useful for characterizing films (using cantilevers of different lengths and plotting f vs. t / l^2) or predicting resonant frequencies, it can be

difficult to use when films are being added – as added materials must be thought of with respect to an average density or an effective, composite beam stiffness. Conceptually and mathematically, it is easier to work from Equation (4-10) when establishing sensing mechanisms and characterizing frequency shift behaviors.

In doing so, the discussions of Section 1.2 and the logistics of sensing must be considered. To perform best as a sensor, the cantilever needs to capture or bind materials on its surface, whether it is evaporated metals, condensing water vapor, or biomolecules binding out of solution. Surface-to-volume ratio then becomes a key factor—ideally the sensor should be able to capture as much material as possible for a given set of conditions. A high surface-to-volume ratio should also reduce the initial sensor properties of mass and thickness, making them more sensitive added material. High surface-to-volume ratio cantilevers can easily be made from thin film materials, with the added benefits of thin film deposition and etching being a mature microfabrication technology with many different material choices available.

Cantilevers made from thin film materials will feature a thickness, t, much less than their width, w, or length, l, naturally suggesting that t will be closely related to sensor applications as well as the sensing capabilities and limits. Using this condition in conjunction with Equation (4-10), it becomes evident that the two important sensing pathways are flexural rigidity and mass. For very small changes in these quantities, a Taylor expansion can be used to approximate the new frequency, f_1 as

$$\frac{\Delta f}{f} = \frac{1}{2}\left(\frac{\Delta D}{D} - \frac{\Delta m}{m}\right) \tag{4-12}$$

Within the flexural rigidity is stiffness and thickness of the added layer (neglecting changes in width), and the added mass similarly depends on the density and thickness

of the added material. If, however, the changes become large, then the full version must be used, starting from Equation (4-10),

$$\frac{\Delta f}{f} = \frac{C\sqrt{\frac{D'}{m'}} - C\sqrt{\frac{D}{m}}}{C\sqrt{\frac{D}{m}}} = \sqrt{\frac{D'/D}{m'/m}} - 1 \tag{4-13}$$

From this point, there are many ways in which Equations (4-12) and (4-13) evolve based on where and how much of the material is added, what the device geometry is, and what resonant mode is used for sensing. These situations will be discussed in full detail later in Sections 4.2 – 4.4.

4.1.2 Quality Factor

The quality factor, as mentioned earlier in Section 2.2.1, describes the energy dissipation of the system and has a role in determining the resolvability of two adjacent resonant peaks. In frequency space, the resonance peak takes the form of a Lorentzian curve, given by the following

$$A(f) = \frac{1}{\pi} \frac{\frac{1}{2}\Gamma}{(f - f_0)^2 + (\frac{1}{2}\Gamma)^2} \tag{4-14}$$

where Γ is the full width of the peak at half of its maximum and f_0 is the frequency at its peak. Quality factor is defined by the peak center over the full width at half maximum (f_0 / Γ) when the amplitude is in units of energy. If looking at only the

amplitude of the signal, the full width at $2^{-½}$ of the maximum is used, as the energy is related to the square of the amplitude.

When used for sensing, the shift in peak frequency from the initial resonance peak to the final one must be measured, requiring that the two neighboring peaks are resolvable. This resolution is primarily determined by the quality factor, as smaller changes can be detected when the peaks are sharper, which led to Equation (2-4) where the minimum detectable mass change is inversely proportional to quality factor. Ideally, an infinite quality factor would appear to be a Dirac delta function, giving infinite resolution. For example, several Lorentzian curves with quality factors ranging from 100 to 5000 are plotted in Figure 4-2.

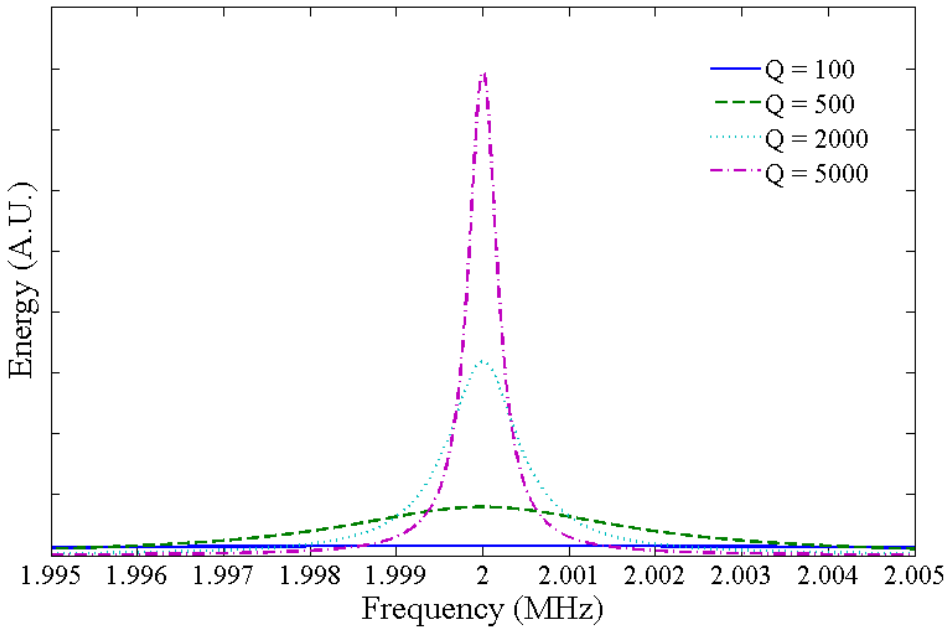

Figure 4-2. Plot of several resonance peaks with varying quality factor. There is sharp contrast between the $Q = 5000$ peak and the $Q = 100$ peak, which does not even appear to be Lorentzian over this frequency span.

Since Q also describes the energetics of the resonance, it is important to consider the many different loss mechanisms that can reduce it, and in fact, energy dissipation quantities are often given as Q^{-1}. The actual measured quality factor is determined much like resistors in parallel, given by

$$\frac{1}{Q_f} = \sum_i \frac{1}{Q_i} \tag{4-15}$$

where Q_i represents a wide array of different loss mechanisms. In vacuum, typical MEMS and NEMS resonators have quality factors on the order of 10^3 to 10^5. It is worth noting that there have been some recently fabricated nanomechanical devices with impressively high quality factors of 3 x 10^5 up to 10^6, that are a result of high stress either built into or applied to the nanostring resonators.[6,7]

Sources of energy loss have been studied a great deal in the literature, however, only a handful are relevant when discussing realistic sensor scenarios. For example, in the quest for single Dalton mass sensitivity, the limits of Q in ultra-high vacuum and loss mechanisms that can be avoided at extremely low temperatures have been studied,[8] however other loss mechanisms quickly dominate these effects in sensing applications. In addition, clamping losses are often considered for devices operated in vacuum and describe energy losses from the device into the bulk material and/or substrate.

Making smaller, more sensitive resonators also inevitably leads to a larger surface to volume ratio, which is an important loss mechanism. In fact, Yasamura *et al.*[9] found that cantilevers thinner than about 1.2 μm had a linearly decreasing quality factor as device thickness was reduced, pointing to surface losses. In this same work, the cantilever material also played a significant role in Q, where single crystal silicon

has the lowest losses, then followed by silicon nitride and polysilicon, in order. Similar results were also observed in recent work on nanostring resonators, where quality factors were found to be limited by surface-to-volume ratio until other more lossy effects took over.[10]

The key issue to keep in mind is that in order for these resonators to be used for sensing a *specific* analyte, they need to be coated with some selective material. Even if one were to make the world's smallest, highest Q nanoresonator with a Q of a billion and sub-Dalton mass sensitivity, it would need a specific capture layer (that would likely reduce Q significantly), otherwise it could just as easily detect a molecule of vacuum pump oil as it could a caffeine molecule—and noone would be able to tell which actually bound.

Unfortunately, surface functionalization or coating the device with a deposited function layer(s) will decrease the quality factor. Even simply changing the surface termination of a silicon resonator can significantly affect the quality factor. M. A. Hines and colleagues have studied this problem in great detail, and shown that quality factor can vary by up to a factor of 6 for different molecular surface terminations on torsional silicon resonators.[11-14] Methyl termination has given the highest quality factor, followed by hydrogen and then longer alkyl chain molecules. Oxidized surfaces have even lower quality factors. Long term stability of Q, therefore, is related to the rate of surface oxidation, which was found to be much faster for hydrogen terminated surfaces.[13] Devices fabricated in this work are also subject to this effect and decreasing quality factor with storage time is a commonly observed, as the hydrogen termination remaining from HF release is slowly replaced by oxygen.

For some sensor designs it is necessary to coat devices with a polymer layer or a gold film in order to capture certain analytes on the resonators. These coatings present another loss pathway and can significantly reduce quality factor. For instance,

gold layers can easily reduce quality factor by an order of magnitude for films on the order of 10% the thickness of the original device.[15,16] These effects must also be taken into account.

Unfortunately, the most significant loss mechanism has been saved for last—viscous damping. The viscous nature of air and water bogs down device resonances greatly reducing quality factor, strongly decreasing the amplitude of resonance, and shifting the resonant frequency due to the added mass of fluid entrained to the resonator. Not only does the reduced quality factor degrade sensitivity, but the added mass also decreases the sensitivity, effectively making the device more massive. As a result, most resonant sensors are limited to operation in vacuum or in some cases air, giving deflection-based sensors an advantage in real-time biosensing directly in fluids. While operated in vacuum, nanomechanical resonators typically have quality factors on the order of 10^4-10^5, however these values drop several orders of magnitude when operated in air[10,17] (10-100) or liquid[18-21] (1-10). Even nanomechanical resonators with quality factors greater than 10^6 in vacuum are inhibited by viscous damping, reducing the Q to ~1000 at about 1 Torr.[7]

Recently, Basak *et al.* have shed light on the process of viscous damping of resonating cantilevers using finite element analysis.[22] In studying a few different cantilever shapes, their model suggests that wider devices have higher quality factors, and that slotted or necked cantilevers result in reduced quality factors. Observing the fluid shear as a result of these device geometries revealed that shear is very high at all of the edges of the device, which are more numerous in slotted or necked cantilevers, resulting in higher energy dissipation and lower values for Q. Squeeze film effects were also investigated, which become important when the gap between suspended cantilevers and the substrate become comparable to the thickness of the water boundary layer surrounding the cantilever. Recently, Southworth *et al.* took

advantage of squeeze-film effects on polysilicon drumhead resonators and utilized them for pressure sensing, giving impressive linearity over several orders of magnitude.[23]

4.2 Sensor Configurations

When using thin MEMS and NEMS resonators as sensors, there are two main configurations for how material is sensed: bilateral detection, where both device surfaces are coated for specific binding, and unilateral detection where only one (usually the top) surface of the device is functionalized. These categories are delineated by the assumption that the resonators are much thinner than they are wide and long, which has been justified in above discussions. In the next two sections, these sensing modes will be defined and Equation (4-13) will be elaborated on in each case.

In order to expand Equation (4-12) or (4-13) for these two configurations, the change in flexural rigidity needs to be determined. This can be done using the equivalent beam method presented by Timoshenko,[24] in which composite beams are modeled as homogeneous beams with an altered cross section. The width of an added layer is scaled by the ratio of its stiffness to that of the original material, as shown in Figure 4-3. Once scaled, the added materials retain their density and thickness but are now considered to have a stiffness of E_0. Once the equivalent beam is formed, then new flexural rigidity can be determined using the initial stiffness and a new value for the second moment of the area, I.

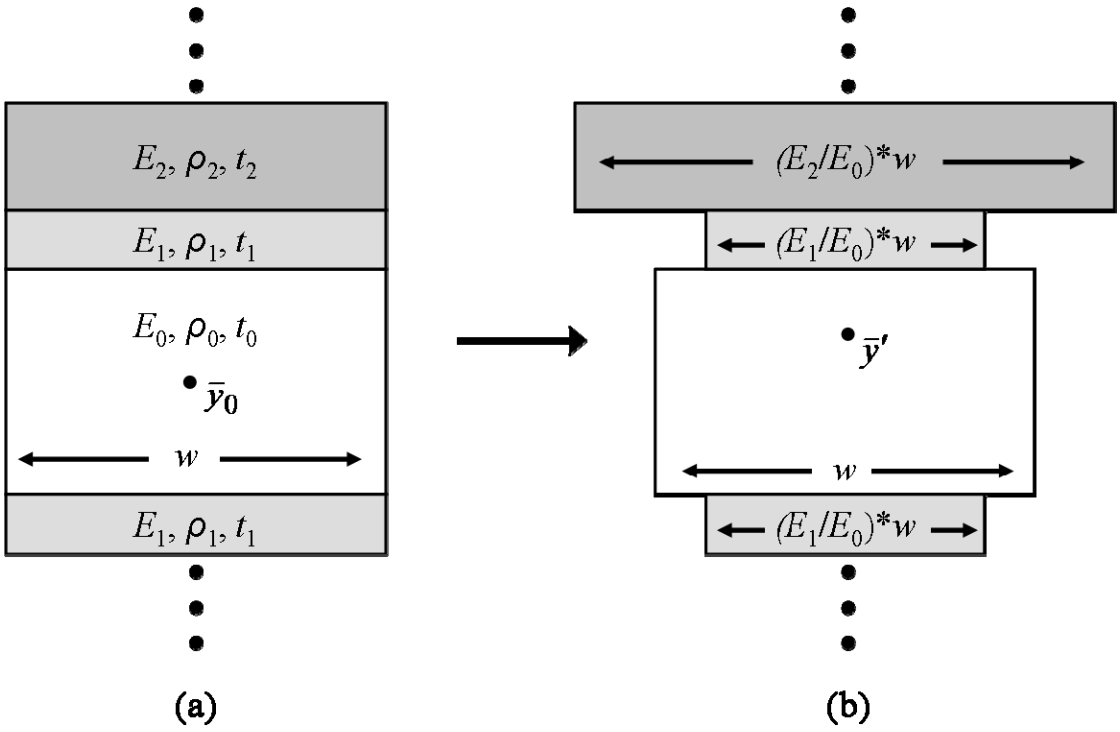

Figure 4-3. (a) Cross-sectional schematic of cantilevers composed of multiple added layers. All layers are assumed to have the same width, w, and $E_2 > E_0 > E_1$. (b) Equivalent beam version of (a) with uniform stiffness, E_0, used to calculate the change in flexural rigidity. $\bar{y}$ designates the centroid of the beam, around which the second moment of the area must be calculated.

It is important to remember that beams bend about their neutral axis, which is defined by the centroid of the cross-section which lies in the plane where there are no stresses or strains along the device length. For a beam with homogeneous density, the centroid is also the center of mass. However, the equivalent beam created above is of heterogeneous density. Therefore, a new centroid, $\bar{y}'$, must be defined around which the new I must be calculated.

To do this, the beam is broken up into *n* different rectangular cross-sections and the new centroid is determined by

$$\bar{y}' = \frac{\sum (A_n \bar{y}_n)}{\sum A_n} \tag{4-16}$$

where $\bar{y}_n$ is the centroid and A_n is the area of each individual cross-sectional area. Once the new centroid is found, then the second moment of the area can be calculated using the parallel axis theorem, which states that

$$I' = \sum (I_n + A_n (\bar{y}_n - \bar{y}')^2) \tag{4-17}$$

Once I' is determined, the new flexural rigidity is given by $E_0 I'$.

4.2.1 Bilateral Detection

In bilateral detection schemes, added material is deposited on all surfaces of the resonator. Examples of such processes include chemical vapor deposition, atomic layer deposition (ALD), or protein adsorption. Because the added material binds to both sides equally, there is actually no change in the centroid from the center of the original cantilever beam. Therefore, the new second moment of the area can be determined using the width of the added material scaled by a factor of $\alpha = E_1/E_0$ as the following:

$$I' = I_0 + 2 * I_1 = \frac{1}{12} w t_0^3 + 2\left(\frac{1}{12} \alpha w t_1^3 + \alpha w t_1 \left(\frac{t_0 + t_1}{2} \right)^2 \right) \tag{4-18}$$

which simplifies to

$$I' = \frac{1}{12} w t_0^3 \left[1 + 2\alpha \left(\frac{t_1}{t_0} \right)^3 + \frac{6\alpha t_1}{t_0^3} \left(t_0^2 + 2 t_0 t_1 + t_1^2 \right) \right] \tag{4-19}$$

This can be further reduced by substituting $\tau = t_1 / t_0$, which results in

$$\begin{aligned} I' &= I_0 \left[1 + 2\alpha\tau^3 + 6\alpha\tau \left(\tau^2 + 2\tau + 1 \right) \right] \\ I' &= I_0 \left[1 + 6\alpha\tau + 12\alpha\tau^2 + 8\alpha\tau^3 \right] \end{aligned} \tag{4-20}$$

The new mass of the trilayer cantilever is also needed for Equation (4-13)

$$m' = w\left(\rho_0 t_0 + 2\rho_1 t_1 \right) \tag{4-21}$$

Combining Equations (4-13), (4-20), and (4-21), the frequency shift for bilateral material deposition becomes the following

$$\frac{\Delta f}{f} = \sqrt{\frac{D'/D}{m'/m}} - 1 = \sqrt{\frac{E_0 I_0 (1 + 6\alpha\tau + 12\alpha\tau^2 + 8\alpha\tau^3) / E_0 I_0}{w(\rho_0 t_0 + 2\rho_1 t_1) / w\rho_0 t_0}} - 1 \tag{4-22}$$

If one more substitution is used for the density ratio, setting $\beta = \rho_1 / \rho_0$, we arrive at the expression

$$\frac{\Delta f}{f} = \sqrt{\frac{1 + 6\alpha\tau + 12\alpha\tau^2 + 8\alpha\tau^3}{1 + 2\beta\tau}} - 1 \tag{4-23}$$

This equation is valid for all added film thicknesses, though it can be simplified if the thickness of added material is very small. In this case, only terms linear in τ are kept, and a Taylor approximation may be applied to reach a form of Equation (4-12) below

$$\frac{\Delta f}{f} = (1+3\alpha\tau)(1-\beta\tau)-1 \approx (3\alpha-\beta)\tau$$

$$\frac{\Delta f}{f} = \left(3\frac{E_1}{E_0} - \frac{\rho_1}{\rho_0}\right)\frac{t_1}{t_0} \tag{4-24}$$

In the limit of high sensitivity detection, the thickness of material added to the sensors will be very small, resulting in low thickness ratios ($t_1 / t_0 << 1$) that make Equation (4-24) an acceptable and useful approximation.

4.2.2 Unilateral Detection

In cases where unilateral deposition or binding of material is necessary, such as evaporated metals or materials binding to such films (*e.g.* thiol-based molecules binding to a gold-coated cantilever), the mechanics of the resonator must be approached differently. Unlike the bilateral case, the uneven deposition of material changes the centroid of the beam, which significantly complicates the formulation of the new beam flexural rigidity. For the unilateral deposition of one material, the new centroid can be calculated from Equation (4-16) to be

$$\bar{y}' = \frac{wt_0 * t_0/2 + \alpha w t_1 * (t_0 + t_1/2)}{wt_0 + \alpha w t_1} = \frac{t_0}{2}\frac{1+\alpha\tau*(2+\tau)}{(1+\alpha\tau)} = \frac{t_0}{2}\frac{1+2\alpha\tau+\alpha\tau^2}{(1+\alpha\tau)} \tag{4-25}$$

using the same substitutions as the bilateral case. Now that the centroid has moved upwards, the parallel axis theorem is needed again but now for both the cantilever and added material in the calculation of the new second moment of the area, shown in the following

$$I' = \frac{wt_0^3}{12} + wt_0\left(\bar{y}' - \frac{t_0}{2}\right)^2 + \frac{\alpha w t_1^3}{12} + \alpha w t_1\left(\bar{y}' - \left(t_0 + \frac{t_1}{2}\right)\right)^2 \tag{4-26}$$

which can be further simplified to

$$I' = I_0\left[1 + \alpha\tau^3 + \frac{12}{t_0^2}\left(\bar{y}' - \frac{t_0}{2}\right)^2 + \frac{12\alpha\tau}{t_0^2}\left(\bar{y}' - \left(t_0 + \frac{t_1}{2}\right)\right)^2\right] \tag{4-27}$$

Inserting Equation (4-25) into the above (4-27) removes the factors of t_0 / 2 and after some simplification results in the following expression

$$I' = I_0\left[1 + \alpha\tau^3 + 3\alpha^2\tau^2\left(\frac{1+\tau}{1+\alpha\tau}\right)^2 + 3\alpha\tau\left(\frac{1+\tau}{1+\alpha\tau}\right)^2\right] \tag{4-28}$$

A term of $(1+\alpha\tau)$ can conveniently be factored from the last two terms, giving an expression for flexural rigidity

$$D' = E_0 I_0\left[1 + \alpha\tau^3 + 3\alpha\tau\left(\frac{1+2\tau+\tau^2}{1+\alpha\tau}\right)\right] \tag{4-29}$$

From here, a new version of Equation (4-22) can be written for unilateral deposition as

$$\frac{\Delta f}{f} = \sqrt{\frac{1+\alpha\tau^3+3\alpha\tau\left(\frac{1+2\tau+\tau^2}{1+\alpha\tau}\right)}{1+\beta\tau}} - 1 \tag{4-30}$$

In applications where the thickness ratio is quite small, Equation (4-30) simplifies to

$$\frac{\Delta f}{f} = \left(1+\frac{3\alpha\tau}{2}\right)\left(1-\frac{\beta\tau}{2}\right) - 1 \approx \tfrac{1}{2}(3\alpha-\beta)\tau$$
$$\frac{\Delta f}{f} = \frac{1}{2}\left(3\frac{E_1}{E_0} - \frac{\rho_1}{\rho_0}\right)\frac{t_1}{t_0} \tag{4-31}$$

Reassuringly, Equations (4-24) and (4-31) are quite similar and only differ by a factor of two since there is twice as much added material in the bilateral case.

Therefore, in the limit of very small thickness ratio of added material, a valid assumption when approaching the detection limit of resonant sensors, a single equation governing frequency shift of cantilevered resonators can be used

$$\frac{\Delta f}{f} = \frac{n}{2}\left(3\frac{E_1}{E_0} - \frac{\rho_1}{\rho_0}\right)\frac{t_1}{t_0} \tag{4-32}$$

where n is a factor of 1 or 2 depending on if the added material deposits on just one or both sides of the device.

4.2.3 Bilateral Growth Using ALD

Atomic layer deposition, or ALD, is a material deposition technique that can deposit extremely thin and highly conformal films (even in very high aspect ratio features) using a cyclical growth process where each cycle deposits a fraction of a monolayer of material on a surface. In addition, many of the materials that can be deposited by ALD are insulator materials, including high-κ dielectrics, that are of great interest in the microelectronics industry, enabling denser and deeper capacitors for memory technologies, as well as improving the gate dielectric and reducing leakage currents in the current-day (45 nm) and future (32 nm) transistor technologies for microprocessors.[25,26] ALD works by limiting typical chemical vapor deposition reactions to one reactant at a time, and precisely controlling the environment so that no more than a monolayer (though most commonly less) of one reactant binds to the surface. The first reactant is then chemically fixed to the surface using water vapor, plasma, or temperature to remove undesired parts of the organic precursor molecule. If necessary for the process, a similar step brings in the second component in a similar way. Repeating this cycle many times can result in highly linear depositions of thin films. A thorough review of this process and the intricacies of its surface chemistries and physical behavior has been presented by Puurunen.[27]

ALD film growth presents a useful platform to demonstrate the validity of bilateral material deposition on cantilever resonators because it results in a highly conformal coating for high aspect ratio features and the growth rate is both linear and slow, allowing great control over the thickness of extremely thin film depositions. Experiments were performed using low stress silicon nitride resonators, fabricated as described in Section 3.1. First, initial resonant frequencies were measured on 2 μm wide cantilevers with lengths of 3, 4, 5, and 6 μm; roughly 50 cantilevers were

measured on each chip (*i.e.* for each deposited thickness). The actual cantilever lengths were ~1.5 μm longer than these patterned lengths because of the undercut produced when releasing devices in hydrofluoric acid. Using these effective lengths with Equation (4-11), the resonant frequencies can be plotted against t/l^2 in order to calculate the specific modulus, E/ρ, for the low stress silicon nitride; this graph is shown in Figure 4-4. The specific modulus was determined to be 33.5 ± 2.61 x 10^6 m^2/s^2. Assuming that the silicon nitride has the bulk density, 3100 kg/m^3, the stiffness of the silicon nitride is then 104 ± 8 GPa.

After measuring a baseline resonant frequency, devices were placed in an Oxford Instruments FlexAL ALD tool for growth of various thicknesses of silicon dioxide: 0.5, 2.4, 4.5, 6.9, 8.9, 14.6, 19.5, and 25 nm. The SiO_2 was deposited using a plasma-based process with a bis(tertiary-butylamino)silane, or BTBAS, precursor molecule at 110° C. Film growth was characterized as a function of cycle number on low stress silicon nitride using witness chips having the identical film as was used for the resonators.

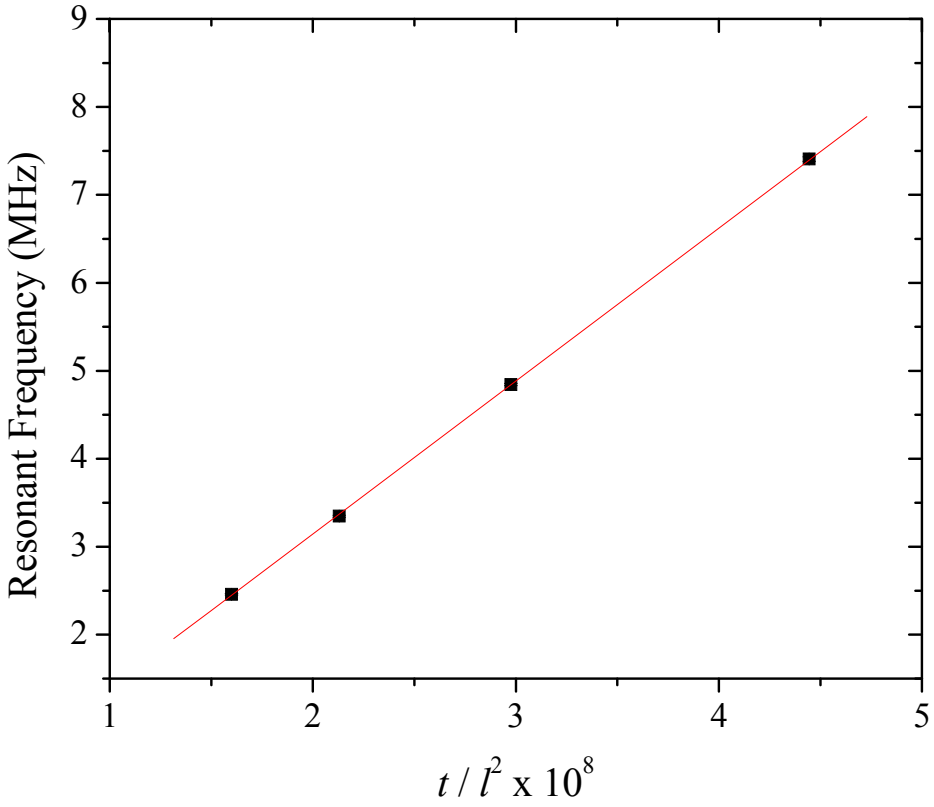

Figure 4-4. Graph of resonant frequency vs. thickness over length squared for several cantilever lengths, which was used to determine the mechanical properties of low stress silicon nitride.

Film thickness was measured using a Woollam spectroscopic ellipsometer and is shown in Figure 4-5 as a function of ALD cycles used. The observed growth was quite linear, with a rate of 1.64 ± 0.03 Å per cycle. In addition, a lag of roughly 5 cycles was needed before the film began significant growth, possibly allowing for sufficiently surface nucleation to support the full growth rate. A process with only four cycles was also tested, however there was no detectable deposition of silicon dioxide.

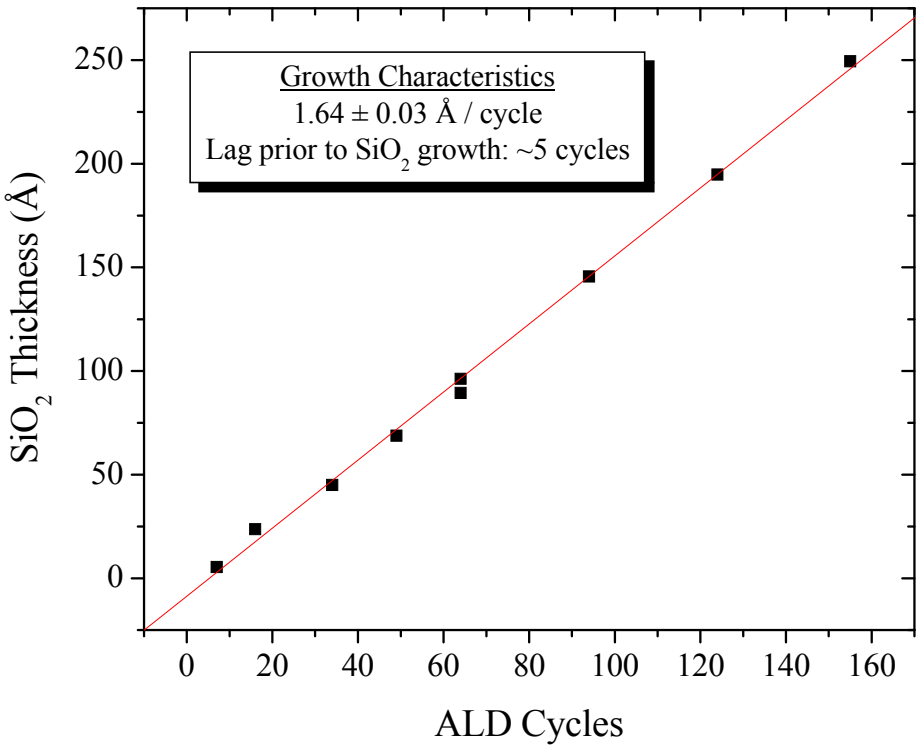

Figure 4-5. Plot of silicon dioxide film thickness grown on low stress silicon nitride using ALD. The growth per cycle was fairly constant at ~1.64 Å per cycle.

Device resonant frequencies were then measured again after ALD deposition and frequency shifts determined. Equation (4-23) shows that if these frequency shifts are plotted as a function of thickness ratio, τ, then the stiffness and density ratios can be determined from fitting this equation to the data. This has been done in Figure 4-6 for all cantilever lengths. It is evident that all cantilever lengths behave the same way in frequency, also agreeing with Equation (4-23).

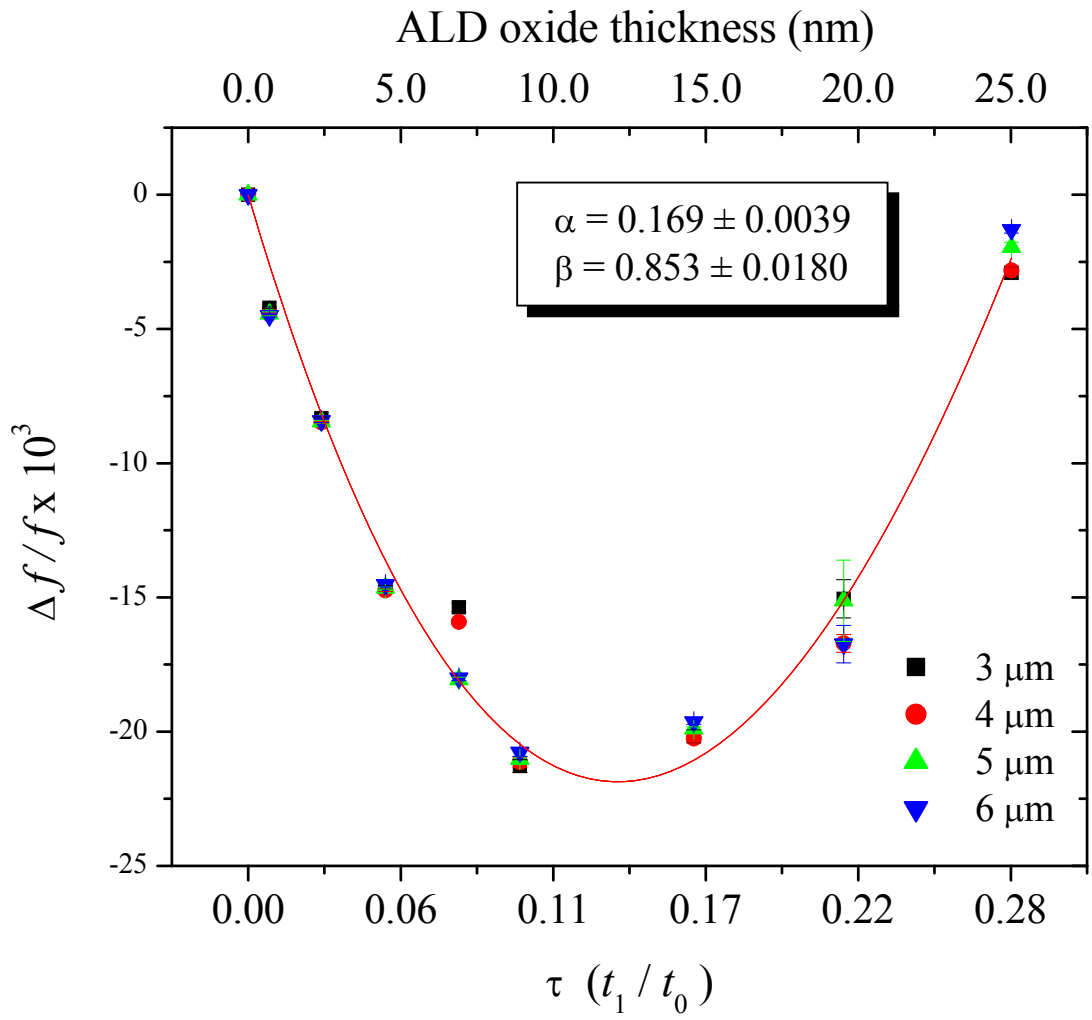

Figure 4-6. Resonant frequency shift plotted as a function of the thickness ratio of ALD deposited silicon dioxide. The consistent behavior despite varying cantilever length validates assumptions that change in cantilever length upon uniform deposition is negligible.

The fit parameters, when applied to the stiffness and density of silicon nitride discussed above, result in a silicon dioxide stiffness and density of 17.5 ± 1.8 GPa and 2650 ± 60 kg/m^3, respectively. The density agrees much better with that of quartz (2650 kg/m^3) rather than SiO_2 growth thermally from silicon (2200 kg/m^3). This can be accounted for by considering the bottom-up growth of ALD SiO_2 that has no geometric constraints, whereas thermally grown silicon dioxide is grown *via* oxygen diffusion into crystalline silicon, which restricts the final density of the material. In addition, because ALD growth on an amorphous silicon nitride film likely to be amorphous as well, the stiffness should be significantly less than quartz (100 GPa) or thermally grown silicon dioxide (~70 GPa).

Device quality factors were also measured along with resonant frequency. Prior to the silicon dioxide deposition, quality factors ranged from roughly 6000 to 7500, but quickly fell off as more silicon dioxide was deposited. Figure 4-7 shows this sharp falloff of *Q* with silicon dioxide thickness for 2x5 μm resonators. It is somewhat surprising that even 5 Å of silicon dioxide drops the quality factor to less than half of its initial value. However, if the ALD loop process is considered, an oxygen plasma is used each cycle to remove the side chains from the silicon in BTBAS and oxidize it, inevitably oxidizing the resonator surface as well. This oxidation agrees with observations of oxidized single crystal silicon resonators discussed earlier in Section 4.1.2.[11-14]

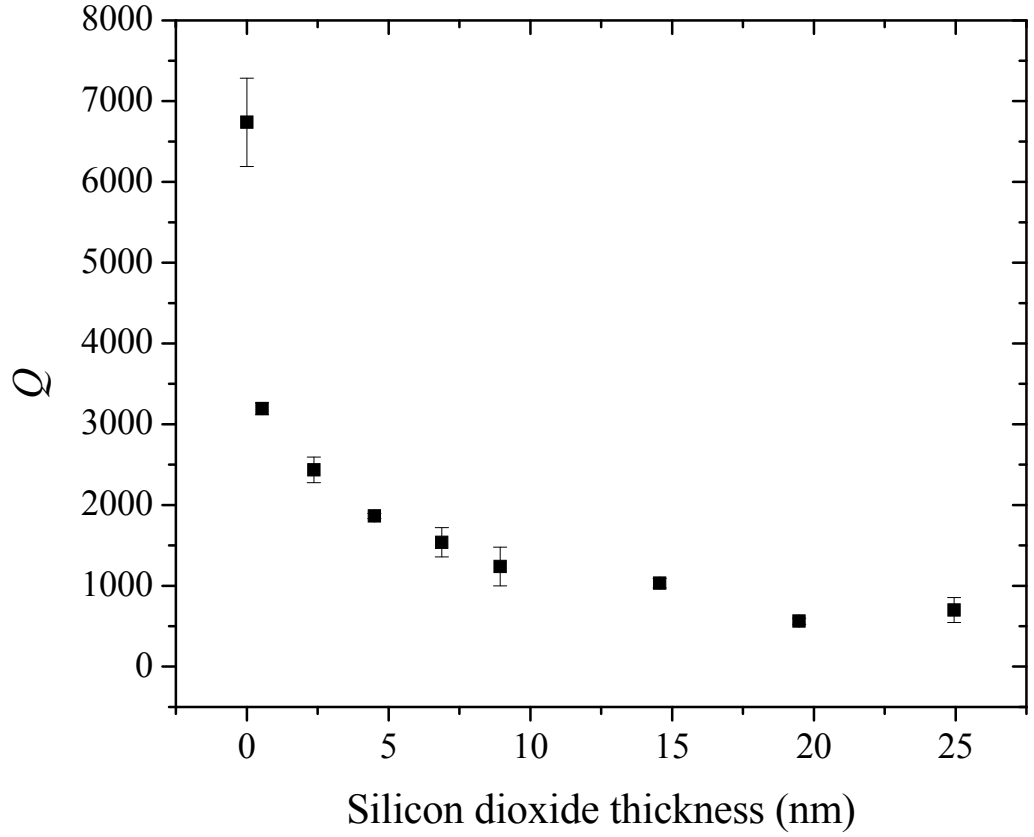

Figure 4-7. Plot of quality factor as a function of added oxide thickness for 2 x 5 μm cantilever resonators.

4.3 Effect of Device Geometry[1]

Despite the fact that cantilevers represent the most common geometry used in the literature, resonant MEMS and NEMS can take on many different geometries unlike deflection-based MEMS cantilever sensors. In this discussion, geometry refers primarily to variations in the top-down view of devices, as fabrication of many resonators on a wafer results in devices that have roughly the same thickness and feature the same materials properties. The key question that arises is "Are other geometries more or less sensitive than cantilevers, and if so, why and in what

regimes?" In light of the above discussions, the effects of mass and flexural rigidity must to be investigated as a function of resonator geometry as well as how the material is deposited.

Equation (4-32) demonstrates that frequency shifts resulting from uniform deposition on cantilevers are independent of device width and length, as long as they have the same density, stiffness, and thickness. This should still hold for doubly clamped beams or cantilevers with variable cross sections, such as cantilevered paddles. As more complex geometries are studied with interesting cross-sections, the flexural rigidity term will likely become a factor differentiating the sensitivity of different geometries. However, for films with negligibly small α (low stiffness), the remaining mass addition term has no dependence on device geometry. The most intriguing part of the question just proposed, however, is the how different device geometries sense non-uniform, localized addition(s) of material, which will be discussed in the following.

Intuitively, if a point mass were placed at the very base of a vibrating cantilever, it is not likely to know the difference, whereas if it were placed at the tip, the mass would have the greatest possible effect on resonant frequency. Then, the sensitivity to mass must vary along the length of the device which has been demonstrated for a microcantilever.[28] This has been used in some resonance-based mechanical sensors in order to detect individually bound analytes by limiting their binding to occur near the cantilever tip.[29-31] In addition, it has been demonstrated that there are conditions for which the stiffness of bound material becomes important near the clamped end of a cantilever.[32]

For more complex geometries, the frequency response as a function of binding location is more complicated. It has been shown that the resonant frequencies of beams with discontinuous cross sections such as cantilevered paddles can be

determined using an adapted form of the Rayleigh quotient method, an approach based on the conservation of energy.[33] It is demonstrated that there is negligible error when approximating the bending mode shape of such a complex beam as having the same bending mode shape as a cantilever with the same length. Using this method, the resonant frequency, ω, for bending modes can then be described by

$$\omega^2 = \frac{k_e}{m_e} = \frac{\int_0^l D(x)[\bar{u}''(x)]^2 dx}{\int_0^l \lambda(x)[\bar{u}(x)]^2 dx} \tag{4-33}$$

where k_e and m_e are the effective spring constant and mass of the resonator, $\bar{u}(x)$ is the normalized displacement distribution function that describes the resonant mode shape, and $\lambda(x)$ is the mass per unit length of the cantilever, given by the product of density and cross-sectional area. Note that $D(x)$ and $\lambda(x)$ could be stepwise functions that vary along the length of the cantilever due to discontinuous resonator shape or the addition of another material at specific locations along the resonator.

Inspection of Equation (4-33) reveals that the positional sensitivity is closely related to the resonant mode shape and permits qualitative study of complex device resonances. For instance, by only knowing the boundary conditions associated with resonance of cantilevered beams, namely $u(x=0)=0$ and $u''(x=l)=0$, one knows that mass addition at the clamping point and flexural rigidity changes at the free end of the cantilever will have no effect on the resonant frequency. Furthermore, changes in the effective mass will be largest when material is added at points where the amplitude of resonance, $u(x)$, is largest. On the other hand, changes in the flexural rigidity will be maximized where the device curvature is highest.

In order to further illustrate the effect of resonant sensor geometry on the detection of locally bound material, we have modeled the resonant response of a range of structures and fabricated micromechanical resonators of different sizes and geometries and deposited gold pads at many locations across the devices. By knowing the resonant frequencies before and after etching away the gold, the frequency responses of different device geometries to localized deposition (or removal) of material can be studied. Three different device geometries were tested and will be described in detail below. In addition, experimental results were compared with finite element analysis simulations. An analytical model is presented in order to study how each of the relevant materials properties affect the positional dependence of the frequency response of a resonator to added material. The implications of these results on sensing applications and appropriate devices designs will also be discussed.

4.3.1 Experimental Methods for Studying Localized Binding

Resonators in these experiments were fabricated for the most part as described in Section 3.1, however, the silicon dioxide and low stress nitride film thicknesses used were 1.5 μm and 150 nm. In addition, a second layer of lithography was performed in order to define the position of the gold pads for a subsequent liftoff process. Alignment was performed using an automated stepper tool with errors of < 300 nm. A 1 nm layer of chromium was evaporated as an adhesion layer for approximately 25 nm of gold deposited by e-beam evaporation. The circular gold pads were the same size on all devices, with radii of ~0.5 μm. After liftoff, the wafer was diced into chips and prepared as usual. The undercuts produced at the clamping points of all devices during the release etch in hydrofluoric acid were measured to be

~1.75 μm using optical microscopy, which was possible since the 90 nm thin resonators were sufficiently transparent in order to observe the silicon dioxide pillars beneath the device anchors.

Arrays ranging from 9 to 30 resonators were fabricated within 150 × 150 μm^2 areas and repeated many times across each die. The high density of devices permitted placement of gold pads at many positions of interest across arrays of devices. An image of such an array was taken using a scanning electron microscope (SEM) and is shown in Figure 4-8. Multiple arrays of each device geometry were present, allowing repeated measurements to be made, improving confidence in the experimental results. Typically, three arrays were used to calculate resonant frequency responses; the standard deviations of these readings were used for error bars in all figures.

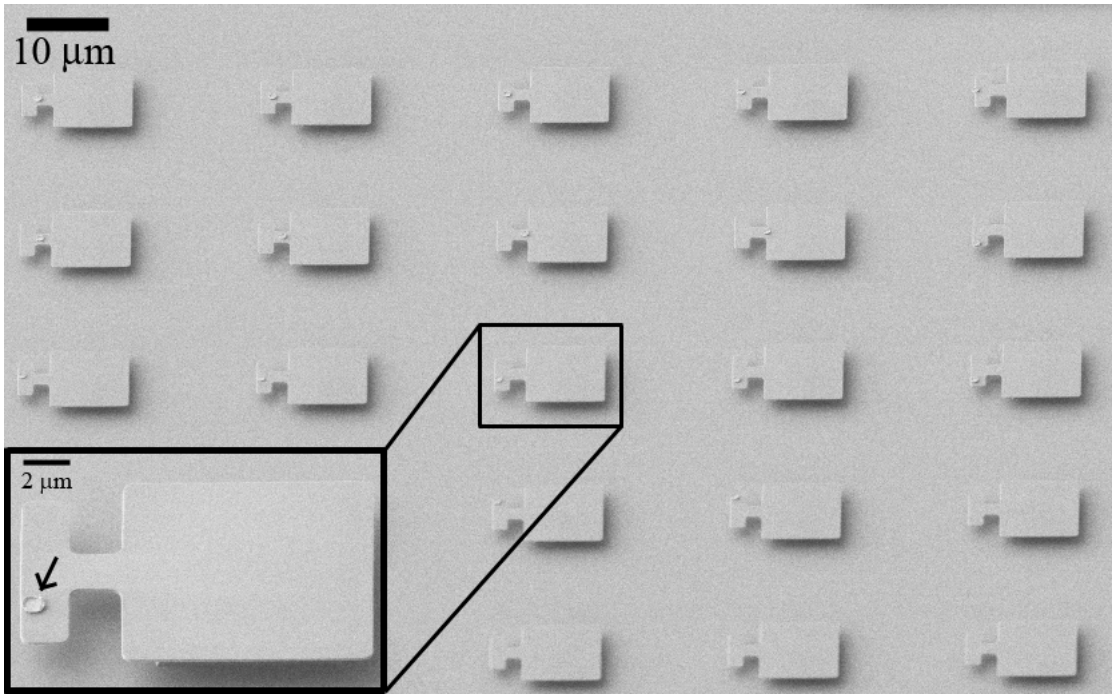

Figure 4-8. SEM image of an array of paddlever resonators with gold pads positioned at several different locations across the devices within a single array.

Three different device geometries were studied and are shown in Figure 4-9. SEM images of devices are shown with simple schematics defining relevant dimensions. The first and simplest device geometry studied was a rectangular cantilever. Cantilevers measuring 2 μm in width were made with lengths varying from 5 to 8 μm. Gold pads were deposited from the tip to the clamped end at 500 nm increments.

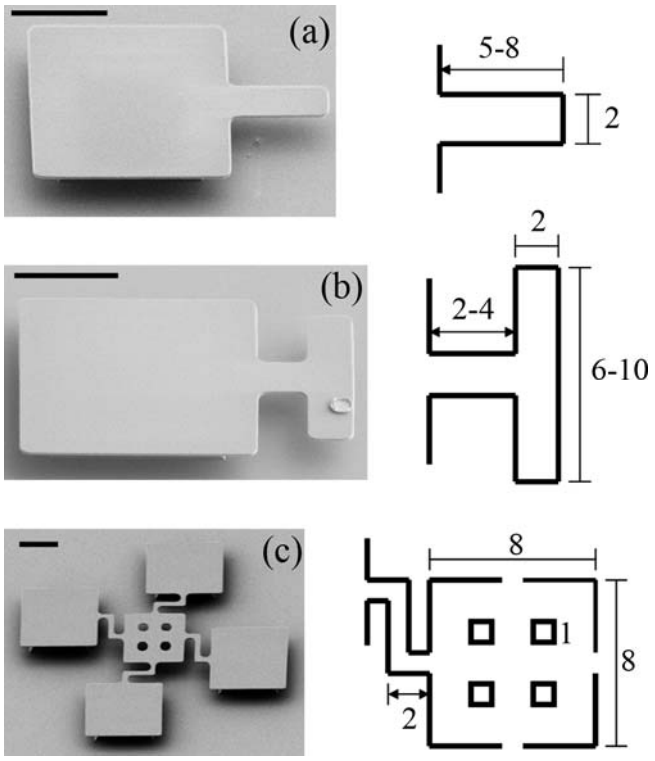

Figure 4-9. SEM images and dimensional schematics of each of the device geometries studied here, including (a) cantilevers, (b) paddlevers, and (c) trampolines. All dimensions are in micrometers, and all scale bars represent 5 μm.

The next devices studied are cantilevers with a 2 μm long paddle at the end, also called paddlevers; shown in Figure 4-9(b). Because the tip of a cantilever is sensitive to bound mass, these paddlevers were designed in order to increase the area

for binding in this region and in turn its mass sensitivity. Devices measuring 4-6 μm in length were made with paddle widths varying from 6 to 10 μm. In order to study the frequency response of bound material to the paddle, gold pads were placed at locations across the paddle as well as along the length of the device.

The third device studied in this work is a trampoline-like structure with an 8 × 8 μm^2 paddle suspended by four flexible support arms. An SEM image and schematic of trampoline dimensions are shown in Figure 4-9(c). The design for this device aimed to create a resonator in which much of the device moves in phase with the same amplitude. The holes are present in order to allow hydrofluoric acid to undercut the large paddles.

Following frequency measurements with gold pads present, the chips were placed in an iodine-based chemical etchant to remove the gold pads. After rinsing and drying, the chips were placed back into vacuum, and device frequencies measured again. Plain resonators of each size and geometry with no gold were also present in each array as a control for the effect of gold etchant on silicon nitride as well as slight environmental variations between measurements. These shifts were small, such that magnitudes of $\Delta f/f$ were on the order of 10^{-4} or 10^{-5}. Control frequency shifts were subtracted from the shifts of other devices in that array to permit correlation of frequency shift signals to the removal of gold. All frequency shifts are discussed and plotted with respect to the addition of gold, such that measurements after the gold etch are considered as the initial resonant frequency. This convention is more easily interpreted from a sensing perspective where a change in k increases and addition of mass decreases the resonant frequency.

Experimental results were compared with finite element simulations for addition of material to all three geometries studied in this section. Device overhangs created during the sacrificial silicon dioxide etch were included in the modeling.

Resonant frequencies for different devices and modes agreed with experimental observations (≤ 2% difference) when the specific modulus, E / ρ was reduced to 70% of the bulk value. Finite element studies were performed both with and without flexural rigidity of the gold pads ($E_1 = 0$) in order to observe its effect on the frequency responses. The mass and stiffness of the deposited gold were determined by fitting the simulations to experimental data, giving $E_{Au} \approx 40$ GPa and $m \approx 400$ fg. The stiffness of evaporated gold thin films has previously been measured and ranges from 30-50 GPa.[34] Using the accepted density of gold, 19.3 g/cm^3, with the average gold dot radius, this mass corresponded to a gold thickness of ~ 28 nm, which is in reasonable agreement with the value measured during gold deposition.

4.3.2 Cantilevers

Cantilevers with lengths of 5, 6, 7, and 8 μm were fabricated with gold dots placed along their length, and resonant frequencies were measured before and after etching away the gold. Frequency responses as a function of gold dot position along the cantilever are shown in Figure 4-10(a). As expected, the cantilever tips are most sensitive to bound material, and larger cantilevers are less sensitive due to higher effective masses. If the data in Figure 4-10(a) is normalized to the maximum frequency shift for each length, the curves collapse onto one another, as shown in Figure 4-10(b), demonstrating the similarity of the resonant modes. Another interesting feature of this data is that the frequency responses of the cantilevers become positive near the clamped end, where the added flexural rigidity of the gold is affecting the resonance.

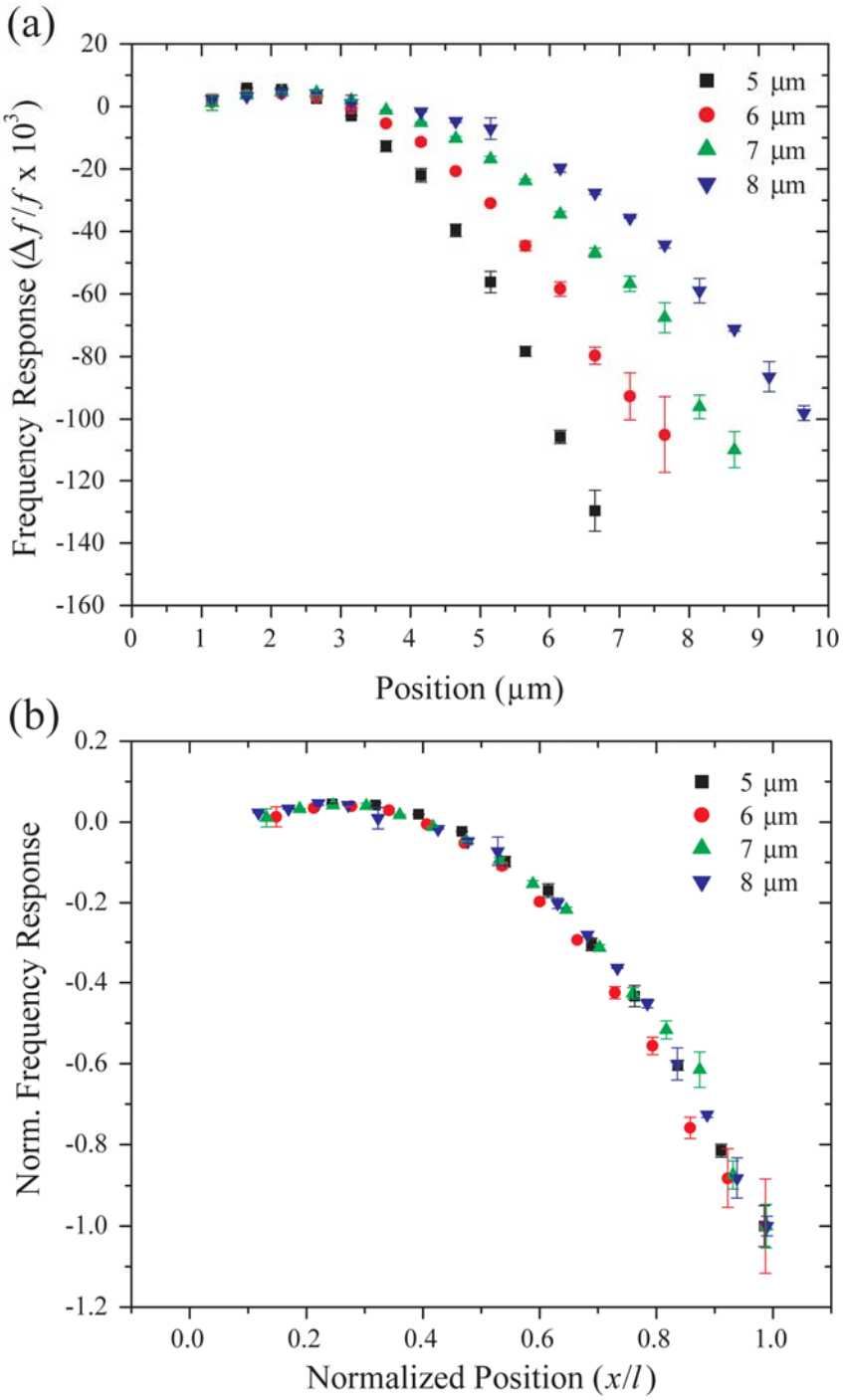

Figure 4-10. (a) Frequency response to the presence of gold pads for 2 µm wide cantilevers with lengths varying from 5 to 8 µm. (b) Normalized version of (a) in which all the responses of all cantilevers collapse onto roughly the same curve as a result of similar mode shape.

Finite element simulations were performed for addition of point masses at different positions along the width and length of a 2 μm wide and 5 μm long cantilever. Cantilever support overhangs created experimentally during the hydrofluoric acid etch are also included in the modeled structure. Simulated frequency shifts for the fundamental resonant mode are plotted as a three-dimensional surface contour in Figure 4-11(a) as a function of position. Each vertex of the surface represents data from a single simulation, where the z-axis represents the frequency response. It is apparent that the positional frequency response is very much related to the shape of the cantilever resonance. The data points present in Figure 4-11(a) are experimental frequency shifts for the 5 μm long cantilevers, which appear to follow along with the simulations except for near the clamped end of the device.

To further compare experiment and simulation, the frequency response along the cantilever center (y=0) is plotted as a function of position in Figure 4-11(b). While the simulations using only the mass of the bound material agree well with experiment at the cantilever tip, they deviate near the clamped end. The finite element simulations were repeated including the stiffness of the gold dots in addition to their mass, shown by the dashed line in Figure 4-11(b). This curve agrees with the data along the entire length of the cantilever with an average difference of $-4.9 \pm 5.6\%$, showing that the discrepancy near the clamped end of resonators is in fact due to the flexural rigidity of the gold.

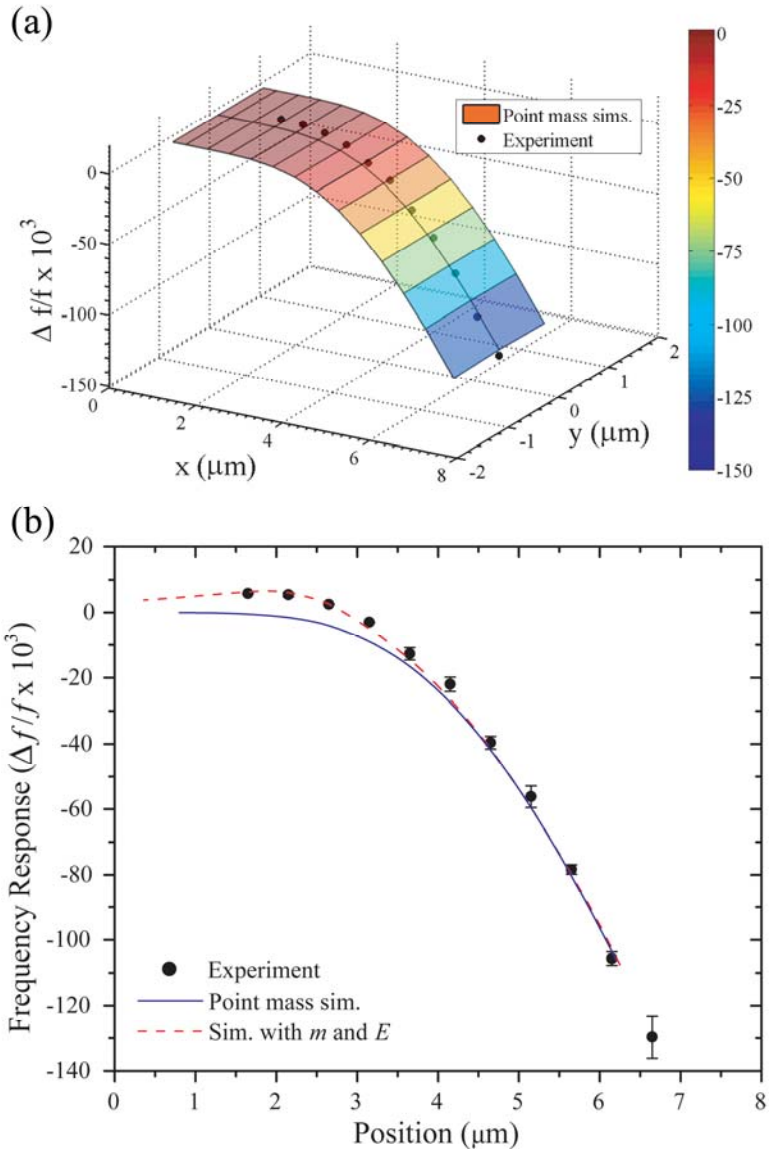

Figure 4-11. (a) Positional frequency response determined from finite element analysis simulations for the effect of a point mass binding to a 2 x 5 μm^2 cantilever. Experimental results for gold addition along a 5 μm long cantilever are represented by the data points. (b) Experimental and simulated (mass only or stiffness and mass) frequency responses as a function of gold pad position along a cantilever. The results indicate that changes in flexural rigidity are important near the clamped end and are needed to account for the difference between point-mass simulations and the experimental results.

The quality factors, Q, of these cantilevers were also measured along with resonant frequency, and some dependence of Q on the location of the gold pad was observed. Control devices with no gold present typically had quality factors of approximately 7000. Quality factors from all cantilever lengths are shown in Figure 4-12 as a function of gold pad position along the cantilever (normalized to cantilever length). At the cantilever tip, Q is unaffected by presence of the gold, while as the gold moves towards the clamped end Q decreases. This is expected, as it has been observed that gold films are lossy and decrease Q for gold-coated cantilevers.[15,16] As the gold pads move onto the overhang region, Q recovers slightly, as it should once the gold moves off of the resonator. These results demonstrate that Q decreases as a result of the additional energy required to bend the added, more lossy material along with the resonator.

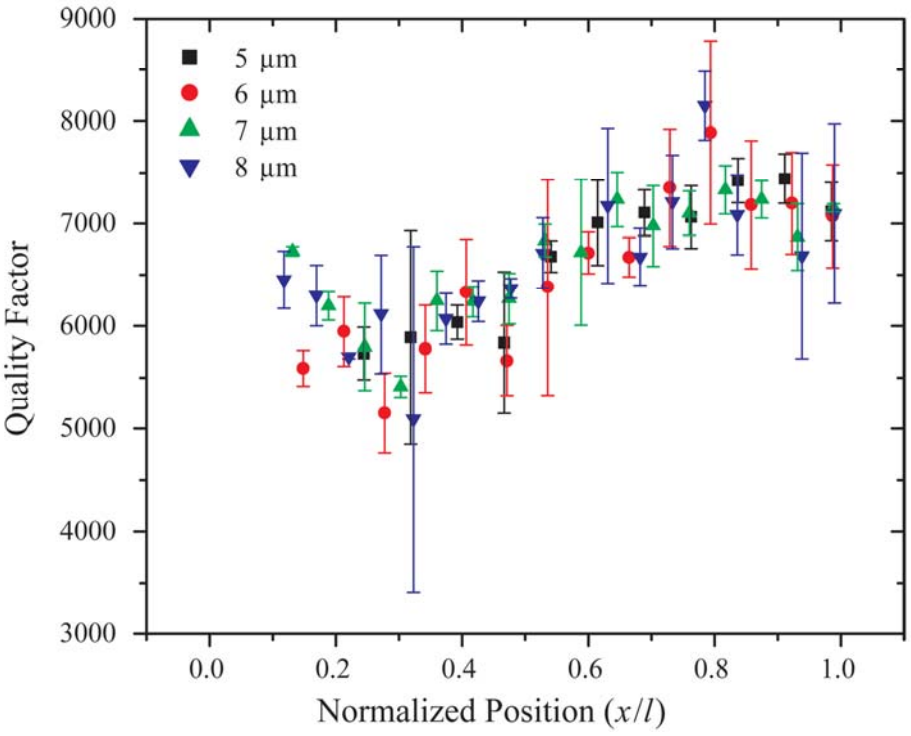

Figure 4-12. Quality factor as a function of gold pad position on cantilevers.

4.3.3 Paddlevers

The next resonator geometry studied was the paddlever geometry. Gold pads were present on these devices along both the length of the device and the width of the paddle. The frequency responses as a function of gold pad position along the 4, 5, and 6 μm long paddlevers are shown in Figure 4-13(a-c). They closely resemble the response curves of the cantilevers; however, the frequency shifts are smaller as a result of larger device mass due to the addition of the paddle. The effect of the paddle can be seen for each device length in that sensitivity to the same amount of added gold decreases as the paddle becomes wider. Along this direction, the paddle only adds effective mass and reduces the mass sensitivity. Again, positive frequency shifts are observed near the base of the paddlevers, occurring as a result of changes in flexural rigidity. In addition, the quality factors decrease as the gold pads are positioned closer to the clamped end of the paddlevers, just as was observed in cantilevers (data not shown).

Gold dots were also placed along the width of the paddle to measure the frequency responses across it. These results are shown in Figure 4-14(a-c) for 4, 5, and 6 μm long devices, respectively. Frequency responses across the paddles were found to be greater than or equal to the response in the center for all paddlever sizes, as expected.

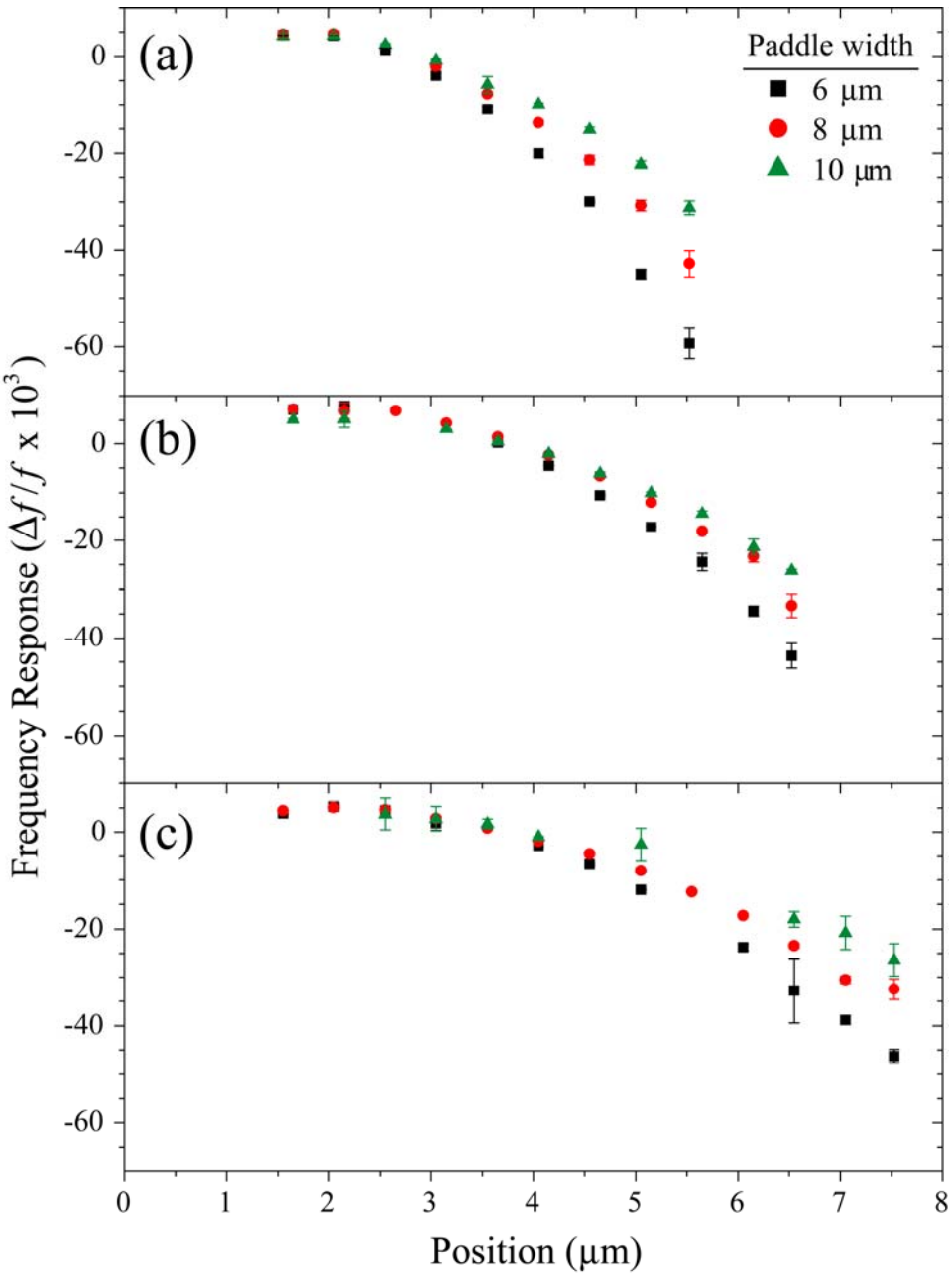

Figure 4-13. Frequency response data from paddlevers measuring (a) 4, (b) 5, and (c) 6 µm in length. For each length the paddle width is varied between 6, 8, and 10 µm, which only changes the effective mass of the resonator in this case where the gold pads are placed along the device length.

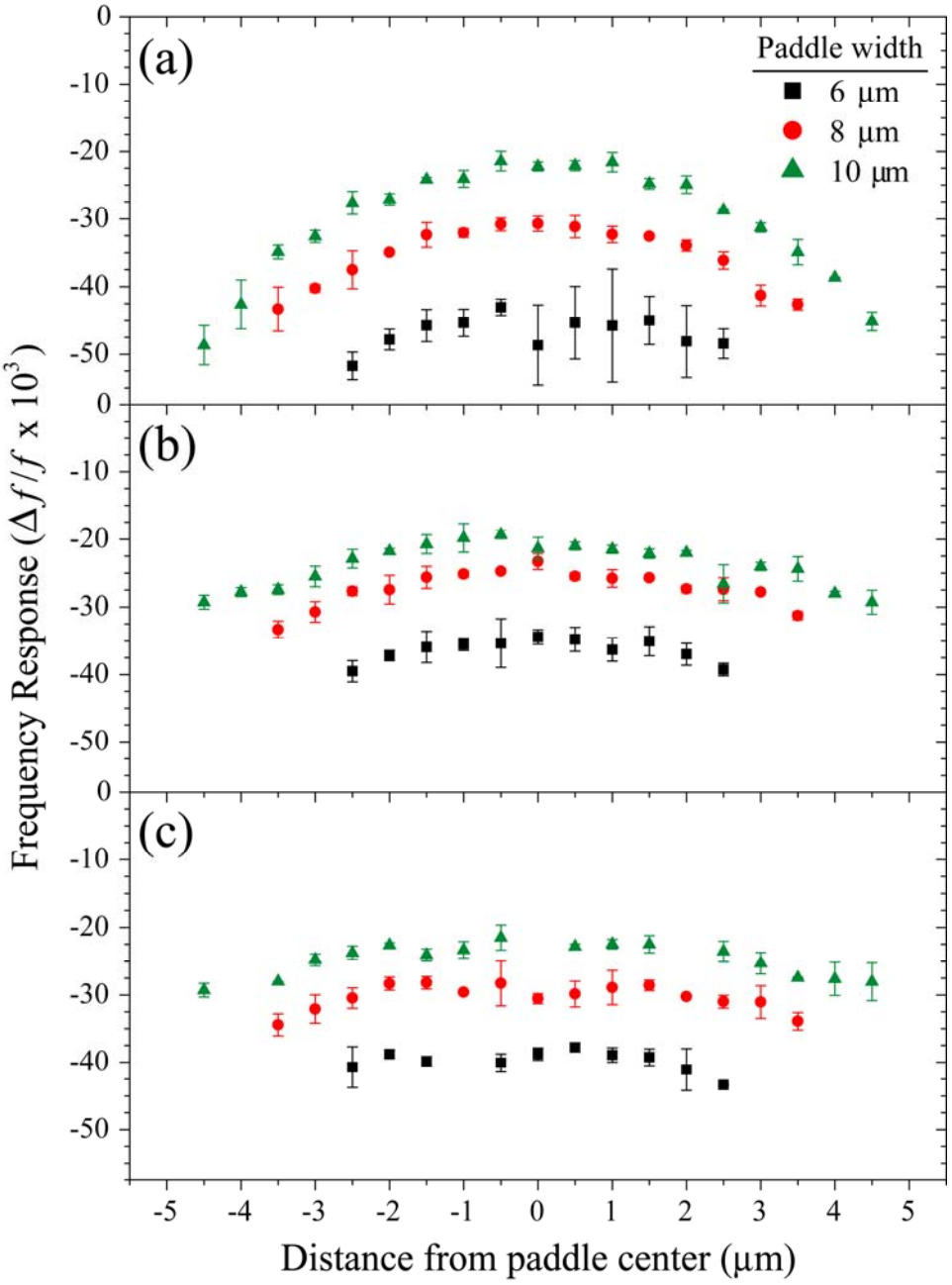

Figure 4-14. Paddlever frequency responses for gold pad placement across the width of paddles for (a) 4, (b) 5, and (c) 6 µm long devices. The changing curvature with device length shows that additional bending of the paddle is taking place during resonance in shorter devices, since mass sensing is proportional to the relative amplitude of vibration.

An interesting feature of Figure 4-14 is that as devices become longer, the frequency shifts from gold dots at the paddle edge approach those of the center. This suggests that in shorter devices the paddle flexes more and undergoes a wing flapping-like motion. This curvature in the frequency response is prominent in Figure 4-14(a) with the 4 μm long paddlevers, while in Figure 4-14(c), the 6 μm long devices show roughly the same response across the paddle, suggesting that the entire paddle moves with the same amplitude. As a result, short paddlevers like those studied here do not permit assumption of cantilever-like mode shapes as suggested,[33] and therefore Equation (4-33) would need to be further complicated in order to account for variation of mode shape along the width of the paddle.

Finite element analysis was also used to model the 5 μm long paddlever with a 10 μm wide paddle. Initially, point-mass simulations were performed identically to those for the cantilever, shown in Figure 4-11(a). Paddlever simulations and experimental data are plotted similarly in Figure 4-15(a) and roughly agree. Two dimensional plots along the length and width of the paddlever are shown in Figure 4-15(b) and (c), respectively. A difference between point-mass simulations and experimental data is once again present when the added material is near the clamped end of the device, as shown in Figure 4-15(b). Including the stiffness of the gold pad in the simulations removes this discrepancy and improves agreement with the experimental data, giving an average difference of 3.2 ± 11%. Along the paddle width, shown in Figure 4-15(c), curvature of the frequency response is apparent, with the ends of the paddle showing highest sensitivity to bound mass. In addition, there was not a significant difference between simulations with and without stiffness. The simulations were on average only 0.3 ± 5.0% different from the experimental values. This further supports our observations that material stiffness is not a significant factor near the free end of a cantilevered resonator.

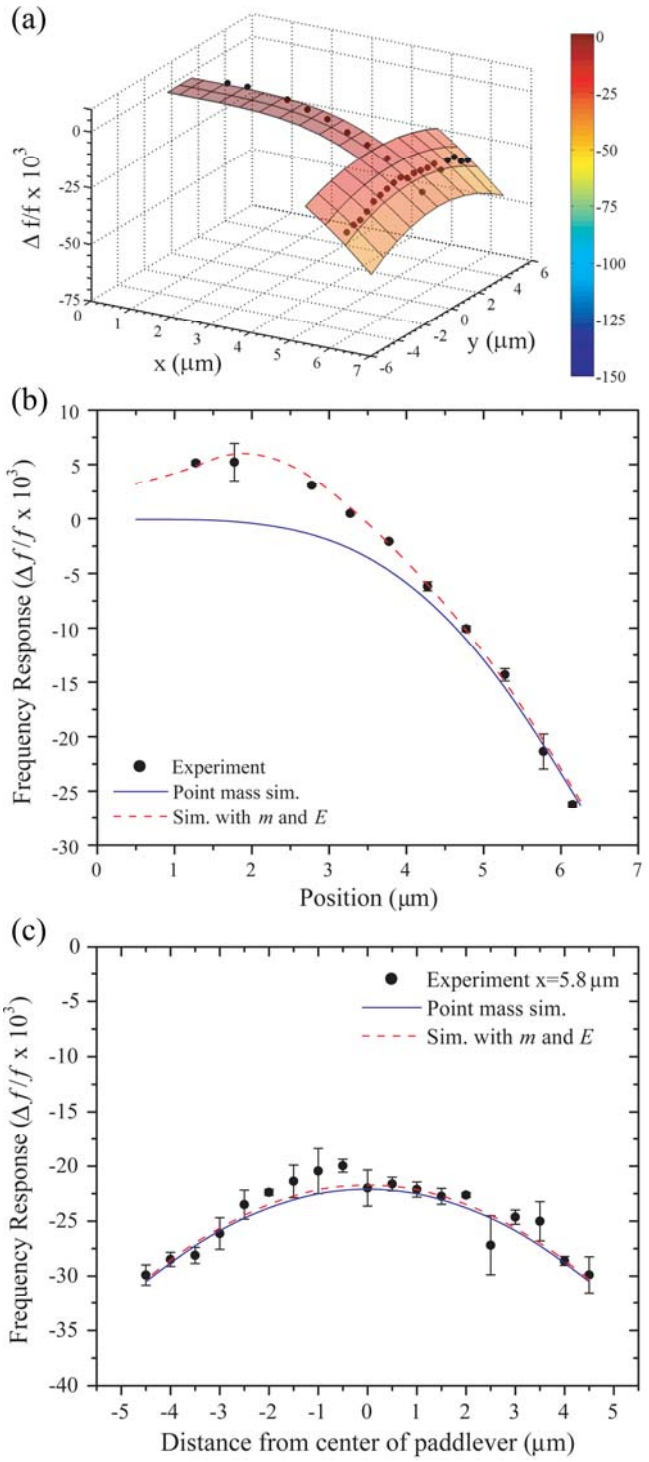

Figure 4-15. (a) Simulated and experimental frequency response of a 5 μm long paddlever with a 10 μm wide paddle as a function of binding location. These results are also shown (b) along the device length and (c) across the width of the paddle.

4.3.4 Trampolines

The final device geometry studied was the trampoline, consisting of a large paddle, suspended by four flexible support arms. Frequency responses were measured with gold dots at several locations on the trampolines, and the devices were also studied using finite element analysis. The experimental results and simulations (mass only) for these trampolines agree well, with an average difference of -2.5 ± 5.7%, and are shown in Figure 4-16(a). An interesting feature of this figure is that the frequency response at positions all across the trampoline is relatively uniform. This agrees with the fundamental resonant mode shape predicted by finite element analysis, a membrane-like mode where the center paddle moves in and out of plane with nearly the same amplitude. The mass of these trampolines is much greater than the cantilevers and paddlevers made in this work, and as a result the frequency responses to the same gold dots are an order of magnitude lower on the trampolines.

Finite element simulations were also performed taking stiffness into account for gold dots placed along the x-axis of the trampoline and compared to experimental data. These results, shown in Figure 4-16(b), reveal that the experimental data agrees with point-mass simulations and that material stiffness does not affect the resonant frequency when binding occurs on the trampoline paddle. However, small positive frequency shifts were observed in both experiment and finite element simulation at points along the support arms, analogous to stiffness effects observed in cantilever and paddlever devices.

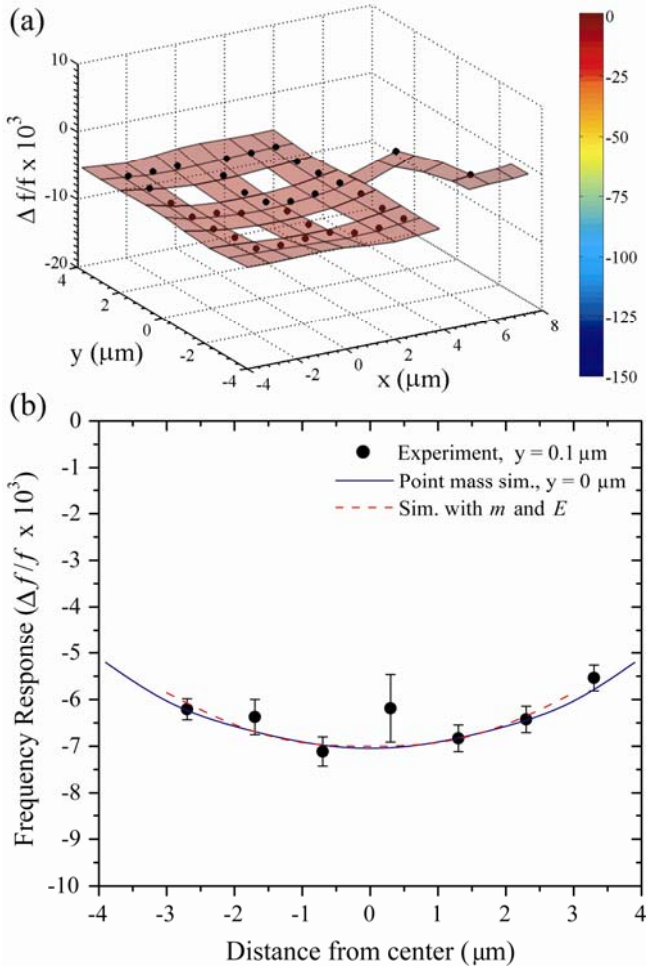

Figure 4-16. (a) Experimental data and finite element simulations (mass only) shown as a function of position across 8 × 8 μm^2 trampolines, demonstrating a fairly uniform response across the device. (b) Subset of the data taken along the x-axis compared with finite element simulations with and without the effect of stiffness. Trampolines demonstrate relatively uniform frequency shifts for binding in the center.

4.3.5 Implications of Materials and Fabrication Methods

In these experiments, the mass rather than the stiffness of the added gold has dominated the frequency responses, as the amplitudes of positive frequency shifts associated with flexural rigidity were typically much lower than those associated with mass. This is not surprising, since the density of gold is over six times larger than silicon nitride while it is roughly a factor of three less stiff. However, flexural rigidity may take over at large gold thicknesses since it depends on a higher power of thickness than added mass does. These conditions could change for different material systems, whether there are different added or resonator materials, or different sizes of each. Many different variables and material parameters become apparent and have a variety of effects on resonant sensing. In the following we study these variables separately in order to learn more about their role in determining frequency responses.

For sensing applications where high sensitivity is required, the materials being detected are typically soft and lightweight (low E and ρ), unlike gold, as well as relatively thin. In order to study the effect of stiffness on frequency responses in this regime, further finite element modeling was performed. Four different configurations on a 5 μm cantilever with overhang were considered: a 5 nm thick localized pad near the cantilever base (x = 1.75 μm) and tip (x = 6.25 μm) in addition to a 5 nm and 10 nm thick, uniform film, all with the same low density of 1 g/cm^3. The base position was chosen since the largest positive frequency shifts experimentally observed were found when the gold was placed at this location, as shown in Figures 4-11(b) and 4-15(b). Frequency shifts are shown in Figure 4-17 as a function of the stiffness ratio (E_1/E_0). As expected, when material binds at the cantilever tip, the frequency shift is negative and the material stiffness has no effect over 8 orders of magnitude. If the bound material is located near the clamped end, the frequency shift is effectively zero

for stiffness ratios less than about 0.01. Above this point, the frequency shift becomes positive and increases quickly with stiffness ratio. If binding occurs uniformly across the device with the same thickness of 5 nm, more mass is added, resulting in greater negative frequency shifts that decrease only slightly (< 5%) up to a stiffness ratio of ~0.01. For higher stiffness ratios, the frequency shift changes significantly and becomes positive around 0.1. The 10 nm film causes larger amplitudes of both positive and negative frequency shifts and leads to a stronger dependence of the frequency response on stiffness ratio.

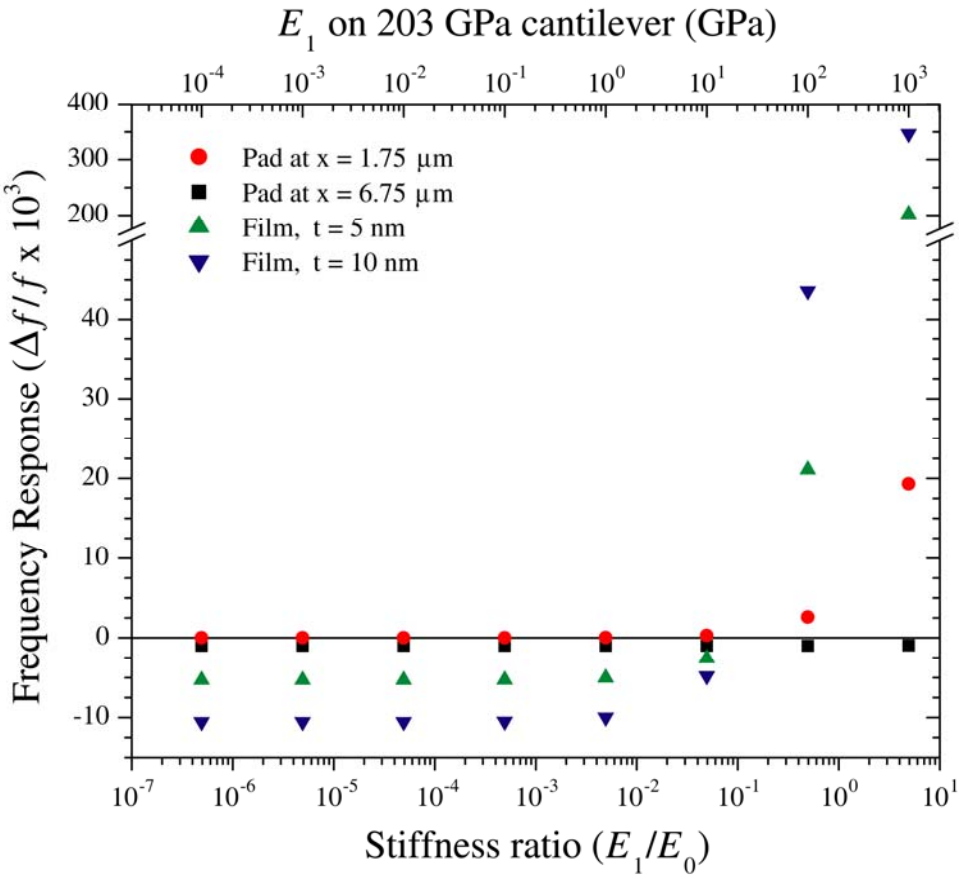

Figure 4-17. Finite element simulation results for cantilever frequency shifts as a function of the added material stiffness in four different configurations.

To learn more about the competing effects of changes in flexural rigidity and mass in the high sensitivity regime, the frequency response profile of a 5 μm cantilever to a 1 x 1 μm^2 square pad of added material is modeled analytically using Equation (4-33). The modeled cantilever is the same as those made in this work, including the 1.75 μm overhang. The change in flexural rigidity for unilaterally deposited material can be derived from Equation (4-29) to be

$$\Delta D = D' - D_0 = D_0\left[\alpha\tau^3 + 3\alpha\tau\left(\frac{1+2\tau+\tau^2}{1+\alpha\tau}\right)\right] \tag{4-34}$$

However, one exception must now be made, because rather than a uniform layer, now only a small pad is present which has a width less than that of the resonator. In order to account for this term, α becomes a function of position, x, along the length such that

$$\alpha(x) = \frac{E_1 w_1(x)}{E_0 w_0(x)} \tag{4-35}$$

Where $w_1(x)$ is now defined as

$$w_1(x) = \begin{cases} 1, & (c-0.5) \le x \le (c+0.5) \\ 0, & otherwise \end{cases} \tag{4-36}$$

where c is the center position of the binding area. In this case, $w_0(x)$ is constant at 2 μm. These conditions will be imposed on both the change in flexural rigidity and mass and will impose their limits on the integrals for the effective mass and spring constant.

As a result, the new effective spring constant after material binding is

$$k_e' = \int \{D_0(x) + \Delta D(x)\}[\bar{u}''(x)]^2 dx = k_e + \int \Delta D(x)[\bar{u}''(x)]^2 dx \tag{4-37}$$

The mass per unit length of the cantilever with added material becomes

$$\lambda(x) = \lambda_0(x) + \Delta\lambda(x) = \lambda_0(x)[1 + \beta\tau w_1(x)] \tag{4-38}$$

which in similar manner as Equation (4-37) leads to

$$m_e' = m_e + \int \Delta\lambda(x)[\bar{u}(x)]^2 dx \tag{4-39}$$

We will avoid using Taylor approximations and use the full solution based on the spring constant formulation used in Equation (4-33) such that

$$\frac{\Delta f}{f} = \sqrt{\frac{k_e'/k_e}{m_e'/m_e}} - 1 = \sqrt{\frac{1 + \frac{1}{k_e}\int_0^l \Delta D(x)[\bar{u}''(x)]^2 dx}{1 + \frac{1}{m_e}\int \Delta\lambda(x)[\bar{u}(x)]^2 dx}} - 1 \tag{4-40}$$

Full evaluation of Equation (4-40) will yield the frequency response profile of the cantilever as a function of the center of the bound material, *c*. Notice here that if deposition is uniform, ΔD and $\Delta\lambda$ are no longer a function of *x* and the integrals will cancel out with those in k_e and m_e, giving the same result as Equation (4-30) for uniform unilateral deposition of material.

The above equations again show that the important parameters governing the frequency response profiles appear as ratios of stiffness, width, thickness, and density

of the added material to the resonator. Note that frequency response profiles exist in a complicated multi-dimensional space defined by the ratios of these materials parameters and will be different for each system. The frequency response profiles for locally patterned regions of material on a silicon nitride cantilever will be calculated for several values of each ratio, while holding others constant, in order to illustrate how each quantity affects the frequency shifts. Base parameters of E_1=100 MPa, w_1=1 μm, t_1=5 nm, and ρ_1=1 g/cm^3 are used for the added material while E_0=203 GPa, w_0=2 μm, t_0=150 nm, and ρ_0=3.1 g/cm^3 are used for the silicon nitride cantilever. The normalized displacement distribution function for the fundamental mode of a cantilever can be described by

$$\bar{u}(x) = -\frac{45}{26}\left(\frac{x}{l}\right)^2 + \frac{10}{13}\left(\frac{x}{l}\right)^3 - \frac{1}{26}\left(\frac{x}{l}\right)^6 \tag{4-41}$$

which is an approximation of the mode shape solution for resonant prismatic cantilever beams given by Equation (4-8).

In the following plots of frequency response profiles for changing stiffness, width, thickness, and density ratios, the origin is defined at the base of the overhang, as used above in the discussion of cantilevers and paddlevers. In addition, there will be four different regions of the curves due to convolution of the integral limits with discontinuities in ΔD(x). The first region from c = -0.5 to 0.5 μm is a result of the localized pad moving from being off of the device altogether to being entirely on the overhang. The next region is present from c = 0.5 to 1.25 while the pad is on the overhang. From c = 1.25 to 2.25 is a transitional section where it is partially on the overhang and partially on the cantilever. The remaining part of the curve is due to the square of added material being located on the 2 μm wide part of the cantilever.

First, the effect of material stiffness on the frequency response profile of a cantilever is shown in Figure 4-18(a). At a first glance, it is evident that the stiffness of added material is only sensed near the clamped portion of the cantilever and has no effect near the tip, where all curves overlap. For ratios of 1/100 or less, the effect of stiffness is negligible in this case, while for stiffness ratios on the order 1/10 or greater, the stiffness has a rapidly increasing effect on the frequency shift and approaches the magnitude of mass-related, negative shifts when the binding pad is at the cantilever tip.

However, the overhang may be reducing the effects of stiffness since the width of the added material is significantly less than the width of the overhang. According to Equations (4-34) and (4-35), the stiffness and width ratios are closely related in producing changes in flexural rigidity, which has the greatest effect near the clamping point of the cantilever. If the overhang width is reduced to 2 μm like the rest of the cantilever, material stiffness has an increased effect, as shown in Figure 4-18(b). This reveals that the overhang inherent to this type of fabrication process reduces the effects of added material stiffness and biases the devices towards mass detection. On the other hand, stiffness ratios of 1/100 or greater are still required for flexural rigidity effects to appear. While the effect of material stiffness could be increased by making cantilevers out of softer materials in order to increase the stiffness ratio and its sensitivity to added flexural rigidity, softer materials like polymers may significantly reduce the quality factor and in turn the sensitivity of the sensors.[35]

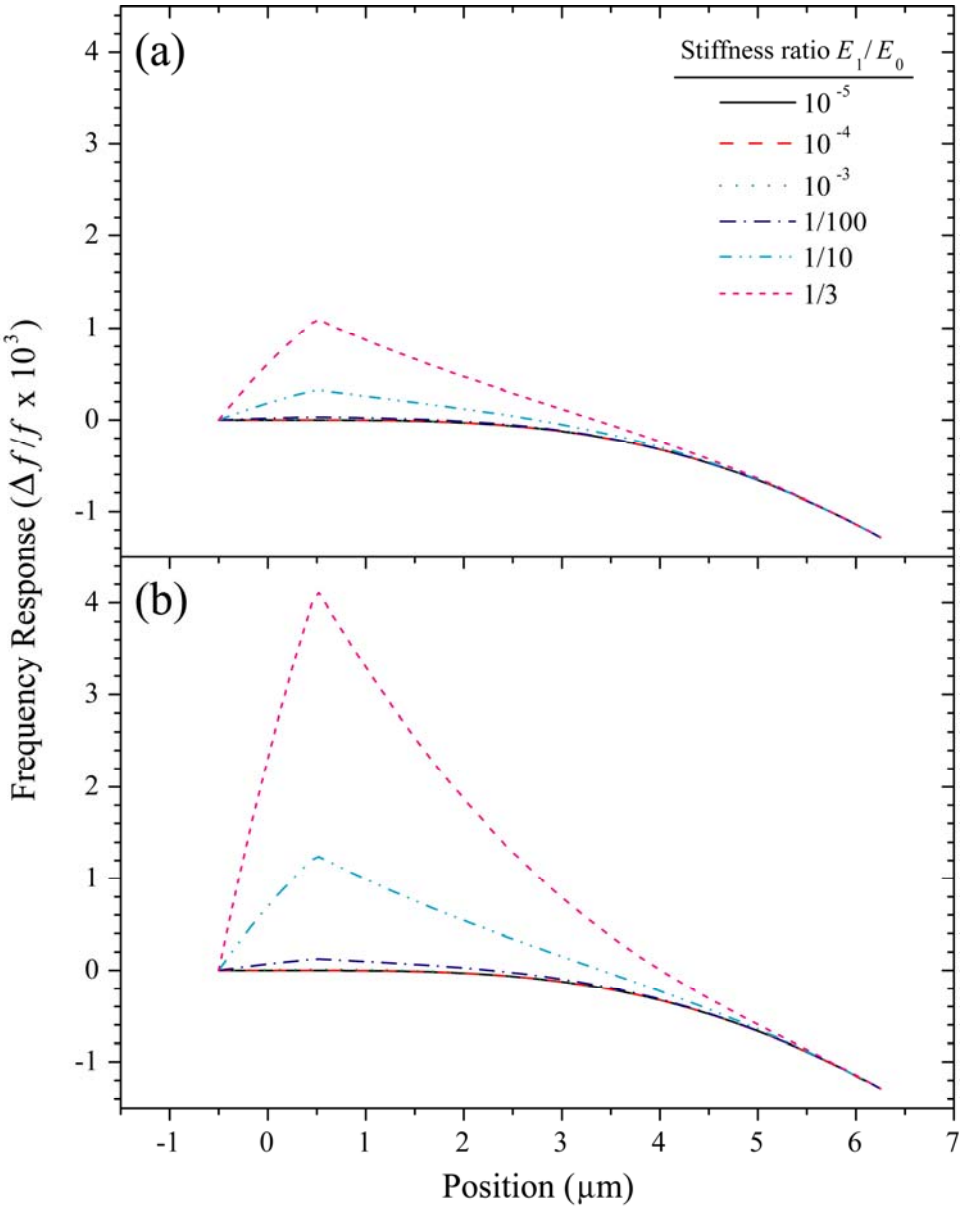

Figure 4-18. Frequency response profiles for several different stiffness ratios on cantilevers with a (a) 10 μm wide and (b) 2 μm wide overhang. The effect of material stiffness is confined near the clamped end of the cantilever where significant bending occurs, leading to the different frequency response amplitudes for cantilevers of different overhang widths.

Frequency response profiles for varying width ratio (added material width to the width of the cantilever, here 2 μm) are shown in Figure 4-19. As the regions of bound material become wider, the mass of the resonator increases, while there is no significant change in the flexural rigidity in this case, with a 10 μm wide overhang. Below a width ratio of 1/10, even frequency shifts due to mass will become very small or insignificant. However, in the interest of maximum sensitivity, a width ratio of 1 gives the largest frequency response and should always be used if possible. This is also true for stiffness sensing, as shown in Figure 4-19(a) and (b), which compare width ratios on the overhang of 0.2 and 0.5, respectively. The larger width ratio of 0.5 gives a larger frequency response, and a ratio of 1 on the overhang region will also give a maximum response.

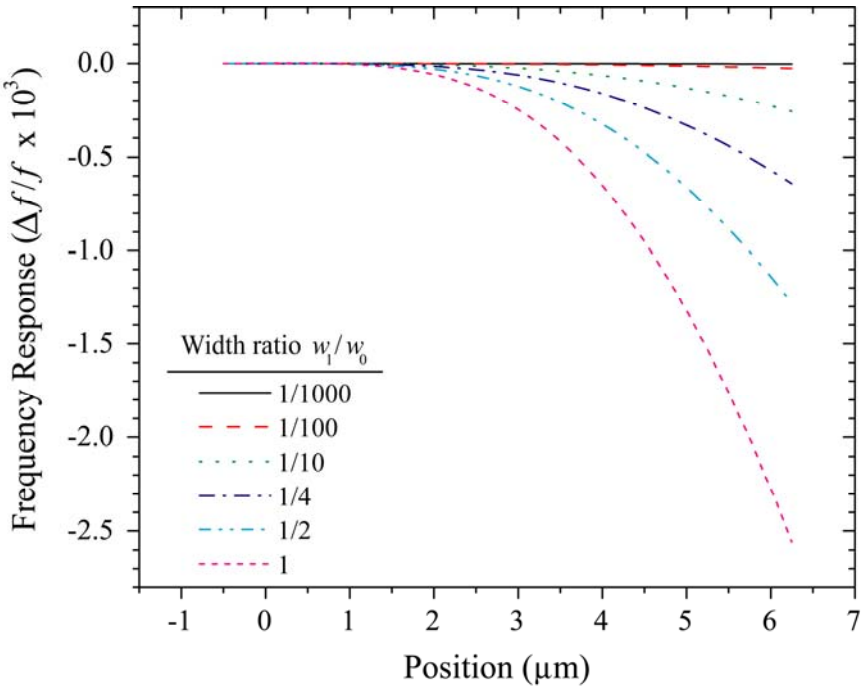

Figure 4-19. Frequency shifts as a function of position for several different width ratio values, where w_0 is the width of the cantilever.

The effect of thickness ratio on the frequency response behavior of a cantilever was calculated for several different values and is shown in Figure 4-20. As t_1 increases, the positive frequency shifts related to flexural rigidity are expected to increase in amplitude more rapidly than the negative, mass-based shifts, due to the higher powers of t_1/t_0 present in Equations (4-34) as compared to Equation (4-38). However, in this case, where E_1 = 100 MPa, the thickness ratio does not significantly change the very small, positive frequency shifts observed near the cantilever base. Another important feature of Figure 4-20 is that at low thickness ratios, detection of added material will become very difficult, suggesting that the sensor thickness should not be several orders of magnitude thicker than what is being added to it. Otherwise, frequency shifts will be very small or even unobservable for changes in both flexural rigidity and mass.

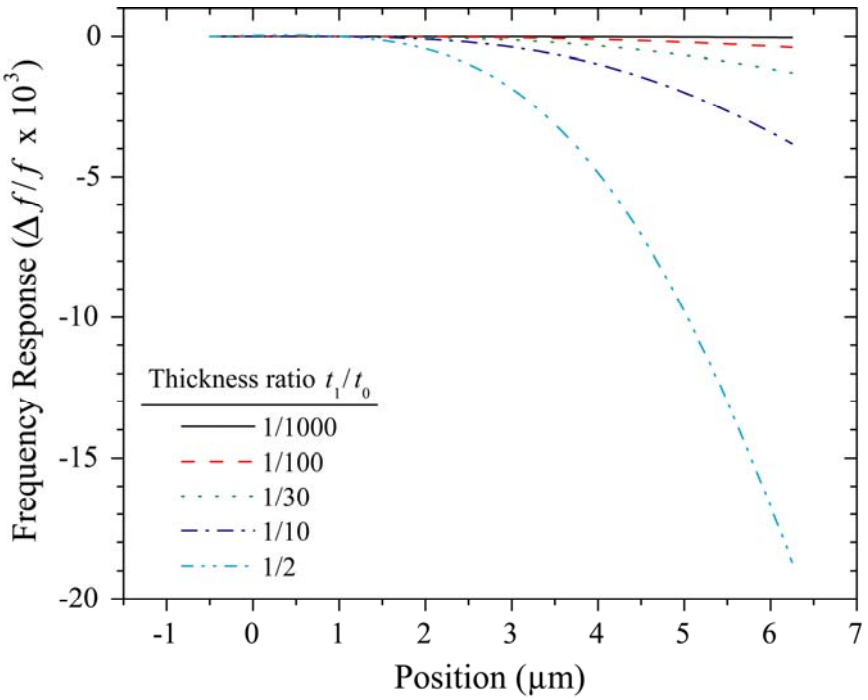

Figure 4-20. Frequency response curves for the effect of thickness ratio on the resonant frequency of a cantilever.

Frequency response profiles for varying density ratios were calculated and are shown in Figure 4-21. As the ratio of densities increases, so do the negative, mass related shifts, as expected. In addition, the curves are all the same near the clamped end of the cantilever, emphasizing that changes in mass have no effect in this part of the device.

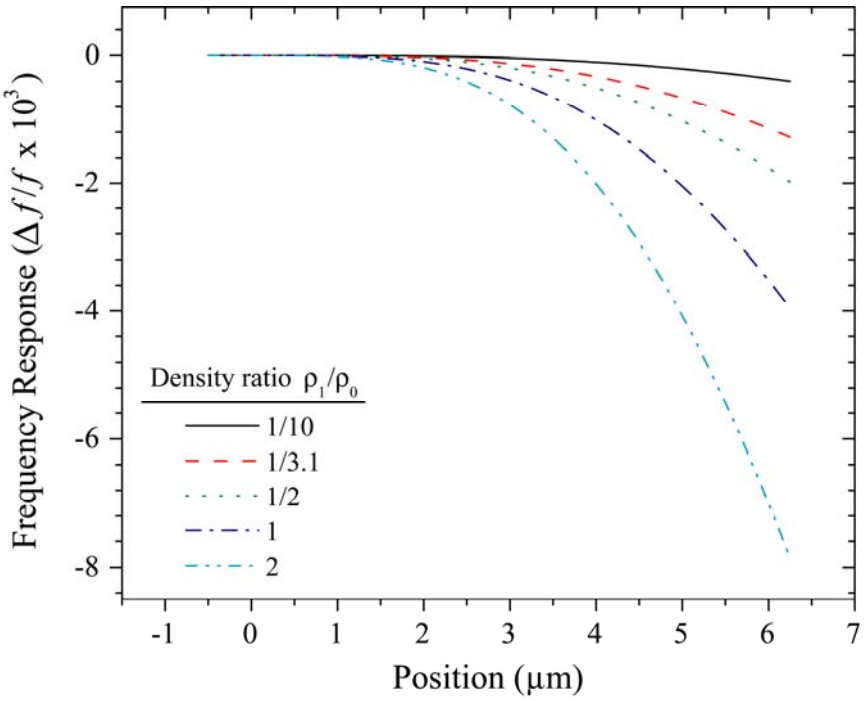

Figure 4-21. Plot of cantilever frequency response profiles shown for several density ratios. Larger density ratios result in larger negative frequency shifts near the cantilever tip, while there are no changes near the clamped end.

4.4 Effect of Resonant Mode

Resonant modes represent another degree of freedom present for MEMS and NEMS resonators. They include the higher harmonics of fundamental resonances,

such as those described by Equation (4-8) and shown in Figure 4-1 above for a cantilever. Also included, however, are entirely different resonances, such as twisting or torsional resonance, or in-plane flexural resonance which is orthogonal to the transverse (out-of-plane) cantilever modes described by Equation (4-8). As device geometries become more complex, additional families of resonant modes arise, such as the wingflap mode of a paddlever, (device shown in Figure 4-9(b)), where the two sides of the paddle move in and out of plane in-phase (unlike the out-of-phase motion of the torsional mode) and the central length of the paddle remains roughly stationary. We now will discuss these modes, how they can affect the sensing mechanism, and assess their utility in potential applications.

Using higher modes does not necessarily mean higher sensitivity. In fact, using higher modes to detect uniformly bound films will result in the same $\Delta f / f$ response as the fundamental mode. As shown in Equation (4-9), the only difference in using higher harmonics is a higher frequency due to the higher coefficient—the functional form stays the same, meaning the same frequency response. While the exact shift in frequency will be larger for devices with initially higher frequencies, their frequency peak resolution will be proportionally worse, because Q is given by the peak frequency over the full width at half maximum. Even if a higher mode has the same Q but twice the frequency of the fundamental mode, its peak width will also be twice that of the fundamental mode. Unfortunately, in vacuum, higher harmonics of fundamental modes often have progressively lower Q, although higher frequency non-transverse modes have exhibited relatively higher values for Q. However, this behavior changes when viscous damping is present, and higher modes can become very beneficial, as will be discussed in Section 4.4.2.

4.4.1. Resonant Mode and the Detection of Localized Binding[1]

In the same way as discussed in Section 4.3.1, the ability of higher resonant modes to detect localized binding was studied with carefully placed gold pads. A second out-of-plane resonance was observed in 8 μm long cantilevers, and the frequency response as a function of position is shown in Figure 4-22. This resonance was determined to be the first harmonic, out-of-plane mode since the resonant frequency agrees with finite element simulations and the frequency response goes to zero at one point in the middle of the cantilever, signifying a single node in the cantilever resonance. The frequency response at the tip is ~25% lower than that of the first mode, which agrees with previous observations.[28]

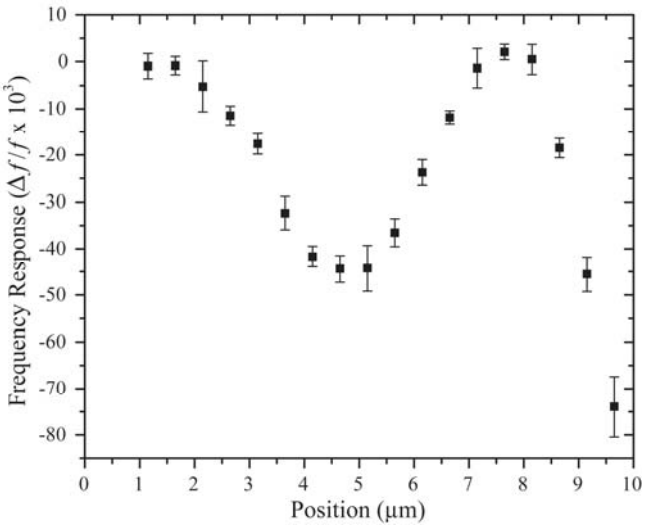

Figure 4-22. Plot of the frequency response to gold pad location for the first harmonic resonant mode of an 8 μm long cantilever. The node in the resonant mode shape corresponds to a node in the frequency response as well.

The torsional mode of paddlevers (5 μm long with 10 μm wide paddles) was also studied experimentally and modeled by finite element simulations. The first two

modes predicted by finite element analysis are the fundamental (2.58 MHz) and torsional (3.65 MHz) modes, and the experimentally observed higher mode at 3.67 MHz agrees with the frequency of the modeled torsional mode. Experimental data is plotted along with point-mass simulations in Figure 4-23(a). The simulations agree very well with the data, as shown in Figure 4-23(b). While point-mass simulations are in agreement with experimental values, they slightly underestimate the resonant frequency shifts in the middle of the paddle. Simulations including the stiffness of gold improve the agreement, but the difference is fairly small, differing on average by $-1.9 \pm 8.7\%$ from experimentally measured values. So, for this mode of resonance, gold pads effectively act like point masses along the width of the paddle. The data also confirms that this is not the fundamental resonant mode or a more complex wing flap mode since the frequency response approaches zero at the center of the paddle, just as would be expected for torsional resonances. It is interesting to note that the torsional frequency responses for gold pads placed at the paddle ends are a factor of two larger than for any location in the fundamental mode, shown in Figure 4-15.

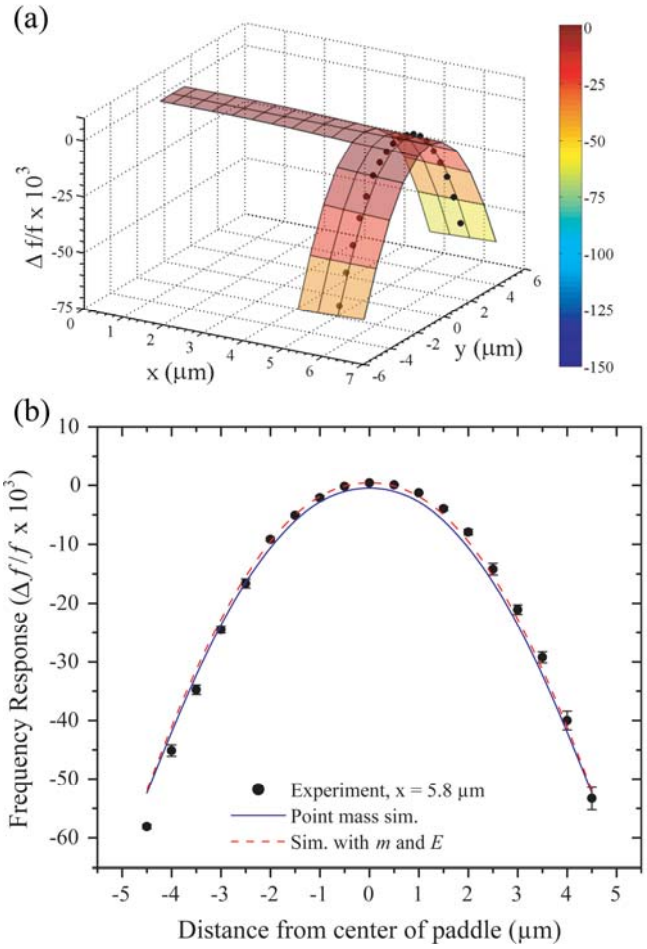

Figure 4-23. (a) Experimental data plotted with point-mass simulations for the torsional mode of 5 μm long paddlevers with 10 μm wide paddles. (b) Two dimensional plot of the frequency response with simulations. Changes in the flexural rigidity are apparent only in the paddle center, where the experimental data deviates slightly from point mass simulations.

4.4.2 Viscous Damping Applications[2]

Viscous damping has long been the most significant factor limiting the quality factor (Q) of resonant MEMS and especially NEMS from use in air or liquids. It defeats resonant sensing in fluids with a two-pronged attack that both reduces the quality factor and adds effective mass to the sensor that in turn reduces its sensitivity to changes in mass. When a small amount of mass is added to the resonators, the frequency will decrease some amount given by

$$\frac{\Delta f}{f} = -\frac{1}{2}\frac{\Delta m}{(m_r + m_{viscous})} \tag{4-42}$$

where m_r is the resonator mass and $m_{viscous}$ is the effective mass of the viscous medium. Therefore, the sensitivity for the same amount of added mass is higher in vacuum where $m_{viscous}$ goes to zero.

Higher harmonics of the fundamental resonant mode have shown promise for operation in air or liquid because the quality factor increases with frequency and the mass of the entrained fluid is reduced.[10,22,28,36,37] In addition, more complex resonant modes, such as torsional or in-plane resonances, may perform better because of the inherently different way in which they interact with the viscous media.[22,36,38] Higher resonant modes have also used with sensors operated in air[39] and liquid[40-41] and demonstrated improved sensitivity in both cases.

Interest in the in-plane, or strong-axis bending, modes has increased recently, because these devices interact minimally with the surrounding fluid, effectively slicing through it. An analytical model has been presented[42] for transverse resonance of

cantilevers in viscous environments using a scaling parameter, T, that is the ratio of added mass of the viscous medium to that of the cantilever, given by

$$T = \frac{\rho}{\rho_c}\frac{b}{h} \tag{4-43}$$

where ρ and ρ_c are the densities of the fluid and cantilever, b is the cantilever width, and h is the cantilever thickness. This aspect ratio of b/h is responsible for the large added masses for cantilever sensors, which are typically both wide and thin in order to maximize surface area for binding while reducing sensor mass. However, if those same cantilevers were excited into in-plane rather than transverse resonance, T becomes proportional to h/b instead, greatly reducing the amount of added fluid mass, while still permitting a large surface area for sensing purposes. Also presented in this model is an expression for quality factor that is inversely proportional to T. So by the same arguments above, the in-plane mode should have a significantly larger quality factor in air as compared to the fundamental transverse mode. Recent theoretical work using numerical simulations of microscale cantilevers has also suggested that such in-plane modes should yield significantly improved quality factors and sensitivities in air or liquid.[38] Specifically, the model predicted that the quality factor of the in-plane mode would be ~45 times larger than that of the fundamental transverse mode in air, and roughly 15 times larger in liquid. If these in-plane modes could be harnessed for sensing applications, devices with high surface areas and low thicknesses, *i.e.* with large surface-to-volume ratios, could still be used to maximize sensitivity.

With this in mind, we have fabricated 90 nm thick trampoline resonators with relatively high surface area (~172 μm^2) and tested the behavior of higher resonant modes in air. The fabrication process and experimental details are all discussed in

Chapter 3 and the device geometry is the same as that shown in Figure 4-9(c). Several higher modes were observed with quality factors greater than 2000 at atmospheric pressure, including two symmetric in-plane resonances. Finite element analysis was been used to model the resonant modes of the geometrically complex devices in order assign mode shapes to experimentally observed resonances. In addition, by comparing these resonances to finite element simulations that account for the HF undercuts, we determined the stiffness and density of the low stress silicon nitride to be 150 GPa and 3.1 g/cm^3, respectively. Finally, we evaporated a polymer that has been used in gaseous sensing applications onto the resonators.[43] This functional layer added to the resonators, 4-*tert*-butylcalix[6]arene (95%, Sigma) was thermally evaporated onto the devices with a thickness of 10 nm, as measured by a quartz crystal thickness monitor assuming a density of 1 g/cm^3. Resonant frequencies and quality factors were measured before and after deposition in order to determine how the evaporated polymer layer affected device resonances. Only a small decrease in the quality factor of higher resonant modes was observed, which is quite promising for use of these and similar devices in atmospheric sensing applications.

Many different resonant modes of the trampolines were observed experimentally; however, finite element analysis was required to assign particular resonant modes to the observed peaks. In addition, finite element simulations assisted in discerning nanomechanical resonances from intrinsic resonances of the macroscopic piezoelectric resonator. A comparison of simulated and experimentally measured peaks is shown in Table 4-1, where the resonant modes are designated using nomenclature for square plate resonators with clamped edges.[44] The pair of torsional modes as well as the in-plane modes are likely non-degenerate due to fabrication variations. We note that the finite element simulations better predict the lower frequency resonant modes, with increasing error for higher modes. Two unknown

resonant modes remained unassigned due to the high density of simulated modes near their frequency as well as the increased discrepancies between experiment and simulation at higher frequencies. Images of the identified resonant modes are shown in Figure 4-24, depicting the displaced shape and node pattern of the device for each mode.

In order to assign the in-plane modes to observed frequency peaks, additional testing was required. First of all, the two peaks observed at 34.9 and 35.0 MHz were closely spaced in frequency and alternated in intensity as the interferometric readout laser was scanned across the resonator surface, much like the two orthogonal torsional modes at f_{10}=3.01 and f_{01}=3.05 MHz, suggesting that these two peaks were also symmetric and orthogonal modes. However, in order to ascertain the mode identity, optical excitation was used to actuate these resonances in a non-uniform manner. By focusing the excitation laser on each of the four clamping arms, we were able to excite vibrations along the direction of that particular support arm. When focused on each individual support arm, one of two peaks appeared, as shown in Figure 4-25. In fact, exciting resonance using the top and bottom support arms produced the resonant mode near 34.9 MHz while the left and right support arms produced the peak near 35.0 MHz. We note that the use of laser drive with devices featuring more than one clamping point typically gives rise to unstable resonant peaks due to thermal effects as well as the non-uniform excitation method, leading to the slight differences in peak frequencies observed in Figure 4-25.

Table 4-1. Experimental and Simulated Trampoline Resonant Modes

Experimental		Finite Element Analysis			
f (MHz)	Q	Mode Designation[44]	Description	f (MHz)	Error
1.64	5908	(0,0)	Fund. Transverse	1.63	0.61%
3.01	4014	(1,0)	Torsion y	3.00	0.33%
3.05	4881	(0,1)	Torsion x	3.00	1.64%
6.74	5308	(1,1) – {(2,0) – (0,2)}	Saddle 1	6.58	2.37%
7.87	4872	(1,1) + {(2,0) – (0,2)}	Saddle 2	7.71	2.03%
11.1	3899	(2,0) + (0,2)	1st Harm. Transverse	9.87	11.08%
16.4	6028	--	Unknown	--	--
34.9	6687	--	In-plane y	41.5	18.91%
35.0	6386	--	In-plane x	41.5	18.57%
35.5	4904	--	Unknown	--	--

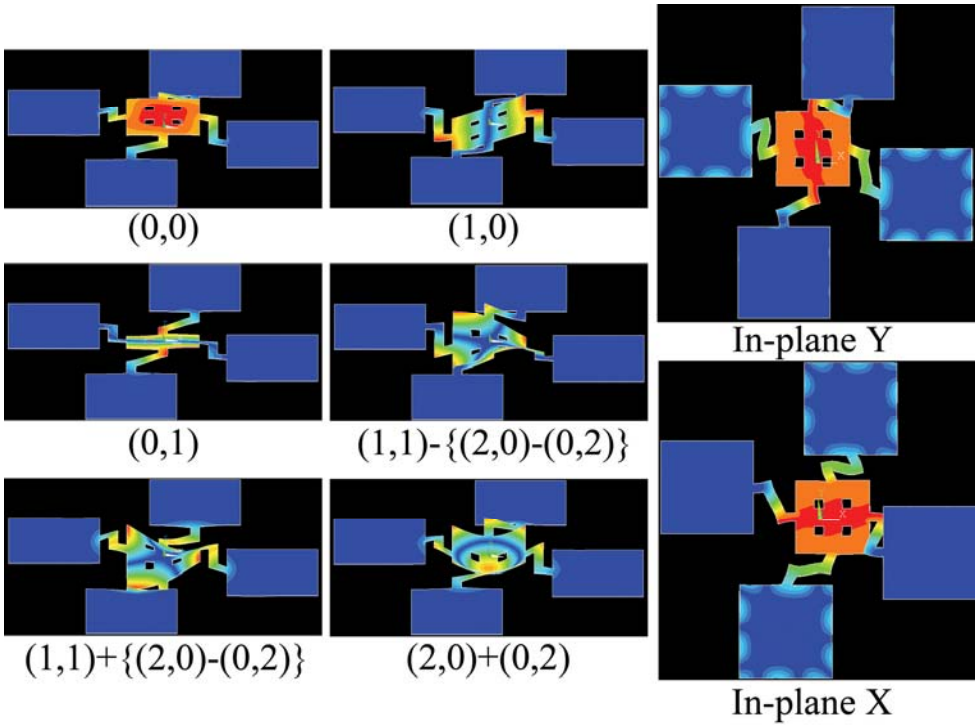

Figure 4-24. Images of the resonant modes from finite element simulations depicting the displacement and nodal structure for each mode. The simulations also predicted two symmetric in-plane resonant modes, degenerate in frequency.

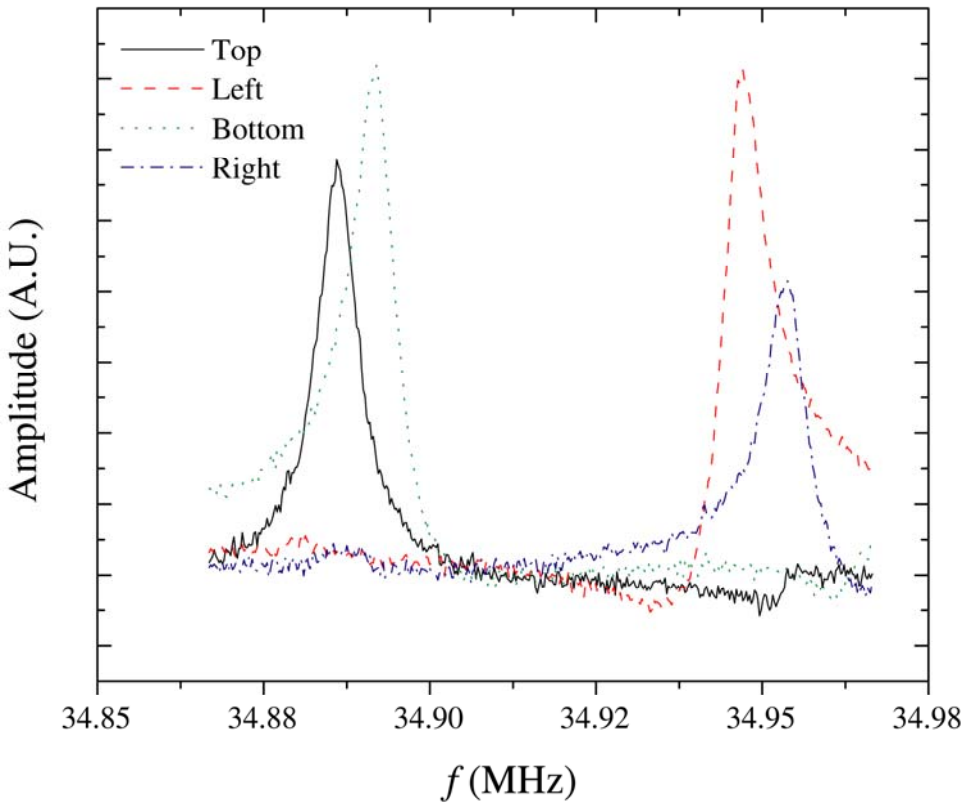

Figure 4-25. In-plane mode resonance peaks driven by localized optical excitation on each of the four trampoline support arms. Opposite supports participate in the same resonant mode, signifying that these are in fact two symmetric, in-plane resonant modes of the trampoline. Note that the frequencies are not degenerate, likely due to minor asymmetry in device fabrication. Small differences in shape are attributed to the non-uniform excitation and thermal effects associated with the optical excitation.

The quality factors for these resonant modes varied from 4000-7000 when measured in vacuum, as shown in Table 4-1. These values decreased significantly as the pressure was increased to atmospheric pressure, where higher resonant modes have been observed to have increasingly larger quality factors while the fundamental mode

has the lowest Q.[10,28,36] By tracking the resonances as the chamber pressure was slowly increased towards atmpospheric pressure, each could be definitively identified. The behaviors of the quality factors as a function of pressure for the fundamental and first harmonic transverse modes, the two in-plane resonant modes, as well as the unknown mode at 35.5 MHz are shown in Figure 4-26(a) and (b). While the quality factor of the first harmonic mode is lower than that of the fundamental in vacuum, at atmospheric pressure the opposite is true, as previously observed with the harmonics of doubly-clamped, nanomechanical beams.[10] The quality factors of the two in-plane modes however were higher in both vacuum and air than the other modes and followed roughly the same curve as one another. However, this behavior does not appear to depend on frequency alone, as the higher frequency unknown mode has a lower Q both in air and vacuum than the in-plane modes, suggesting that the in-plane modes interact with the air to a lesser degree. Because some resonances become undetectable at higher pressures due to low signal or interference with neighboring piezoelectric resonances, the quality factors of all modes were compared at 30 Torr and are shown in Figure 4-26(c), demonstrating again that higher frequency resonant modes have higher quality factors than the fundamental mode when operated near atmospheric pressures.

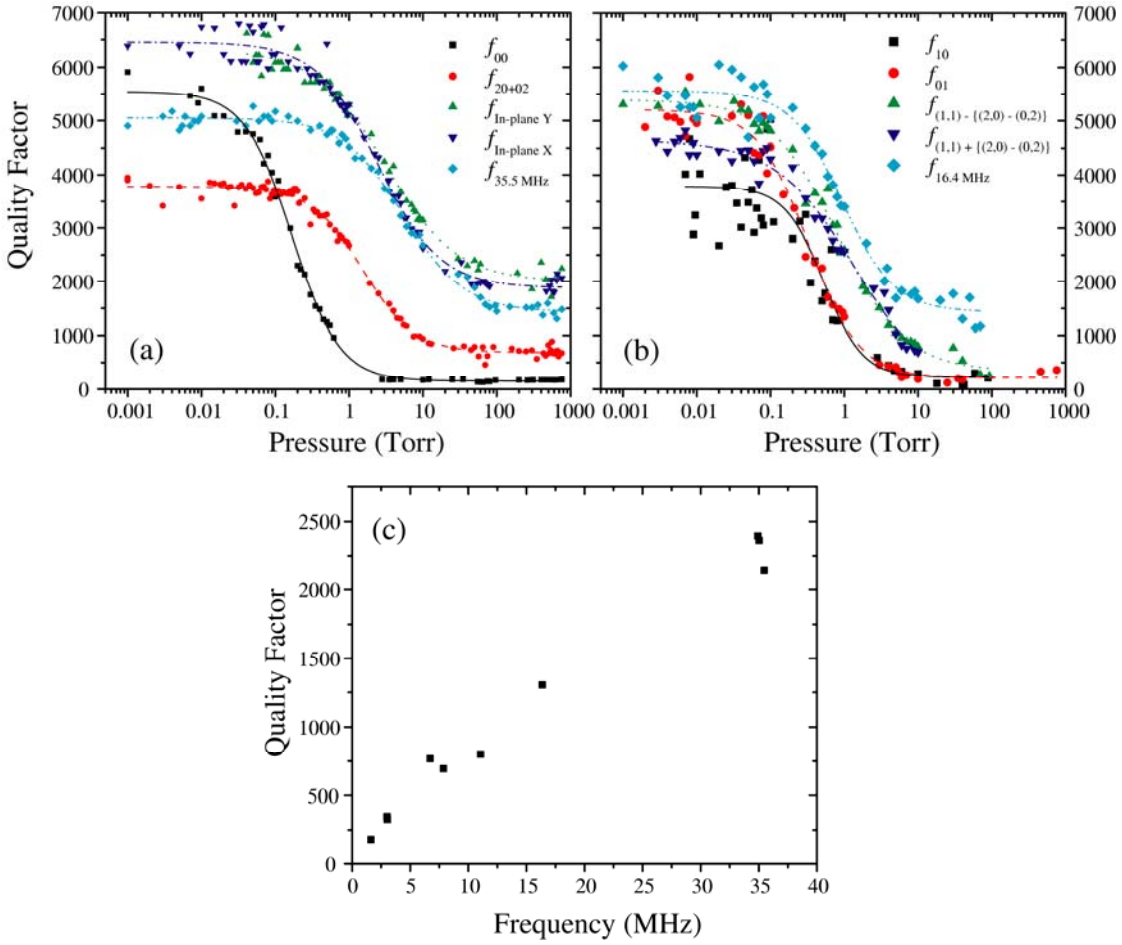

Figure 4-26. Quality factor shown (a) and (b) as a function of pressure and (c) as a function of resonant frequency for all modes at 30 Torr.

Another important factor to consider is the added mass of the viscous medium that is typically responsible for decreasing the resonant frequency of a device with respect to its frequency in vacuum. This entrained mass effectively reduces the mass sensitivity of the resonator, so the optimal resonant modes for sensing would feature only small frequency shifts when operated from vacuum to atmospheric pressure. The frequency shifts were tracked as a function of pressure and are shown in Figure 4-27. For some modes, relatively high laser powers were required for detection, resulting in constant thermal drifts in resonant frequency; these were carefully measured and subtracted from the data in order to isolate the pressure dependence of the frequency. The fundamental mode began to decrease rapidly in frequency at pressures above ~700 mTorr, eventually decreasing by roughly 0.55%. For the higher modes, the quality factor began to decrease at progressively higher pressures and, the frequency shifts were much smaller. Clearly, the resonant frequencies of three highest frequency modes are not strongly affected by operating at high pressures, with both the in-plane modes and the unknown 35.5 MHz mode behaving similarly.

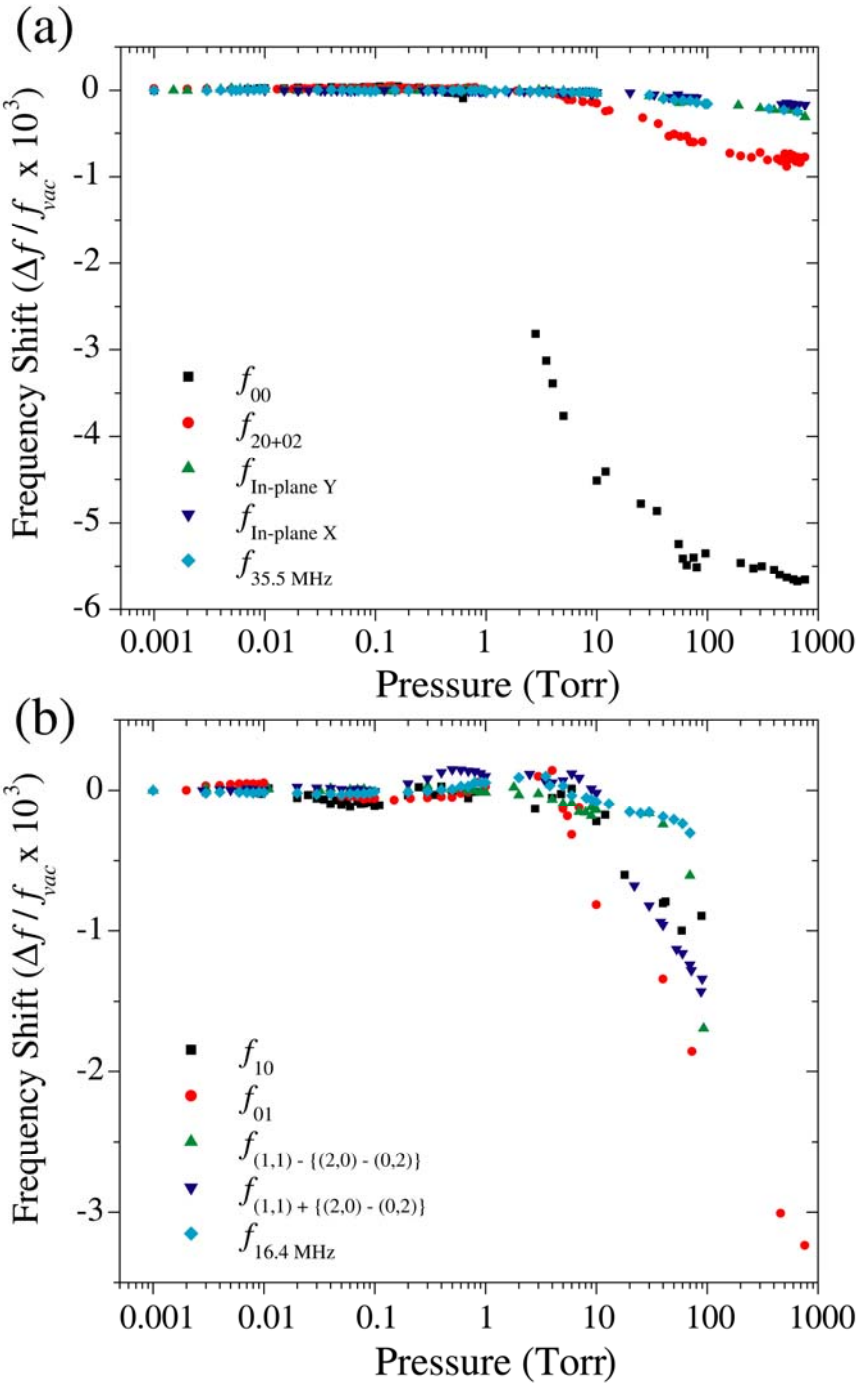

Figure 4-27. Frequency shifts for several resonant modes resulting from added mass of entrained air that moves in phase with the devices. For higher resonant modes, the quality factor in vacuum was preserved to higher pressures and the overall frequency shift decreased.

In order to select the optimal resonant modes for sensing in ambient or near-ambient pressure, we have devised a figure of merit, F, to condense the above discussion mathematically. Ideally, a resonant gas sensor would need a high Q at high pressures and should not suffer a loss in sensitivity due to the added inertial mass of air moving with the device, which would correspond to large values of the following

$$F = \frac{Q}{\left|\Delta f / f_{vac}\right|} \tag{4-44}$$

where Q is the quality factor and $\left|\Delta f / f_{vac}\right|$ is the frequency shift magnitude from Figure 4-27. This quantity was calculated for the resonant modes discussed above and is plotted as a function of pressure in Figure 4-28(a) and (b). Pressures below 1 Torr are excluded because there is essentially no frequency shift for any mode, in which case the resonant mode should be chosen based only on its quality factor as they all have equivalent masses and thus mass sensitivities to uniform mass loading. The in-plane resonant modes behave similarly, both having higher values of F than all other modes at pressures of about 10 Torr and above. If all of the resonant modes are considered for use at 60 Torr, the in-plane resonant modes are still the most desirable, as shown in Figure 4-28(c).

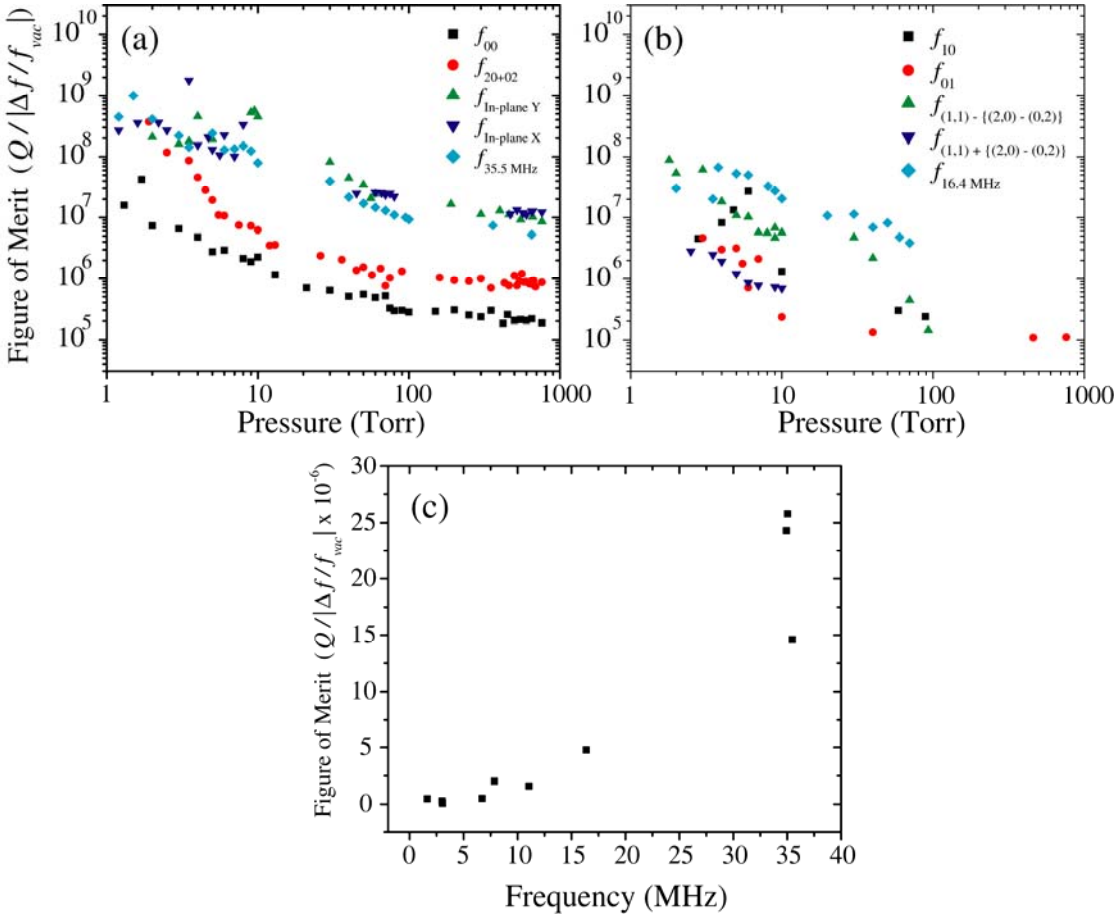

Figure 4-28. (a-b) Comparison of several resonant modes using the figure of merit given in Equation (4-44), revealing that the in-plane modes perform the best in the high pressure regime. (c) Figures of merit shown as a function of resonant mode frequency using all resonances at 60 Torr, again supporting the use of in-plane modes for sensing at high pressures.

Another important consideration that is more difficult to quantify is the signal-to-noise ratio for the resonance signal, as it will depend on the drive and detection techniques, readout electronics, system alignment, and pressure. This should be taken into consideration when designing a sensor and selecting a resonant mode for operation. If necessary, operating the sensor at a slighty reduced pressure would be advantageous and conceivable if the sampling air flow were configured to reduce the pressure in the vicinity of the sensor.

Despite the high quality factors demonstrated by these nanomechanical trampoline resonators in air, a sensing layer with at least some specificity for a target analyte must be added to the device, which could significantly degrade the quality factors. For the detection of chemical vapors from air, polymer coatings are typically used to absorb these vapors and swell, causing a change in stress, conductivity, or some other physical quantity. In order to test the response of these devices to the addition of a mechanically lossy sensing layer, 4-*tert*-butylcalix[6]arene was evaporated on the devices. The frequencies and quality factors of the fundamental and the 35 MHz in-plane (along the x direction) modes were measured before and after evaporation in order to highlight the extremes in sensitivity for detection in air. The frequency shifts from an array of devices in vacuum were measured for each of these modes and used to measure the thickness of the deposited polymer layer. Assuming a negligible flexural rigidity and a density of 1 g/cm^3 for the polymer, the thickness was calculated from Equation (4-12) to be 8.9 ± 0.6 nm using both resonant modes.

More importantly, the quality factors of these two modes were measured before and after deposition at both vacuum and 30 Torr and are shown in Figure 4-29. While 30 Torr was chosen for these measurements because of the relatively large signal-to-noise ratios for the resonant peaks, the quality factors did not differ significantly from those at 760 Torr, as suggested by the data in Figure 4-26, though

the amplitudes decreased somewhat. In vacuum, the modes behave similarly and their quality factors both decreased by roughly 45%. However, at 30 Torr, the already low average quality factor of 115 for the fundamental mode was reduced to ~50. In contrast, the in-plane modes started with a Q of about 2200 on average but only decreased to ~1800 after deposition of the polymer. Even after adding a mechanically lossy film that increases the resonator thickness by ~10%, the quality factor of the in-plane modes decreased by only a small amount. Taking the ratio of quality factors for the in-plane mode to the fundamental transverse mode gives a value of ~20, which is on the same order of magnitude but less than the value predicted by simulations for cantilever resonances.[38]

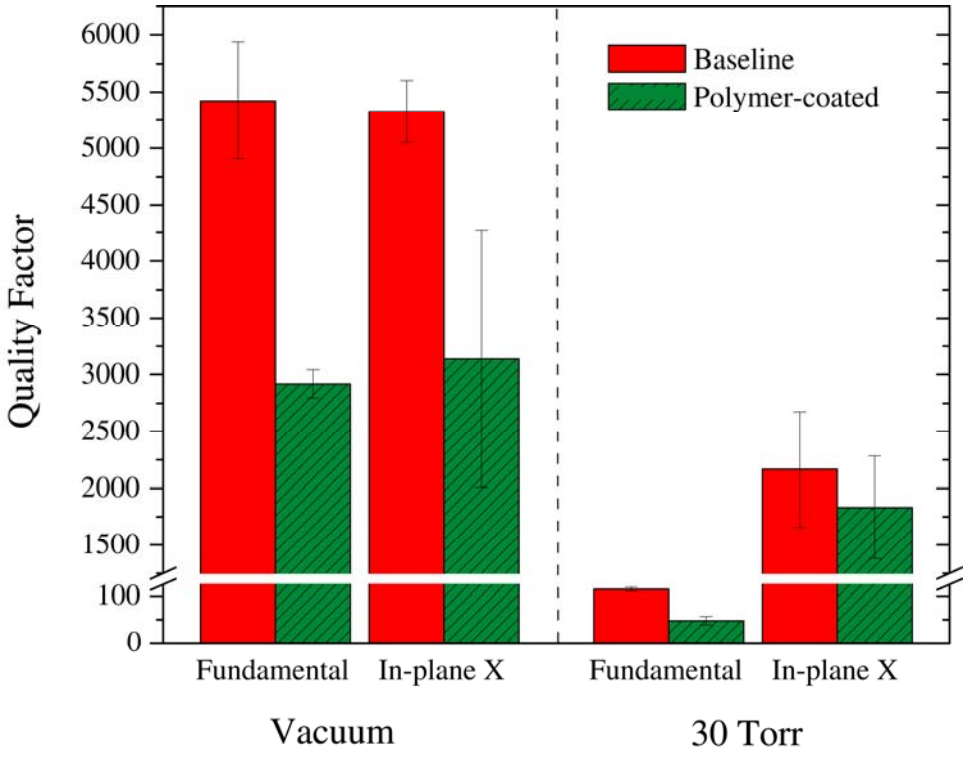

Figure 4-29. Comparison of the fundamental and in-plane (x-direction) resonant mode quality factors before and after deposition of an 8.9 ± 0.6 nm polymer layer, measured in vacuum and at 30 Torr.

4.5 Building a Better Resonant Sensor[1]

After investigating and discussing the many facets of resonant sensors and the underlying physics, one should be able to tune sensor design for the expected mechanical properties and deposited amount of analyte material. Minimizing the resonator mass is an obvious way to maximize sensitivity that is followed often in the literature, and the surface-to-volume ratio is one key ingredient in improving the sensitivity of a device while keeping its total mass constant. This points towards the use of devices that are as thin as possible. In fact, graphene resonators made from a single sheet of carbon atoms[45] have been realized, as well as carbon nanotube resonant sensors,[46] representing the ultimate limits of resonant sensor minimization.

On the other hand, the sensor needs to be tuned for the application. As seen in the ALD experiments described in Section 4.2.3, if relatively large amounts of material are added to a resonant sensor, the Q is likely to drop off dramatically and reduce sensitivity. The dynamic range of the sensor should similarly be controlled so that devices which are too thick or too thin should not be used to measure a particular deposition of material. Otherwise flexural rigidity effects will come into play. This and other important issues will be discussed in the following sections.

4.5.1 Competition of Flexural Rigidity and Mass

In situations where frequency shifts due to flexural rigidity and mass changes have similar magnitudes, these results suggest that analyte binding should be specifically localized in order to measure the frequency responses of maximum amplitude and avoid complications. As demonstrated above, the position of localized

binding determines the relative contributions of stiffness and mass and can give varying amplitudes of frequency responses based on sensor geometry and resonant mode. In the experimental material system used here, mass-related shifts were larger than flexural rigidity-related ones. Localization of binding to regions of maximum mass sensitivity may simplify the interpretation of a frequency shift as added mass, and it may also improve the sensitivity, since the deposited material will not contribute significantly to losses and will preserve the quality factor. However, if the flexural rigidity of the deposited material is negligible, the highest mass detection sensitivity will occur when using the entire sensor area, otherwise binding localization carelessly throws out sensitive surface area, reduces frequency response signals, and requires an extra experimental step to define the localized region.

On the other hand, if it is not experimentally feasible to localize deposition, increasing the resonator thickness should be considered in order to restrict the system to the linear region of the response with low thickness ratio, like that shown in Figure 4-6. Though not shown, similar curves are produced if unilateral depositions of relatively stiff material are modeled using Equation (4-30). Otherwise, if typical thickness ratios resulted in small frequency shifts near zero, it would be difficult to tell if a large amount of material was deposited and any more would start producing positive shifts or if only a very small amount of material had been added.

When localized binding is used however, the device geometry and resonant mode determines where bound material should be added. From Figure 4-17, it appears that even when the stiffness ratio is high, the last two microns of the cantilever are still only sensitive to added mass. We then studied the response of different cantilever and paddlever sizes when binding is localized on the last 2 μm of the device using finite element analysis. To maximize frequency responses, the entire width of the device tip would be coated, as suggested by the data shown in Figure 4-19. In order to

demonstrate the effect of localized binding, a 15 nm thick material with a density of 1 g/cm^3 and a stiffness of 20 GPa is added to the 150 nm thick, low-stress silicon nitride devices. If this relatively think and stiff layer is uniformly coated on devices, it causes a small, positive frequency response of ~2.25 x 10^{-3} for out-of-plane resonant modes. For comparison, if the same film has a much smaller stiffness of 100 MPa, the frequency response would be ~ -15.7 x 10^{-3} for both device geometries. The most effective localized binding configuration should result in frequency responses that approach that of the negligibly stiff, 100 MPa film.

Simulation results for these relatively thick added layers are shown in Figure 4-30 as a function of cantilever length and in Figure 4-31 for paddlevers as a function of their (b) length and (c) paddle width. Three different resonant modes common to the two geometries are studied: the fundamental and first harmonic out-of-plane modes as well as the torsional mode. Boundary lines are included on each graph for reference to the frequency responses for the two uniform films.

For the cantilevers shown in Figure 4-30, the fundamental out-of-plane mode gives the largest frequency responses. Binding localization clearly improves the frequency responses for these devices and makes them more sensitive to mass addition than flexural rigidity, with frequency response values near that of the uniform, 100 MPa film. The torsional mode is less sensitive, which is expected since the out of plane motion is relatively small along the center of the cantilever due to the node in the resonant mode shape that runs along the length of the device. The least sensitive mode in this configuration is the 1st harmonic out-of-plane mode.

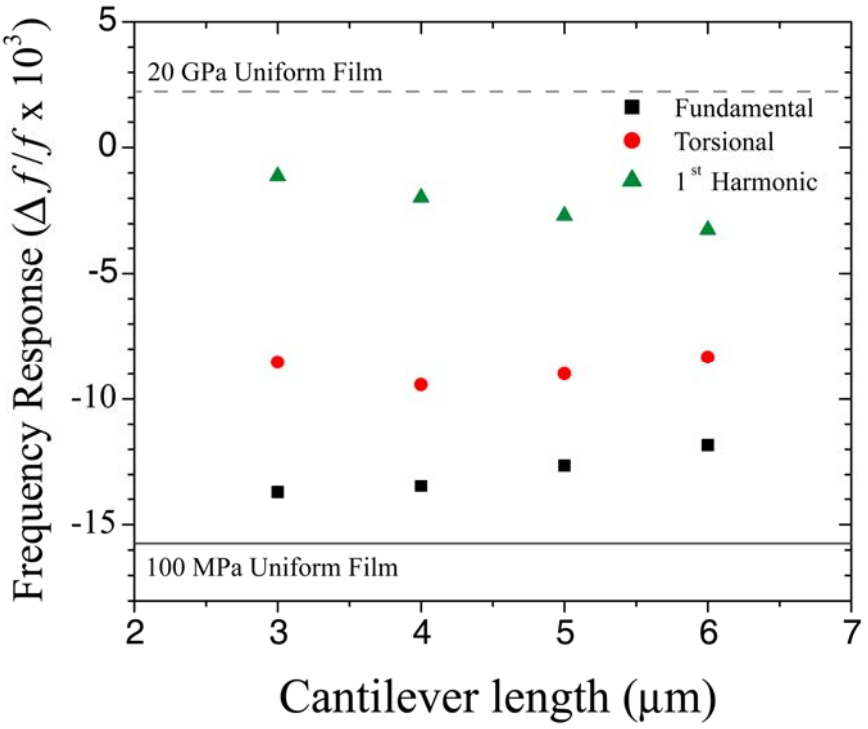

Figure 4-30. Frequency responses due to localized binding of a 20 GPa, 1 g/cm^3 material at the tip (the last 2 μm) of 150 nm thick, 5 μm long cantilevers.

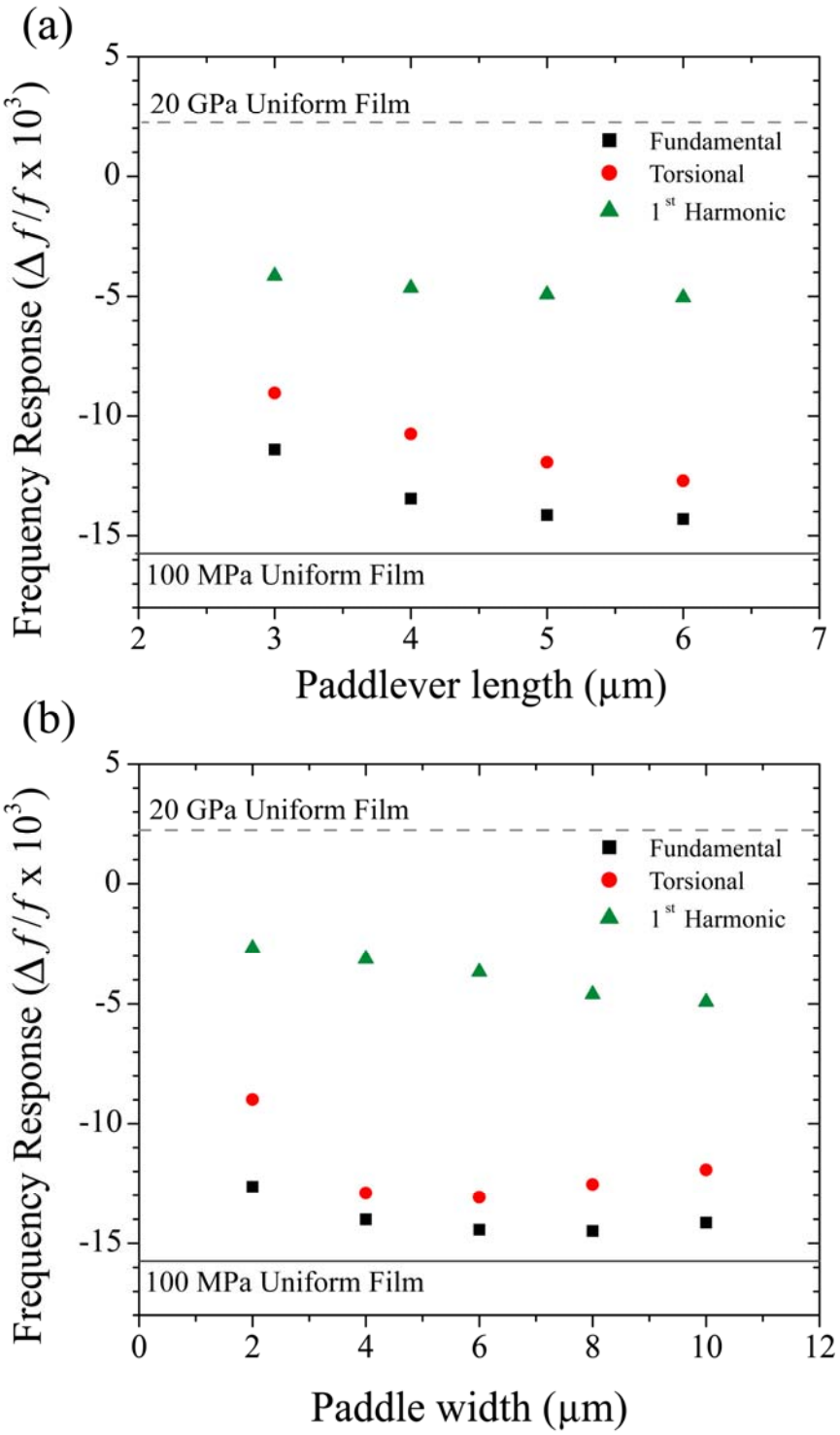

Figure 4-31. Frequency responses due to localized binding of a 20 GPa, 1 g/cm^3 material at the tip (the last 2 μm) of 150 nm thick devices as a function of paddlever (a) length and (b) paddle width for 5 μm long devices.

In Figure 4-31(a), the out-of-plane resonant mode of paddlevers also gives the largest frequency responses to the localized material and is larger than those of the cantilever for longer paddlever lengths. Like the cantilevers, the torsional and 1st harmonic out-of-plane modes have smaller frequency responses. We note that the larger frequency shifts of the torsional modes for paddlevers are likely due to the extended areas of the paddle that move out of plane much more than regions near the central axis of the device, increasing sensitivity to mass added on the paddle. Another noticeable feature of paddlevers is that as they increase in length, the paddle becomes more sensitive to added mass, while the cantilevers in Figure 4-30 show an opposite trend. This can be attributed to small differences in their resonant mode shapes due to the presence of the paddle. The effect of paddle width for 5 μm long paddlevers is shown in Figure 4-31(b). As the paddle width increases from 2 μm to 6 μm, all resonant modes have larger frequency responses. This trend continues for the 1st harmonic out-of-plane mode, while the other two decrease with larger widths.

These results demonstrate that binding localization is effective for reducing competition between mass and flexural rigidity effects and increasing frequency response amplitudes. In addition, the fundamental mode of an 8 μm trampoline resonator of the same thickness was also modeled for localized binding on its center paddle. The frequency response to this localized thick and stiff material was -14.4 x 10^{-3}, which is slightly larger than the frequency responses of the paddlever fundamental modes and larger than those from all cantilever modes. These results show that common rectangular cantilevers can be outperformed by other resonator geometries for the detection of localized depositions of material.

4.5.2 Consequences for Biosensing Applications

It has been suggested that the stiffness of biomolecules and self assembled monolayers could be measured using microcantilevers.[47] However, the Young's moduli used may overestimate the stiffness of the film, as these values were cited from works that measure the *intra*molecular stiffness of the molecules based on bond strengths or secondary structure rather than the overall stiffness of a film.[48,49] The film stiffness would be determined by intermolecular interactions such as charge or steric hindrance effects that would lead to finite flexural rigidity. However, these forces are much weaker than the chemical bonding that makes each individual molecule stiff and makes solid materials like gold, silicon, or diamond even stiffer. For the detection of low analyte concentrations, analyte binding would likely result in sub-monolayer films that would render any intermolecular interactions negligible and potentially negate any stiffness of the film.

For most biosensor applications, the stiffness of biomarker proteins would probably be several orders of magnitude lower than gold. On the other hand, the added mass would be an order of magnitude lower as well. If we estimate a stiffness of ~ 10 to 100 MPa (stiffness ratio ~ 0.5 to 5 x 10^{-4} on silicon nitride resonators) for thin layers of biological material, there would be no significant effect on the flexural rigidity of the device, and no positive frequency shifts would be observed for binding at any location, as demonstrated by Figures 4-18 through 4-21. This could also be an overestimated range of stiffnesses, as the stiffness of biological materials such as skeletal muscle[50] or platelets[51] are on the order of 10 kPa. Therefore, resonators made of relatively stiff materials like silicon or silicon nitride will be more sensitive to the mass of proteins as opposed to stiffness or flexural rigidity. In the case of uniform films, Equation (4-32) can be used to determine the sensing mechanism. For a silicon

nitride resonator and a unilaterally deposited biological film ($\rho \sim 1$ g/cm^3), a null frequency shift would occur at E_1=22 GPa. Detecting ~100 MPa films would give a linear curve with a slope of of -0.32, as the density ratio would be over 300 times larger in magnitude than the stiffness term, meaning that mass addition would be the dominant pathway for changes in resonant frequency. Even with overestimated stiffnesses (~10 GPa), the mass effect would still be larger, and negative frequency shifts would be observed for uniform binding while the amplitude of the shifts would be reduced by roughly 50%.

One possible exception to this would be resonant biosensors for the detection of bacteria or large objects on a thin cantilever, which could significantly change the flexural rigidity through *I* more so than *E*. For prismatic cantilevers, *I* is given by $wt^3/12$, so the added thickness of a bacterial cell could have a significant impact on the flexural rigidity even if its stiffness is negligible compared to that of the resonator. Recent work has shown that inkjet-deposited droplets of bacteria at different places along a cantilever can result in positive or negative frequency shifts as well.[32] The authors also point out poor reproducibility in measuring the frequency shift associated with dipping the cantilevers in a particular concentration of bacteria. While a portion of this variability is likely due to the method of nonspecific bacterial binding to the cantilever, the competition between flexural rigidity and mass-loading effects is surely another factor, especially if the magnitudes of the frequency shifts are comparable.

However, for the majority of resonant biosensor experiments, uniform coatings should be used for detection, and very thin devices should be used as long as they are roughly an order of magnitude thicker than the expected biological materials to be captured and detected.

4.5.3 The High Sensitivity Limit and Dilute Analyte Binding

In the high sensitivity limit, very little material is added to devices, incomplete films are likely even when uniform binding is possible, and it is plausible that only a small number of binding events occur spread sparsely over the device. Sensing in this regime is limited to resonant sensors, as current research suggests that static deflection-based cantilever sensors require a percolated network of binding events in order to create even the tiniest surface stress that may or may not even be measurable.[52] In such cases device geometry becomes an important factor determining sensitivity and reproducibility. Here, restricting binding to a localized area will likely be detrimental to the sensitivity and limit the number of analytes binding to the sensor. The uniformity of the frequency response as a function of binding position has a significant impact on sensitivity as well as the reproducibility due to the presence of few randomly distributed binding events on each device. The frequency response of cantilevers to a bound analyte is a strong function of binding position along the length and is especially non-uniform if the analyte also affects flexural rigidity. Paddlevers improve the uniformity somewhat by creating additional binding area in the most sensitive region of the device and providing a larger fraction of sensor area that is sensitive to the mass of bound analyte. However, the variation along the length of the paddlever is still present. Here, the trampoline geometry should out-perform both of these geometries, due to the uniformity of the frequency response across the center paddle which makes up the majority of the device surface. The small support arms also reduce the amount of sensor area that is sensitive to changes in flexural rigidity and insensitive to mass.

In situations where a few binding events are expected to occur randomly on each device, devices with the most uniform frequency response as a function of

binding location and the largest proportion of surface area sensitive to binding are likely to perform the best. While smaller device geometries have lower masses and higher sensitivities, they also have smaller surface areas that will capture fewer analytes than larger devices of the same thickness. Even if devices with equivalent density, thickness, and surface area are compared, frequency responses will still vary due to differences in resonant mode shape. For a particular incidence rate of analytes on sensors based on concentrations as well as diffusion and mass transport, another important issue for small scale sensors,[53] the most sensitive devices will have the highest probability for binding events to take place on sensitive areas of the device. The most significant benefit of devices with the highest uniformity of frequency response is likely to be reduction in variations from device to device due to the randomness of analyte binding positions. It is here in this regime that trampoline-like devices outperform cantilevers with more uniform signals from resonator arrays and enhanced probability of analyte capture in the sensitive area(s) of the device.

REFERENCES

1. P.S. Waggoner and H.G. Craighead, "The relationship between material properties, device design, and the sensitivity of resonant mechanical sensors," *J. Appl. Phys.* **105** (2009) 054306.

2. P.S. Waggoner, C.P. Tan, L. Bellan, and H.G. Craighead, "High-*Q*, in-plane modes of nanomechanical resonators operated in air," *J. Appl. Phys.* **105** (2009) 094315.

3. M. J. Lachut and J. E. Sader, "Effect of Surface Stress on the Stiffness of Cantilever Plates," *Phys. Rev. Lett.* **99** (2007) 206102.

4. M. J. Lachut and J. E. Sader, "Effect of surface stress on the stiffness of cantilever plates: Influence of cantilever geometry," *Appl. Phys. Lett.* **95** (2009) 193505.

5. W. Weaver, Jr., S. P. Timoshenko, and D. H. Young, *Vibration Problems in Engineering*, 5th ed., Wiley-Interscience, New York, 1990.

6. S. S. Verbridge, D. F. Shapiro, H. G. Craighead, and J. M. Parpia, "Macroscopic tuning of nanomechanics: Substrate bending for reversible control of frequency and quality factor of nanostring resonators," *Nano Lett.* **7**(6) (2007) 1728.

7. S. S. Verbridge, H. G. Craighead, and J. M. Parpia, "A megahertz nanomechanical resonator with room temperature quality factor over a million," *Appl. Phys. Lett.* **92** (2008) 013112.

8. K. L. Ekinci, Y. T. Yang, and M. L. Roukes, "Ultimate limits to inertial mass sensing based upon nanoelectromechanical systems," *J. Appl. Phys*. **95**(5) (2004) 2682-2689.

9. K. Y. Yasamura, T. D. Stowe, E. M. Chow, T. Pfafman, T. W. Kenny, B. C. Stipe, and D. Rugar, "Quality factors in micron- and submicron-thick cantilevers," *J. Micromech. Syst.* **9** (2000) 117.

10. S. S. Verbridge, R. Ilic, H. G. Craighead, and J. M. Parpia, "Size and frequency dependent gas damping of nanomechanical resonators," *Appl. Phys. Lett.* **93** (2008) 013101.

11. Y. Wang, J. A. Henry, A. T. Zehnder, and M. A. Hines, "Surface chemical control of mechanical energy losses in micromachined silicon structures," *J. Phys. Chem. B* **107** (2003) 14270-14277.

12. J. A. Henry, Y. Wang, and M. A. Hines, "Controlling energy dissipation and stability of micromechanical silicon resonators with self-assembled monolayers," *Appl. Phys. Lett.* **84**(10) (2004) 1765.

13. J. A. Henry, Y. Wang, D. Sengupta, and M. A. Hines, "Understanding the effects of surface chemistry on *Q*: Mechanical energy dissipation in alkyl-terminated (C_1-C_{18}) micromechanical silicon resonators," *J. Phys. Chem. B* **111** (2007) 88-94.

14. A. M. Richter, D. Sengupta, and M. A. Hines, "Effect of surface chemistry on mechanical energy dissipation: Silicon oxidation does not inherently decrease the quality factor," *J. Phys. Chem. C* **112** (2008) 1473-1478.

15. L. Sekaric, D. W. Carr, S. Evoy, J. M. Parpia and H. G. Craighead, "Nanomechanical resonant structures in silicon nitride: fabrication, operation and dissipation issues," *Sens. Actuators A* **101** (2002) 215.

16. R. Sandberg, K. Mølhave, A. Boisen, and W. Svendsen, "Effect of gold coating on the *Q*-factor of a resonant cnatilever," *J. Micromech. Microeng*. **15** (2005) 2249-2253.

17. J. W. M. Chon, P. Mulvaney, and J. E. Sader, "Experimental validation of theoretical models for the frequency response of atomic force microscope cantilever beams immersed in fluids," *J. Appl. Phys.* **87**(8) (2000) 3978.

18. C. Vančura, J. Lichtenberg, A. Hierlemann, and F. Josse, "Characterization of magnetically actuated resonant cantilevers in viscous fluids," *Appl. Phys. Lett.* **87** (2005) 162510.

19. D. Ramos, J. Tamayo, J. Mertens, and M. Calleja, "Photothermal excitation of microcantilevers in liquids," *J. Appl. Phys.* **99** (2006) 124904.

20. S. S. Verbridge, L. M. Bellan, J. M. Parpia, and H. G. Craighead, "Optically driven resonance of nanoscale flexural oscillators in liquid," *Nano Lett.* **6**(9) (2006) 2109.

21. T. Y. Kwon, K. Eom, J. H. Park, D. S. Yoon, and T. S. Kim, "*In situ* real-time monitoring of biomolecular interactions based on resonating microcantilevers immersed in a viscous fluid," *Appl. Phys. Lett.* **90** (2007) 223903.

22. S. Basak, A. Raman, and S. V. Garimella, "Hydrodynamic loading of microcantilevers vibrating in viscous fluids," *J. Appl. Phys*. **99** (2006) 114906.

23. D. R. Southworth, H. G. Craighead, and J. M. Parpia, "Pressure dependent resonant frequency of micromechanical drumhead resonators," *Appl. Phys. Lett.* **94** (2009) 213506.

24. S. Timoshenko, *Strength of Materials*, Lancaster Press, New York, 2nd Ed., 1940, p 216-218.

25. R. Chau, S. Datta, M. Doczy, B. Doyle, J. Kavalieros, and M. Metz, "High-κ/Metal–Gate Stack and Its MOSFET Characteristics," *IEEE Electron Device Letters* **25**(6) (2004) 408.

26. S. Natarajan *et al.*, "A 32nm logic technology featuring 2nd-generation high-k + metal-gate transistors, enhanced channel strain and 0.171μm^2 SRAM cell size in a 291Mb array," *International Electron Devices Meeting*, IEEE, 15-17 Dec. 2008, 1-3.

27. R. K. Puurunen, "Surface chemistry of atomic layer deposition: A case study for the trimethylaluminum/water process," *J. Appl. Phys.* **97** (2005) 121301.

28. S. Dohn, R. Sandberg, W. Svendsen, and A. Boisen, "Enhanced functionality of cantilever based mass sensors using higher modes," *Appl. Phys. Lett.* **86** (2005) 233501.

29. B. Ilic, D. Czaplewski, M. Zalalutdinov, H. G. Craighead, P. Neuzil, C. Campagnolo, and C. Batt, "Single cell detection with micromechanical oscillators," *J. Vac. Sci. Technol. B* **19** (2001) 2825.

30. A. Gupta, D. Akin, and R. Bashir, "Single virus particle mass detection using microresonators with nanoscale thickness," *Appl. Phys. Lett.* **84** (2004) 1976.

31. B. Ilic, Y. Yang, K. Aubin, R. Reichenbach, S. Krylov, and H. G. Craighead, "Enumeration of DNA Molecules Bound to a Nanomechanical Oscillator," *Nano Lett*. **5**(5) (2005) 925-929.

32. D. Ramos, J. Tamayo, J. Mertens, M. Calleja, and A. Zaballos, "Origin of the response of nanomechanical resonators to bacteria adsorption," *J. Appl. Phys.* **100** (2006) 106105.

33. N. Lobontiu, *Dynamics of Microelectromechanical Systems,* Springer, New York, 2007.

34. C. A. Neugebauer, "Tensile Properties of Thin, Evaporated Gold Films," *J. Appl. Phys.* **31** (1960) 1096.

35. S. Schmid, M. Wendlandt, D. Junker, and C. Hierold, "Nonconductive polymer microresonators actuated by the Kelvin polarization force," *Appl. Phys. Lett.* **89** (2006) 163506.

36. L. B. Sharos, A. Raman, S. Crittenden, and R. Reifenberger, "Enhanced mass sensing using torsional and lateral resonances in microcantilevers," *Appl. Phys. Lett.* **84** (2004) 4638.

37. M. K. Ghatkesar, T. Braun, V. Barwich, J.-P. Ramseyer, C. Gerber, M. Hegner, and H. P. Lang, "Resonating modes of vibrating microcantilevers in liquid," *Appl. Phys. Lett.* **92** (2008) 043106.

38. Dufour, S. M. Heinrich, and F. Josse, "Theoretical Analysis of Strong-Axis Bending Mode Vibrations for Resonant Microcantilever (Bio)Chemical Sensors in Gas or Liquid Phase," *J. Microelectromech. Syst.* **16**(1) (2007) 44.

39. D. Jin, X. Li, J. Liu, G. Zuo, Y. Wang, M. Liu, and H. Yu, "High-mode resonant piezoresistive cantilever sensors for tens-femtogram resoluble mass sensing in air," *J. Micromech. Microeng.* **16** (2006) 1017.

40. T. Braun, V. Barwich, M. K. Ghatkesar, A. H. Bredekamp, C. Gerber, M. Hegner, and H. P. Lang, "Micromechanical mass sensors for biomolecular detection in a physiological environment," *Phys. Rev. E* **72** (2005) 031907.

41. T. Braun, M. K. Ghatkesar, N. Backmann, W. Grange, P. Boulanger, L.Letellier, H.-P. Lang, A. Bietsch, C. Gerber, and M. Hegner, "Quantitative time-resolved measurement of membrane protein-ligand interactions using microcantilever array sensors," *Nature Nanotechnol.* **4** (2008) 179.

42. E. Sader, "Frequency response of cantilever beams immersed in viscous fluids with applications to the atomic force microscope," *J. Appl. Phys.* **84** (1998) 64.

43. P. G. Datskos, N. V. Lavrik, and M. J. Sepaniak, "Detection of Explosive Compounds with the Use of Microcantilevers with Nanoporous Coatings," *Sens. Lett.* **1**(1) (2003) 25.

44. T. D. Rossing and N. H. Fletcher, *Principles of Vibration and Sound*, 2nd Ed., Springer, New York, 1999, p. 81.

45. S. Bunch, A. M. van der Zande, S. S. Verbridge, I. W. Frank, D. M. Tanenbaum, J. M. Parpia, H. G. Craighead, and P. L. McEuen, "Electromechanical Resonators from Graphene Sheets," *Science* **315** (2007) 490.

46. Jensen, K. Kim, and A. Zettl, "An atomic-resolution nanomechanical mass sensor," *Nat. Nanotechnol.* **3** (2008) 533.

47. J. Tamayo, D. Ramos, J. Mertens, and M. Calleja, "Effect of the adsorbate stiffness on the resonance response of microcantilever sensors," *Appl. Phys. Lett.* **89** (2006) 224104.

48. A. R. Burns, J. E. Houston, R. W. Carpick, and T. A. Michalske, "Molecular Level Friction as Revealed with a Novel Scanning Probe," *Langmuir* **15** (1999) 2922.

49. H. Suda, Y. C. Sasaki, N. Oishi, N. Hiraoka, and K. Sutoh, "Elasticity of Mutant Myosin Subfragment-1 Arranged on a Functional Silver Surface," *Biochem. Biophys. Res. Commun.* **261** (1999) 276.

50. Ch. Kargel, B. Trummer, G. Plevnik, C. Pellot-Barakat, J. J. Mai, and M. F. Insana, “Is Ultrasonic Imaging a Sensitive Indicator of Spatially Varying Elastic Anisotropy?,” *IEEE Ultrason. Symp.* **2** (2001) 1659.

51. Radmacher, M. Fritz, C. M. Kacher, J. P. Cleveland, and P. K. Hansma, “Measuring the Viscoelastic Properties of Human Platelets with the Atomic Force Microscope,” *Biophys. J.* **70** (1996) 556.

52. J. W. Ndieyira, M. Watari, A. D. Barrera, D. Zhou, M. Vogtli, M. Batchelor, M. A. Cooper, T. Strunz, M. A. Horton, C. Abell, T. Rayment, G. Aeppli and R. A. McKendry, “Nanomechanical detection of antibiotic-mucopeptide binding in a model for superbug drug resistance,” *Nat. Nanotechnol.* **3** (2008) 691–696.

53. T. M. Squires, R. J. Messinger, and S. R. Manalis, “Making it stick: convection, reaction and diffusion in surface-based biosensors,” *Nat. Biotechnol.* **26** (2008) 417.

CHAPTER 5

RESONANT BIOSENSOR APPLICATIONS*

Biosensing represents an up-and-coming field where resonant MEMS and NEMS sensors can be applied and have the potential to make a significant impact. Moving forward with the knowledge of how these sensors function from the previous chapter, paddlever and trampoline sensor geometries have been fabricated and used in various biosensor configurations. In addition, informed decisions can be made on device functionalization, proceeding with uniform bilateral functionalization for the capture of biological analytes with the expectation that stiffness will not play a role in sensing. Despite the efforts made in order to drive the mass sensitivity of resonant MEMS and NEMS sensors to the single Dalton level, the noise mechanisms that are relevant in such pursuits are typically washed out by non-specific binding and the noise it presents in random binding to all surfaces. Chemical specificity and associated non-specific binding of non-target compounds are the most significant limitations on sensing performance. Dealing with chemical processes compatible with the NEMS or MEMS devices is also important. In addition, another major problem that lies ahead is the fact that many biological analytes of interest are extremely light-weight, with masses on the order of zeptograms (10^{-21}) or attograms (10^{-18}).

In order to address this issue, a secondary mass labeling technique was developed that effectively adds mass to specifically captured analytes and greatly improves resonator sensitivity. This technique has been demonstrated for the detection of prion proteins[1,2] and prostate specific antigen[3] and is discussed below.

---

* This chapter highlights findings presented in full in three different publications. Section 5.5 discusses prion protein detection in buffer[1] and serum.[2] Section 5.6 highlights work by P.S. Waggoner *et al.*[3] for the detection of prostate specific antigen. Surface functionalization protocols used by all of these biosensing applications are discussed generally in Sections 5.2 and 5.3, while more detailed information can be gathered from the individual references.[1-3]

5.1 Current Surface Chemistries

The surface chemistries used in functionalization of MEMS and NEMS sensors give the devices their capability for sensing. Only when coated with receptor layers specific to a particular analyte can sensor signals be attributed to analyte detection. Mechanical biosensors use the same binding chemistries as conventional assay techniques. Immunoassays can be performed by coating devices with an antibody and detecting its antigen from solution, or vice versa. Tethering single-stranded DNA (ssDNA) to the cantilever can serve as a sensor for hybridization with the complementary strand of DNA.[4] Another method using enzymes has demonstrated glucose detection with glucose oxidase-coated cantilevers.[5] Liposomes have also been sensed, using capture layers that specifically bind to chemical groups on the liposome surface.[6] A newer technique of surface linking chemistry for MEMS and NEMS sensors uses aptamers, nucleic acids that behave like antibodies, for binding a specific compound.[7] A thorough review of molecular recognition and detection chemistries for biological sensors that are either in use or development has been presented by Iqbal *et al.*[8] Recently, cell membranes have been inkjet-printed on cantilevers in order to capture viruses seeking out particular membrane proteins, enabling the study of these proteins in a natural lipid bilayer setting.[9]

There is, however, a fair amount of complexity introduced by these linking chemistries. If special care is not taken, receptor molecules will nonspecifically adsorb on the sensor surface and potentially block specific binding sites on a portion of the molecules and in turn reduce device sensitivity. Neutron reflectivity experiments have shown that, without using linking chemistries, antibodies will adsorb flat onto SiO_2 surfaces, rather than the fully functional upright configuration, which degrades the antigen binding capacity of the antibodies.[10] Also, at sufficiently

high surface densities, conformational changes or steric hinderance effects from neighboring antibodies could reduce affinity for antigen binding.[11] Methods using amine reactive linkage to antibodies, for instance, may result in a random orientation of antibodies as they possess many addressable amine groups. In addition, tethering proteins to surfaces can detrimentally change their conformation or even denature them, depending on the type of link and where on the protein it is made.[12] Protein G has been used as a surface treatment that results in a more oriented attachment of antibodies. Other processes use the avidin-biotin linking chemistry, but that requires biotinylation of the receptor molecule. This process often results in attachment of several biotin molecules, subjecting the receptor layer to random attachment to the avidin-coated surface and therefore degradation of device sensitivity. These and other immobilization methods are quantitatively compared by Vijayendran and Leckband.[13] One common method of oriented immobilization uses receptor molecules that have been chemically modified with a thiol group that selectively binds to thin films of gold on the sensor. Another recent study has demonstrated improved biosensor sensitivity using antibodies linked to the surface by a ligand that is specifically attached to the antibody at the junction of the Fab and Fc regions.[14]

Single-chain Fv (scFv) or Fab antibody fragments offer potential solutions to many of these issues. By extracting the antigen-specific parts of the antibodies and using thiol groups to immobilize them on gold surfaces, the density of antigen binding sites is increased due to the smaller size of the fragments as well as their upright arrangement. This technique has led to significantly improved sensitivities for microcantilevers,[15] SPR,[16] and protein microarrays.[17]

Besides increasing the affinity of biosensor receptor molecules, there are other challenges in surface chemistry. Microcantilevers have been demonstrated as pH sensors using a variety of surfaces, including gold coated silicon and silicon nitride,

aminosilane monolayers, and thiol monolayers on gold.[18] While these are useful results, they also warn of background pH effects in all MEMS and NEMS biosensors since a majority of applications uses one of these surface chemistries in some form. Another daunting problem for biosensors is non-specific binding. This is often addressed by implementing a blocking chemistry. While many proteins or chemicals are used a blocking agents, such as bovine serum albumin, casein, or polyethylene glycol (PEG), it is not obvious which technique is most effective for particular surface chemistries. Careful planning of experimental procedure and using appropriate controls to measure a background for subtraction are often necessary to circumvent these effects and produce biosensors with meaningful results. Non-specific binding remains a significant limit on ultimate detection sensitivity.

5.2 Experimental Details of Surface Functionalization

With all these options available for use in the current work, careful consideration was given to all in choosing the one most appropriate for the sensor technology as well as the particular application. Techniques based on polymer or gold layers were strictly avoided if at all possible due to the commonly observed reduction in resonator quality factor upon deposition of these films. In addition, use of such (relatively) heavy materials on the devices would decrease the mass sensitivity of the resonators. As a result a silane-based, molecular monolayer technique, very common in glass slide functionalization for applications such as DNA microarrays, was used in order to present a surface of primary amine groups which would later be linked to specific capture molecules. Initially, the basic procedure common to all upcoming

applications will be discussed, but procedures and reagents that are unique to their particular application will be generalized or omitted for the time being.

After resonator chips are released in hydrofluoric acid, device surfaces are prepared for silanization in a two-step cleaning process that also improves bonding between the silane monolayer to the surface. Here, 3-aminopropyltriethoxysilane (APTES, Sigma, 99%) is used, which covalently links to hydroxyl (-OH) groups on the surface as well as neighboring APTES molecules through a series of reactions that depend on many different variables.[19] Because the typical resonator material used is low stress (silicon-rich) silicon nitride, some extra steps are used to encourage formation of hydroxyl groups on device surfaces. The chips were cleaned in a (2:1) piranha solution of sulfuric acid (H_2SO_4) : hydrogen peroxide (H_2O_2) for 30 minutes and then placed in an oxygen plasma cleaner for another 30 minutes. It is believed that these steps do alter the surface chemistry in preparation for surface functionalization, as significant decreases in resonator quality factor have been observed following these steps, which is consistent with previous observations of oxidized silicon resonators.[20,21] In addition, the initially hydrophobic chips become quite hydrophilic after these processes.

Afterwards, devices were functionalized with APTES overnight (~14-16 hours) using a 10% solution in dry toluene (Sigma, 99.8%) in a moisture-free environment. Too much water present can prohibit surface functionalization and encourage too much APTES hydrolysis and polymerization in solution.[19] Following silanization, the device chips were washed in a series of acetone, isopropanol, and water, and then soaked in DI water for 15 minutes on an orbital shaker in order to remove excess APTES and hydrolyze unreacted ethoxy groups.

All of the following biosensing applications that are discussed are protein-based and rely on antibody-based, or immunological, capture of the analytes. Because

all antibodies have several primary amine groups on its chemical structure, a homobifunctional linker molecule can be used to link together the amine groups on the antibodies with those present on the immobilized APTES. Therefore, surface modification continues by soaking chips in a 5% solution of gluteraldehyde (Sigma, 50%) in 10 mM borate buffer (pH ~8) for 2 hours, serving as a covalent cross-linker molecule between the amine groups. Following this and all subsequent steps, device chips are washed in purified DI water, however, the washing protocols varied slightly from application to application, and they will be discussed individually when appropriate. These washings are performed in water rather than buffer in order to prevent buffer salt crystals which form abundantly on the surface if buffer is allowed to dry on the devices, rendering the sensors effectively useless. Chips are dried off using a nitrogen stream prior to incubating with the next chemical.

After the capture antibodies are immobilized on the devices, chips are soaked in glycine buffer in order to quench any remaining, unreacted gluteraldehyde on the surface. Next the surfaces are blocked against non-specific binding by incubating the surface with bovine serum albumin. Device chips are then washed, dried, and placed in vacuum for frequency measurements. Afterwards, devices are incubated in the analyte sample solution for some amount of time, washed, and dried again before measuring resonant frequencies a second time in order to measure frequency shifts that can be attributed to some amount of bound analyte. No drastic loss of antibody functionality was noticed as a result of the drying process. Also, the multiple instances where additional material is added to device surfaces through aqueous processes and then dried greatly increase the probability of resonator stiction to the underlying substrate. Therefore, as discussed earlier, it is very important to ensure that devices are thick, short, and rigid enough and the sacrificial oxide layer is thick enough so that resonators do not irreversibly stick to the surface during surface

functionalization. Otherwise, a process like critical point drying would be required every time to prevent stiction, however, this would add a substantial amount of time to the processing, and the high temperatures and pressures used in addition to the presence of solvents would likely disturb or destroy surface functionality and antibody specificity.

5.3 Secondary Mass Labeling

The limits of MEMS and NEMS sensors are pushed by biomolecular sensing because of the very small masses typically involved. Take for instance a 60 kDa, or ~ 100 zg, molecule—in order to detect its presence in solution on a sensor with a minimum detectable mass of 10 fg, 10^5 molecules would need to bind to the surface, meaning that many, many more need to be present in solution. To make matters worse, key applications in medicine or the defense industry require sensors with high sensitivity to low concentrations of analytes in the presence of abundant non-specific molecules. In approaching these concentrations and lower, fewer and fewer molecules will be bound to surface-based sensors.

In order to overcome this, a technique termed secondary mass labeling has been developed, where additional specific molecules are used to tether high mass labels to analytes already captured on the surface. This is based on a process demonstrated for the detection of DNA hybridization where gold nanoparticle labels are used as seeds for silver enhancement, and the added mass of silver provides the utilized frequency shift signal used for detection.[22] In this case, an antibody-based sandwich assay is used in order to specifically add more mass to the devices. After the analytes are captured on the surface, a secondary antibody also specific to the analyte

is allowed to bind. Then, a nanoparticle label will bind to this secondary antibody, either through a biotin-streptavidin linkage or using antibody-coated nanoparticles which are specific for species of the secondary antibody. Such nanoparticles can easily have masses on the order of femtograms or more, which should improve sensitivity significantly, even if they only bind to a small percentage of analytes on the surface. In addition, the specificity of the assay is improved through the use of two analyte-specific antibodies.

The detection of nanoparticle labels is expected to only add mass and not significantly affect the flexural rigidity of the resonant sensor. Even though the nanoparticle diameter may easily be on the order of the resonator thickness, it is not directly in contact with the surface but is tethered through several layers of biochemistry, which may reduce any influence it may have on the stiffness. Also, the small size of each nanoparticle translates into a very small width ratio (cf. Figure 4-19) as well as a very small value for the integral in the numerator of Equation (4-40) because of the integration limits imposed by the "length" of the nanoparticle along the direction of the cantilever beam. In addition, the nature of the overhang in the present resonator geometry diminishes flexural rigidity effects, as shown in Figure 4-18. Another benefit of using nanoparticle labeling, is that frequency shifts due to nanoparticle binding can be crosschecked by observing devices in an SEM to count nanoparticles and estimate the added mass and associated frequency shifts.

5.4 Blocking Nonspecific Binding on Mass Sensors

For a large majority of currently used biosensors, the transduction mechanism is not mass. It is more often based on detecting fluorescent light from labels, or

measuring color change in assays using horseradish peroxidase in conjunction with a particular substrate that changes optically over time. In such applications, the amount of blocking agent used is not important as long as there is enough to properly block nonspecific binding. Even variations in blocking from sample to sample or day to day are not important as long as the nonspecific binding issues are kept at a constant minimum.

This mentality, however, does not work well with resonant mass sensors because they are sensitive to any and all mass added to devices—excessive blocking appears to be nonspecific binding just as much as nonspecifically bound analytes or reagents do. Therefore, there is essentially a "sweet spot" where there is sufficient blocking to limit nonspecific binding but not too much such that a great deal of it remains on the devices after washing. In addition, the effect of blocking on one device does not necessarily match those of the next one, or ones on a separate chip – it is a somewhat inexact science that depends on many variables pertaining to film quality, surface charge, or functionality that can vary on many length scales. This variability essentially restricts blocking steps from occurring between frequency measurements, otherwise experimental standard deviations will be out of control and wash out the signals.

Despite the discussions in Chapter 2 involving the cut-and-dry perspective of: "the frequency will shift up if the resonator becomes stiffer or it will shift down if mass is added," another possibility is that mass leaves the resonators. This has been observed for excessive blocking conditions, where washing protocols have been insufficient to remove all of the unnecessary blocking agents, which would then elute during the analyte incubation step and increase the resonant frequency, counteracting the addition of analyte mass to the sensors. Although after proper optimization, blocking times should be set in stone for a particular analyte for a particular protocol,

there will inevitably be variations day to day in surface functionalization or environmental conditions that will appear on all chips. In order to account for these background effects, controls are absolutely necessary in order to compare experiments from day to day and isolate the effect of and potentially quantify the specifically bound analyte or nanoparticle label through subtracting the control frequency shift from the shifts on all other chips that day.

5.5 Prion Protein Detection[1,2]

5.5.1 Background and Motivation

Prions proteins (PrP), discovered by Stanley Prusiner in 1982,[23] are proteins which in mis-folded form are believed to be responsible for causing progressive neurodegenerative diseases in numerous species, such as bovine spongiform encephalopathy (BSE) in cattle (also known as mad cow disease), scrapie in sheep, and Creutzfeldt-Jakob disease (CJD) in humans, among others.[24] These are fatal diseases, currently untreatable, and believed to be caused genetically, infectiously or even sporadically. While non-infectious, cellular PrP, or PrP^{c}, can easily be found in normal tissues of the nervous system, it can be converted into a misfolded conformation termed PrP^{sc} (sc for scrapie) that is infectious and believed to encourage more conversions of PrP^{c} to PrP^{sc}.

A key problem in distinguishing these two forms is that that their amino acid sequences are the same, and the secondary structure of the proteins become richer in β-sheet formations. This has, however, resulted in altered properties like insolubility or resistance to digestion by protease K. The digestion resistance has been used to

remove normal forms and attempt to isolate PrP^{sc} for detection.[25,26] Because neither the sensitivity of PrP^{c} nor the resistance of PrP^{sc} to digestion is absolute, the "protease-sensitivity assay" cannot definitively measure the presence or absence of PrP^{sc}.

Unfortunately, diagnosing these diseases is extremely difficult as they are often terminal once symptoms (typically neurological) arise. Therefore, the current state of technology to detect BSE relies upon the post-mortem detection of prions in homogenates of brain tissue removed from slaughtered cows. There are numerous methods available for the detection of prion proteins in animals, ranging from protein misfolding cyclic amplification to conformation-dependent immunoassay to dissociation enhanced lanthanide fluorescent immunoassays.[27] As most of these techniques are intended to detect PrP^{sc} in the brain homogenate, they are not appropriate for routine blood-based screening tests.

In addition, it has been shown that animals appearing normal or healthy could still carry the disease.[28,29] If these animals are not tested for PrP^{sc}, they could conceivably make their way into the human food supply. It is therefore imperative that new technologies be developed for the early detection of PrP^{sc} proteins. PrP^{sc} has been found in blood prior to the onset of clinical symptoms but at very low levels.[30-32] It is expected that the required sensitivity for presymptomatic detection of PrP^{sc} would be on the order of 0.1 pg/mL.[25] Besides high sensitivity, another important aspect of ante mortem testing would be the short detection time, so that all animals can be routinely screened prior to slaughter. Contraction of CJD in humans is not only attributed to the consumption of contaminated meat, but also to blood transfusions from an infected donor.[32,33] The lack of routine testing of cattle is further compounded by the lack of routine testing of human blood for transfusion, establishing a potentially dangerous scenario.[25,34,35]

Saa *et al*. developed a method to detect PrP^{sc} proteins in the blood of presymptomatic animals.[36] The number of PrP^{sc} proteins in the blood of infected hamsters was amplified by mixing them with normal brain homogenate and running protein misfolding cyclic amplification (PMCA) to convert PrP^{c} (in the normal brain homogenate) into PrP^{sc}. Seven rounds of 75 hour-long amplification cycles were performed in order to detect the low levels of prion proteins. The technique was sensitive to detect as low as 20–50 molecules of hamster PrP^{sc}, however, the time of cyclic amplification alone took 525 hours. Another technique based on flow cytometry demonstrated PrP^{sc} sensitivity on the order of 10 aM or 0.24 fg/mL in serum.[37] This process also required a long (20 hour) incubation time. While both of these methods are highly sensitive, neither are plausible or practical for rapidly screening herds of livestock.

In the following work, resonant micromechanical sensors are applied for the detection of PrP proteins. A sandwich immunoassay is performed on these resonators using a covalently linked chemistry based on surface silanization. In addition, secondary mass labeling is used to attach relatively large masses to antibodies already bound on the substrate. The sensitivity of these sensors is evaluated for PrP detection in both buffer and serum and are discussed as a potential platform for *ante mortem* testing of livestock as well as blood transfusion screening.

5.5.2 Experimental Details

Resonators are fabricated as described in Section 3.1 from low stress silicon nitride. Initial experiments performed in buffer used 200 μm thick paddlever devices with initial resonant frequencies of ~4.6 MHz, a length of 4 μm, and 10 μm wide by 3

μm long paddles, as shown in Figure 5-1. The holes are present in the paddle in order to facilitate the HF etching of the underlying sacrificial silicon dioxide. For later experiments performed in serum, the resonators used were of the same geometry but were 150 μm thick, which decreased initial frequencies to ~3.5 MHz. Device resonances were excited optically, using a modulated 405 nm diode laser and interrogated using optical interferometry; these techniques were described above in detail in Section 3.2.

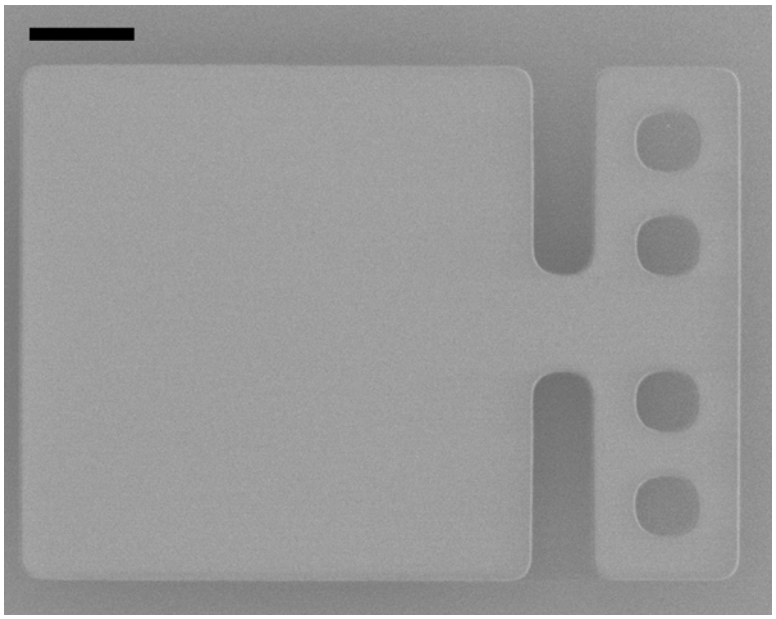

Figure 5-1. SEM micrograph of paddlever geometry used in the detection of PrP. Scale bar represents 2 μm.

Resonators are silanized as described in Section 5.2. The sandwich immunoassay used for PrP detection used primary monoclonal antibodies against amino acids 23−237 of bovine PrP (Millipore Inc.), recombinant prion protein (Millipore Inc.), and secondary monoclonal antibodies against amino acids 123−136 and 140−160 of bovine PrP (Abcam Inc., Cambridge, MA). Primary antibodies are

incubated on the amine-reactive device surfaces for 1 hour at 50 μg/mL in PBS buffer. Then, either buffer or deprionized fetal bovine serum (BioRad) is spiked with a concentration of PrP and incubated on chips for 1 hour. Controls are performed on chips where no PrP is spiked into PBS buffer or fetal bovine serum.

Secondary antibodies are then incubated on chips at 50 μg/mL for one hour. For detection in serum, the secondary antibodies are incubated slightly longer at 80 minutes. The secondary antibodies are conjugated with biotin using NHS−PEO_4-biotin (Pierce Chemicals) in order to present binding sites for the subsequently incubated streptavidin-coated nanoparticle mass labels. An EZ biotin quantification kit (Pierce Chemicals) was used to determine the degree of biotin labeling, which showed ~5-7 biotin molecules were present on each antibody. The secondary mass labels, streptavidin-conjugated nanoparticles (R&D Systems, Minneapolis, MN), are slightly diluted in the blocking solution (1% BSA in PBS buffer) and incubated for 30 minutes on the chips. Because the secondary antibodies had so many attached biotin molecules, it was not feasible to combine the secondary and nanoparticle incubation steps because they easily aggregate and essentially polymerize into large nanoparticle clusters linked by the biotinylated antibodies.

Washing steps are performed after each step in this protocol. For the detection of PrP in buffer, each washing step consists of an initial, gentle wash of each chip using DI water from a squirt bottle for 1 minute followed by a 2 minute long wash on an orbital shaker operated at 80 RPM. For the detection in serum, the washing protocol needs to be more rigorous, consisting of two separate orbital shaker washes at 95 RPM, each for 4 minutes. New water is used in the second washing step to assist in dilution of nonspecifically bound materials and remove eluted molecules.

The blocking protocols also slightly differed between the buffer and serum experiments. For both, the blocking solution consisted of 1% bovine serum albumin

(BSA) diluted in PBS buffer. A blocking step was performed prior to incubation of solutions spiked with PrP by 20 minutes in the case of the buffer and 30 minutes for detection in serum, where the time was increased in an effort to combat additional non-specific binding of the numerous proteins in fetal bovine serum. One more blocking step was performed prior to secondary antibody incubation for 10 minutes in both protocols.

Initially, the time for silanization was optimized by comparing the resonant frequency shifts due to nanoparticles from different chips with varying silaniztion times: 20 minutes, 80 minutes, and overnight (14-16 hours). The resulting frequency shifts of a control chip (no PrP) and 20 μg/mL PrP in buffer are shown in Figure 5-2. Error bars here and in all subsequent frequency shift plots correspond to the standard deviation of frequency shifts taken from roughly 20-24 devices per chip.

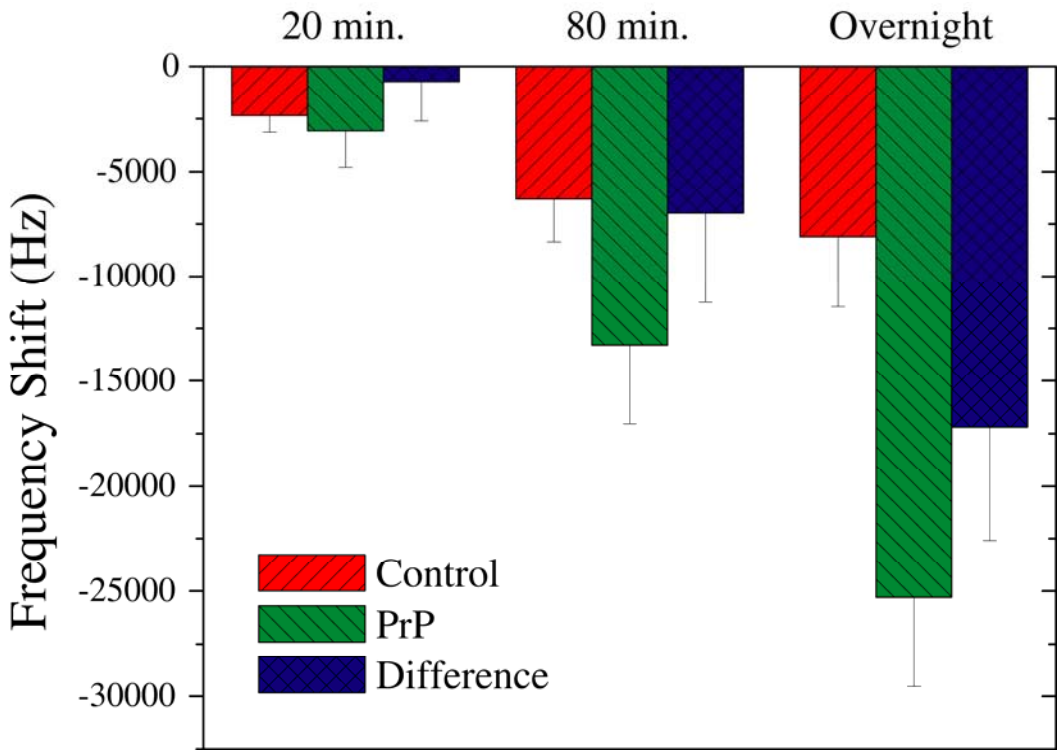

Figure 5-2. Plot showing how silanization efficiency improves with time using the frequency shift due to nanoparticle addition at the end of the labeled sandwich assay.

5.5.3 Prion Detection in Buffer

In order to study the amount of PrP that binds to resonators as well as the secondary antibody and nanoparticle labels, device resonant frequencies are measured just prior to the incubation step and immediately after the subsequent washing and drying. The control-subtracted frequency shifts corresponding to addition of PrP, secondary antibody, and nanoparticle label are shown as a function of PrP concentration in buffer in Figure 5-3 (a), (b), and (c), respectively. Because some of these experiments occurred on separate days, the control from each day must be subtracted from each of the frequency shifts that day in order to account for variations in surface chemistry, nonspecific binding, and environmental conditions that can vary from day to day. This also allows the frequency shifts to be associated only with the amount of specifically added material. For concentrations ranging from 20 ng/mL to 20 μg/mL, PrP can not be detected. However, upon addition of secondary antibody, a very small trend begins to appear, although the standard deviations make the concentrations statistically indistinguishable. However, addition of the streptavidin-coated nanoparticles made a significant different and enabled sensitivity down to concentrations of 2 ng/mL. The 200 pg/mL concentration could not be detected as its error bars overlapped with zero, signifying that it can not definitively be distinguished from the control.

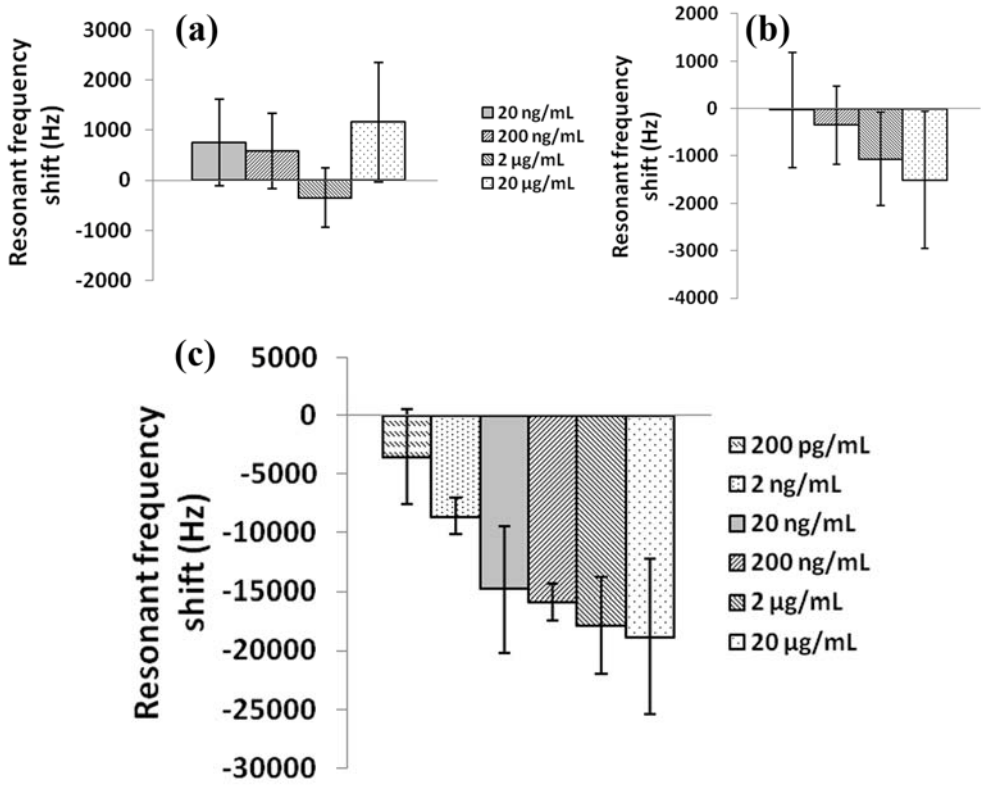

Figure 5-3. Resonant frequency shifts for the detection of PrP with (a) no mass labeling, (b) secondary antibodies, and (c) nanoparticle mass labels.

After taking the final resonant frequency measurements after nanoparticle binding, the chips are taken to a scanning electron microscope (SEM) and imaged. Because of the large size of the nanoparticles, they can be seen and even counted. Resonator images from chips incubated with several of the tested concentrations are shown in Figure 5-4, where there is a clear trend relating the PrP concentration to the number of nanoparticles observed on the device surfaces. In fact, nanoparticles are counted on several devices for each of these concentrations and used to estimate a total mass added to these devices. These values can be compared to the experimentally measured masses based on frequency shift calculations, using Equation (4-12) and assuming that the nanoparticles caused no changes in flexural rigidity. This also inherently assumes that the mass of the nanoparticles acts as an evenly

spread uniform film and is spread sufficiently evenly such that positional binding effects are not observed. The particle mass is estimated from a very rough average particle diameter of 150 nm and an density of 1.34 g/cm^3 which results in a particle mass of 2.4 fg, however, note that the particles are quite polydisperse.

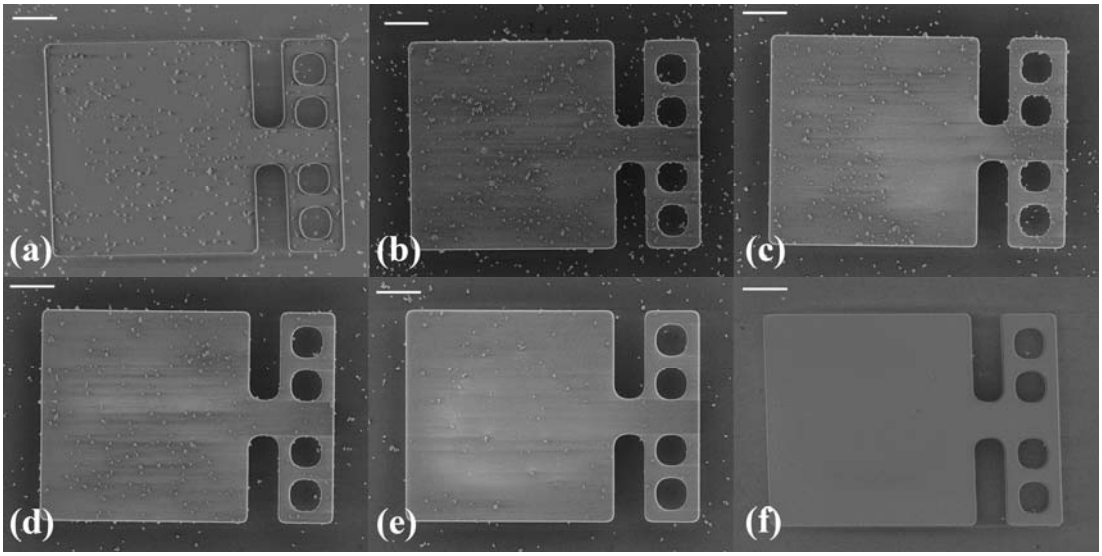

Figure 5-4. SEM images of paddlever resonators with nanoparticles attached following incubation with (a) 20 μg/mL, (b) 2 μg/mL, (c) 200 ng/mL, (d) 20 ng/mL, (e) 2 ng/mL, and (f) no PrP (control). All scale bars represent 2 μm.

Table 5-1. Nanoparticle Counting Results for Prion Detection

Concentration of PrP (ng/mL)	**Experimental Results**		**Calculated Results from Nanoparticle Counting**	
	$\Delta f/f$ x 10^3	**Mass (fg)**	**Particle No.**	**Mass (fg)**
20000	-7.51 ± 1.24	289 ± 48	126 ± 8	298 ± 19
2000	-7.15 ± 1.48	275 ± 57	120 ± 4	284 ± 10
200	-5.76 ± 1.68	222 ± 65	122 ± 6	289 ± 14
20	-5.07 ± 0.85	195 ± 33	100 ± 12	234 ± 28
2	-2.80 ± 0.76	108 ± 29	48 ± 6	114 ± 14
0.2	-1.90 ± 0.89	73 ± 34	36 ± 10	85 ± 28

The absolute frequency shifts are used (controls are not subtracted) in order to include both nonspecifically and specifically bound nanoparticles, which is what is observed in the SEM. A factor of two is included in the counted nanoparticles, as the underside of the paddlevers are functionalized for binding but can not be observed. This data is shown in Table 5-1, where it is shown that the two total masses are not significantly different ($P > 0.05$). As a result, both assumptions are confirmed: the nanoparticles do not affect resonator flexural rigidity, and there are too many nanoparticles bound in this case in order to observe effects related to dilutely bound nanoparticles.

5.5.4 PrP detection in serum

In order to test these resonant PrP sensors in a more realistic manner, the previous results were repeated but instead of spiking PrP into buffer it was put into fetal bovine serum. Other slight experimental changes were noted in Section 5.5.2. Absolute frequency shifts were measured for the binding of nanoparticles to resonators exposed to many different concentrations of PrP in serum and are shown in Figure 5-5. In addition, SEM images were taken on three of the resonator chips: the control, 200 pg/mL, and 20 ng/mL and are shown in Figure 5-6, again demonstrating the correlation between number of bound nanoparticles, the observed frequency shifts, and the amount of PrP in solution to which they were exposed. The first important feature of Figure 5-5 is that now 200 pg/mL can be detected in a more complex buffer – this slightly unexpected finding can be related to the improved washing used in this protocol as compared to that used in the buffer experiments. The all-orbital shaker washing is more rigorous and more repeatable, and its effects are apparent here in the

significantly smaller standard deviations here in comparison to those of Figure 5-3(c). This also signifies that the blocking protocol is sufficient in this case to prevent the serum from sterically reducing the amount of bound PrP and decreasing signals.

The reduced device thickness also plays a role, as it increases the sensitivity of the devices, effectively increasing the magnitude of the slope found in Figure 5-3(c). For instance, the frequency shift for 200 ng/mL there is around -15.5 kHz, where in Figure 5-5 that same concentration features a frequency shift signal of just over -20 kHz, even with the starting frequencies being lower for these 150 nm thick devices. If plotted using $\Delta f / f$, the slope would be a factor of 4/3 steeper due to the change in thickness.

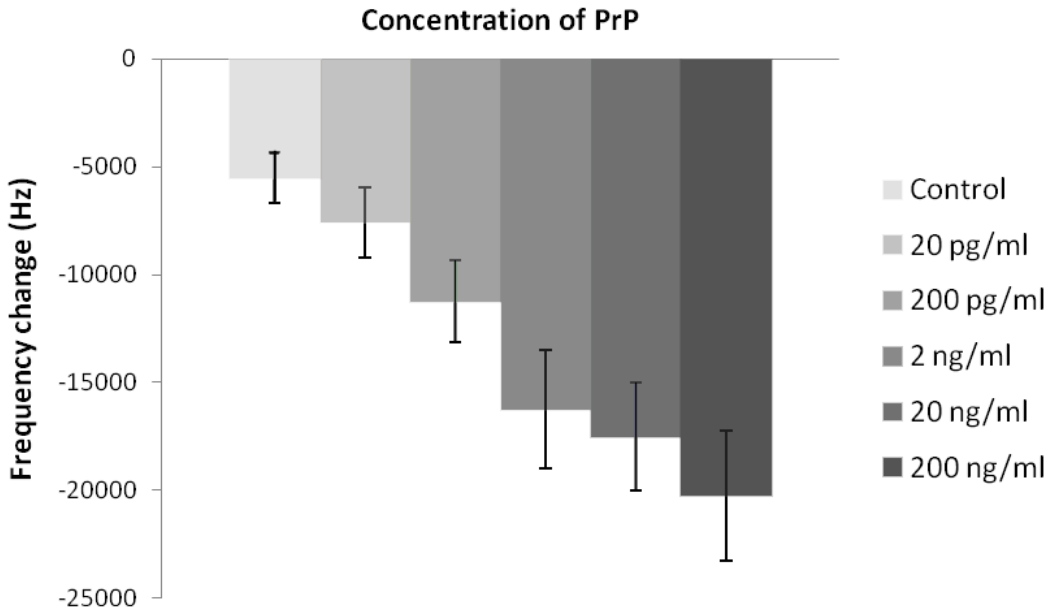

Figure 5-5. Frequency shifts measured for nanoparticle binding as a function of PrP concentration. The leftmost bar corresponds to the control, the next to 20 pg/mL, and up an order of magnitude in PrP concentration for each to the right.

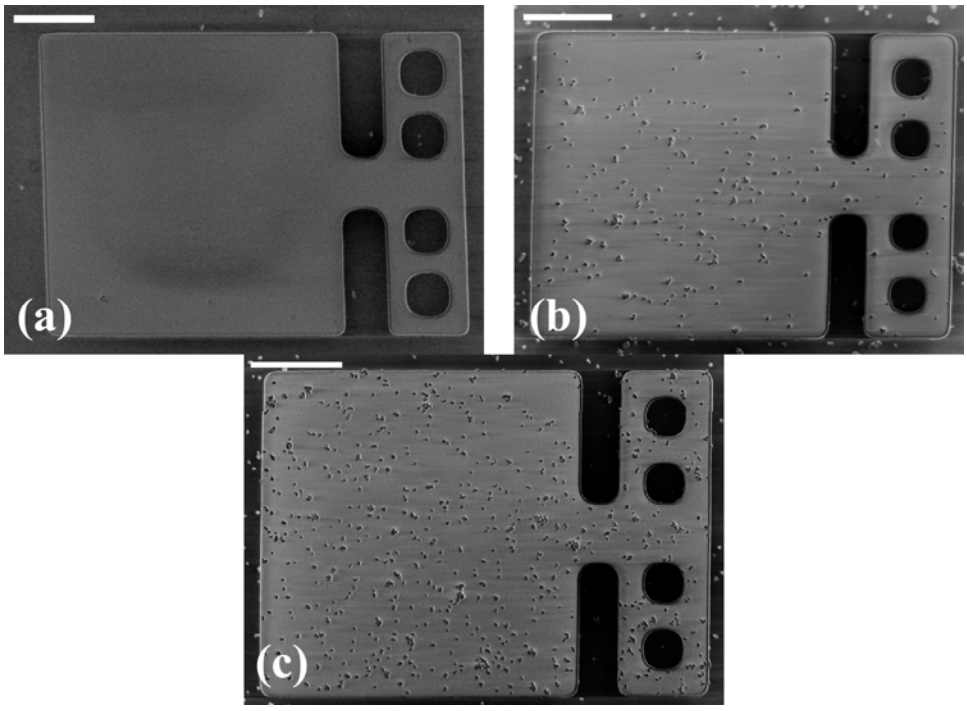

Figure 5-6. SEM images of resonators labeled with nanoparticles after being exposed to (a) no PrP (control chip—only fetal bovine serum) and to PrP concentrations of (b) 200 pg/mL and (c) 20 ng/mL.

5.6 Prostate specific antigen detection[3]

5.6.1 Background and motivation

Prostate specific antigen (PSA) is a clinically monitored protein used in screening tests for prostate cancer.[38] PSA is a normally produced protein found at a high concentration in seminal fluid. Elevated concentrations of PSA in the blood are associated with a higher risk for prostate cancer and may indicate damage of the prostate tissue, allowing PSA to escape into circulation.[39] While PSA can be found in its free form, it is more common for it to be complexed with enzymes or other

molecules, such as α1-chymotrypsin, α1-protease inhibitor, or α2-macroglobulin. At this time, sensitivity to total PSA (free and complexed) concentrations in the range of 2 to 10 ng/mL are required, as there is elevated risk for prostate cancer at these concentrations, while for free PSA the clinically relevant concentrations range from ~0.5 to 1.2 ng/mL (15-36 pM).[38]

When PSA is found at or above these concentrations, a biopsy is often required as the next step to assess whether the increased concentration is associated with prostate cancer or another condition such as benign prostate hyperplasia. However, many such biopsies are negative for cancer; it has been suggested that monitoring the percentage of free to complexed PSA may be more sensitive and also avoid unnecessary biopsies by helping to discern between benign and malignant conditions.[40] With improved sensitivity to PSA levels in serum, its concentration could be tracked over a long period of time at lower concentrations, and increased risk could be gauged from case to case by personal baselines and trends rather than approximate, age-based cut-off guidelines.

Several groups have used MEMS or NEMS sensors in order to detect PSA. Microcantilevers have been used in static deflection mode to detect the surface stress associated with PSA binding to an antibody-coated surface, demonstrating sensitivity to 0.2 ng/mL.[41] Similar devices were used in a two-dimensional array of sensors for PSA through surface-stress induced deflection, detecting 1 ng/mL.[42]

While predominantly used as mass sensors, some have suggested that dynamic, resonant MEMS or NEMS devices could also respond to surface stresses resulting from PSA binding. Hwang *et al.* reported PSA detection of 1 ng/mL using relatively large microcantilever resonators operated in liquid, stating that the frequency shifts arose from a combination of mass-loading effects and a compressive surface stress.[43] Recent work claims that PSA can be detected solely through frequency shifts due to

surface stress, down to a level of 10 pg/mL, or even down to 1 pg/mL if a secondary sandwich antibody is used.[44] However, the calculated surface stresses are much larger than previously reported; for instance, a PSA concentration of 1 ng/mL produced a compressive surface stress of ~40 mN/m, in constrast with the experiments discussed above,[41,42] where compressive surface stresses of approximately 4 and 2 mN/m were found, respectively. In addition, Lachut and Sader have questioned the validity axial-force models like that used in Reference [44] to relate surface stress to resonant frequency, stating that such models violate Newton's third law.[45]

For any biomolecular sensing platform, it is important that its sensitivity be assessed using realistic samples, such as blood serum, urine, or saliva, as sensors applied in the medical field would face these solutions every day. The primary issue that arises when working with serum rather than standard buffer solution is the non-specific binding of other background proteins or biomolecules to the sensor surface. This is typically assumed to sterically block specific binding sites and reduce the amount of captured analyte. In addition, non-specifically bound materials can alter the signals of both mass and surface stress sensors, potentially reducing or even exaggerating measured signals that should be associated with only specific interactions. One recent study using micromechanical resonators to detect PSA has tried to combat this with using prolonged washing after serum has been introduced to the devices, which appeared to remove a large part of the non-specifically bound material.[46] In serum, they observed signal reduction and a detection limit of 100 pg/mL, however, no explicit data from control measurements was shown, which is required to determine the effect of the background media on the sensors and the detection limit.

Prostate specific antigen has a small molecular weight of ~33 kDa or roughly 55 zg (10^{-21} g). At low concentrations, it is unlikely that the number of PSA bound to

resonators would have sufficient mass to produce a detectable frequency shift. However, PSA detection has been demonstrated in liquid at a concentration of 10 ng/mL using a mass-sensitive, resonant cantilever.[47] In order to overcome this, a secondary mass labeling technique is used in the present work, consisting of an antibody-based sandwich assay and nanoparticle mass labels to essentially amplify the mass of the bound PSA molecules. Arrays of trampoline resonators were functionalized with capture antibodies specific to PSA, and a second antibody was used to specifically tether nanoparticle mass labels to PSA molecules attached to the devices. These devices demonstrated PSA detection from undiluted serum at concentrations ranging from 50 ng/mL down to 50 fg/mL, or 1.5 fM.

5.6.2 Experimental details

Resonators used in this work are trampoline shaped, unlike the traditional cantilever geometry found ubiquitously in the literature; an SEM micrograph of the arrayed devices is shown in Figure 5-7(a). The trampoline center has a diameter of 6 μm, and the support arms are 1 μm wide. These flexible supports allow the center to move in and out of plane with fairly constant amplitude and help to concentrate the majority of the device sensing area in the region most sensitive to mass loading, the central paddle. This motion is depicted in Figure 5-7(b), showing the extent of trampoline displacement for the fundamental resonant mode, which is used in this work. In addition, the large surface area of these devices, ~ 54 μm^2, is significantly greater than that of the previously used 4 μm long paddlevers, ~ 30 μm^2, or cantilevers of the same length, ~8 μm^2, increasing the probability of capturing analytes at extremely low concentrations, which may improve sensitivity.

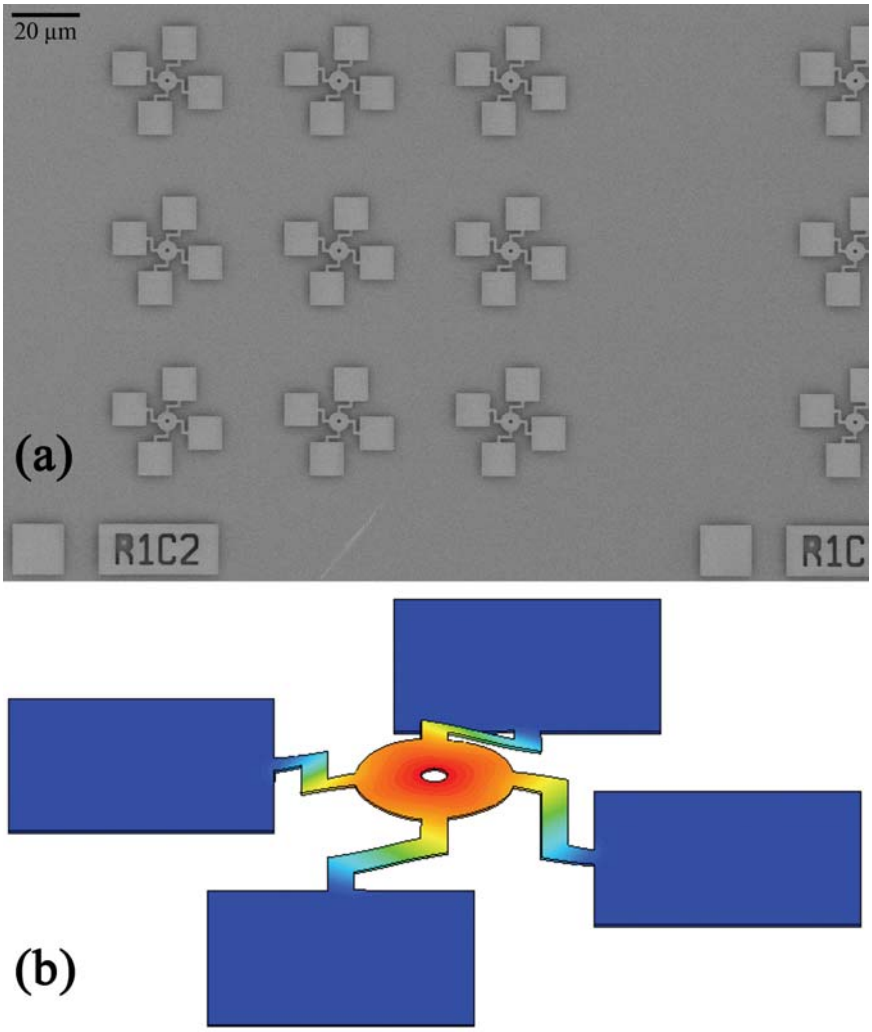

Figure 5-7. (a) SEM micrograph of 3x3 arrays of trampoline resonators with 50 µm between adjacent devices. The center area of each device measures 6 µm in diameter, with a 1 µm diameter hole at the center for etching purposes. (b) Image obtained using finite element analysis depicting the displacement of the device in the fundamental resonant mode.

In order to specifically capture PSA on resonators and detect their presence, a sandwich immunoassay is performed on device surfaces that would finally be used for secondary mass labeling. The assay consists of two antibodies, affinity-purified, polyclonal goat antibodies for human free PSA and monoclonal mouse antibodies to human free PSA, epitope 1, and human free PSA (>98% pure), all purchased from Meridian Life Science (Cincinnati, OH). In the washing step performed after each incubation in the protocol, device chips are washed twice in purified DI water on an orbital shaker operating at 95 RPM. Each washing step lasts for two minutes, and fresh water is used between washes. Three blocking steps are used in the protocol, occurring just before PSA, secondary antibody, and nanoparticle incubations. Each is performed for 15 minutes using a 1% solution of bovine serum albumin (BSA) in phosphate buffered saline (PBS) that had been filtered through a 0.2 μm pore filter.

Two assay configurations are tested in this work and each will be further discussed in the following section. For both versions, however, all antibodies are incubated with chips for one hour at concentrations of 50 μg/mL in PBS buffer. One assay centers on the use of biotinylated secondary antibodies, which are conjugated with biotin using NHS−PEO_4-biotin (Pierce Chemicals) for later use with streptavidin-coated nanoparticles. Free PSA is spiked into either PBS buffer or undiluted fetal bovine serum (FBS, HyClone, Thermo Scientific) at many different concentrations ranging from 50 fg/mL to 50 ng/mL and incubated on the devices for one hour. Control chips are incubated with buffer or FBS containing no PSA. All FBS is filtered through 0.2 μm filter prior to use. The two protocols featured the same nanoparticle (NP) but with different functional coatings. Magnetic nanoparticles, either coated with streptavidin or goat anti-mouse IgG antibodies (R&D Systems, Minneapolis, MN), are used to bind to the secondary mouse antibodies. The nanoparticles measure roughly 100-150 nm in diameter, and correspondingly have masses on the order of 1

fg. The nanoparticles are diluted by a factor of 1:50 in the 1% BSA blocking solution. Device chips are dried using a stream of nitrogen before loading in vacuum and measuring resonant frequencies before and after incubation with nanoparticles. The frequencies are measured using an external piezoelectric element and detected interferometrically, as described in Section 3.2.

5.6.3 Assay Development and Nonspecific Binding Studies

Initially, the biotin-streptavidin chemistry used for prion protein detection, as discussed in Section 5.5, was applied here. In this case, a polyclonal secondary antibody was used in an attempt to make devices more likely to capture secondary antibodies on the PSA, and in turn more likely to bind NPs, due to their ability to specifically bind to multiple epitopes on PSA. This chemistry is shown in Figure 5-8(a). However, when performed, the resulting frequency shifts due to nanoparticle addition were the same on all chips regardless of PSA concentration. Nanoparticles were ubiquitous on all device surfaces even when PSA was absent.

This sparked a series of qualitative diagnostic tests on unpatterned, low-stress silicon nitride surfaces in order to investigate the nonspecific binding and uncover its origins. The identical surface chemistry and procedures were repeated on these chips as described above. Figure 5-9 shows an SEM comparison of a control chip and one exposed to 50 ng/mL PSA, and again nonspecific binding appeared to be dominant.

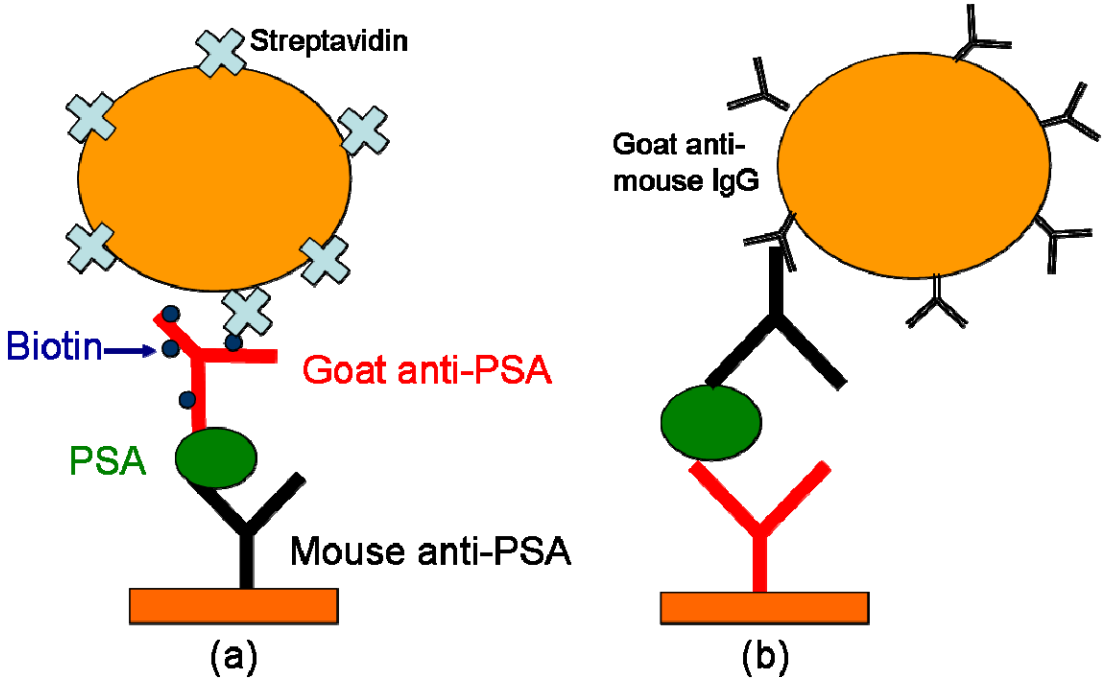

Figure 5-8. Schematic diagrams of the two sandwich assay protocols used for the detection of PSA through secondary mass labeling based on (a) the streptavidin-biotin linking chemistry or (b) the species-specific, antibody-based protocol.

In an effort to reduce nonspecific binding throughout the protocol a surfactant, Tween-20 (Sigma), was diluted in water at a concentration 0.05% and used in the first part of each washing step along the protocol. The second part of each washing step remained as pure DI water to make sure that no Tween-20 residues were left on the surface. SEM micrographs were again taken and two are shown in Figure 5-10. Unfortunately, both chips still featured equivalent amounts of nanoparticles that had nonspecifically bound. In addition, a rough comparison with the images in Figure 5-9 suggests that the Tween-20 had no effect at all in reducing the number of nanoparticles stuck to the surface.

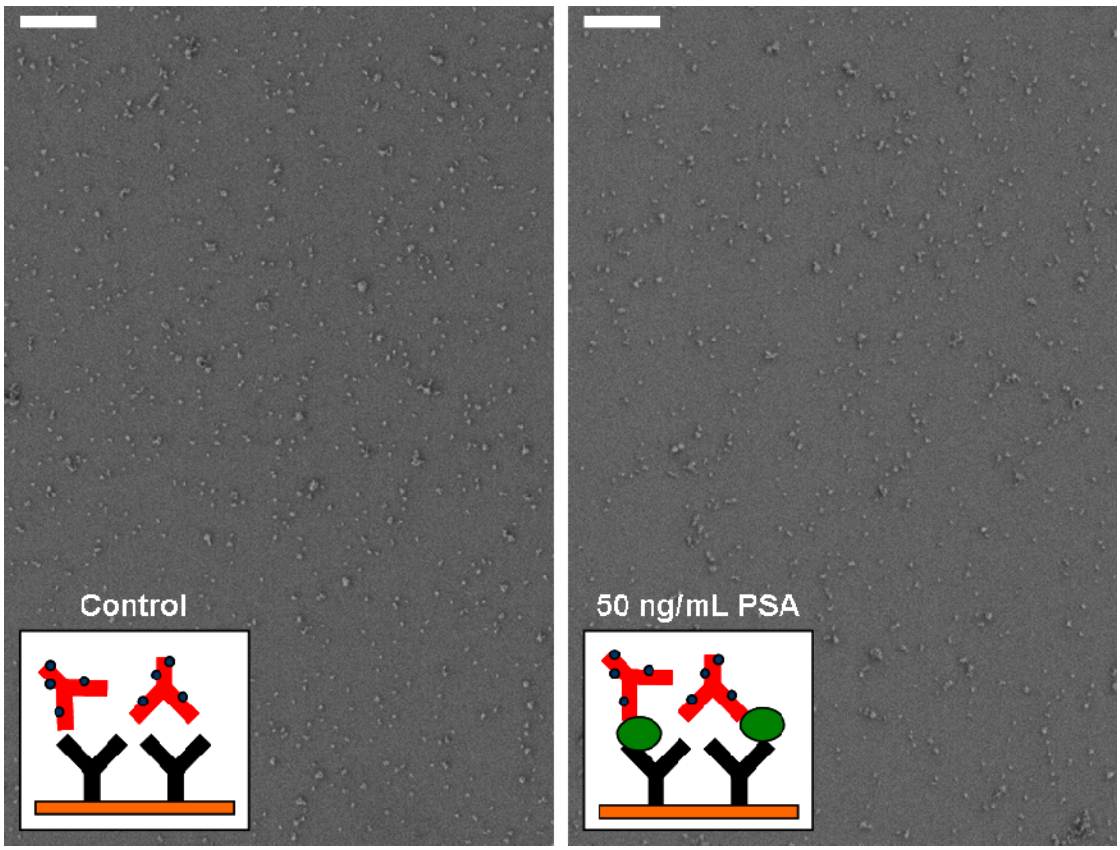

Figure 5-9. SEM images showing that nonspecific binding of streptavidin-coated NPs is a significant problem. Scale bars are 2 μm.

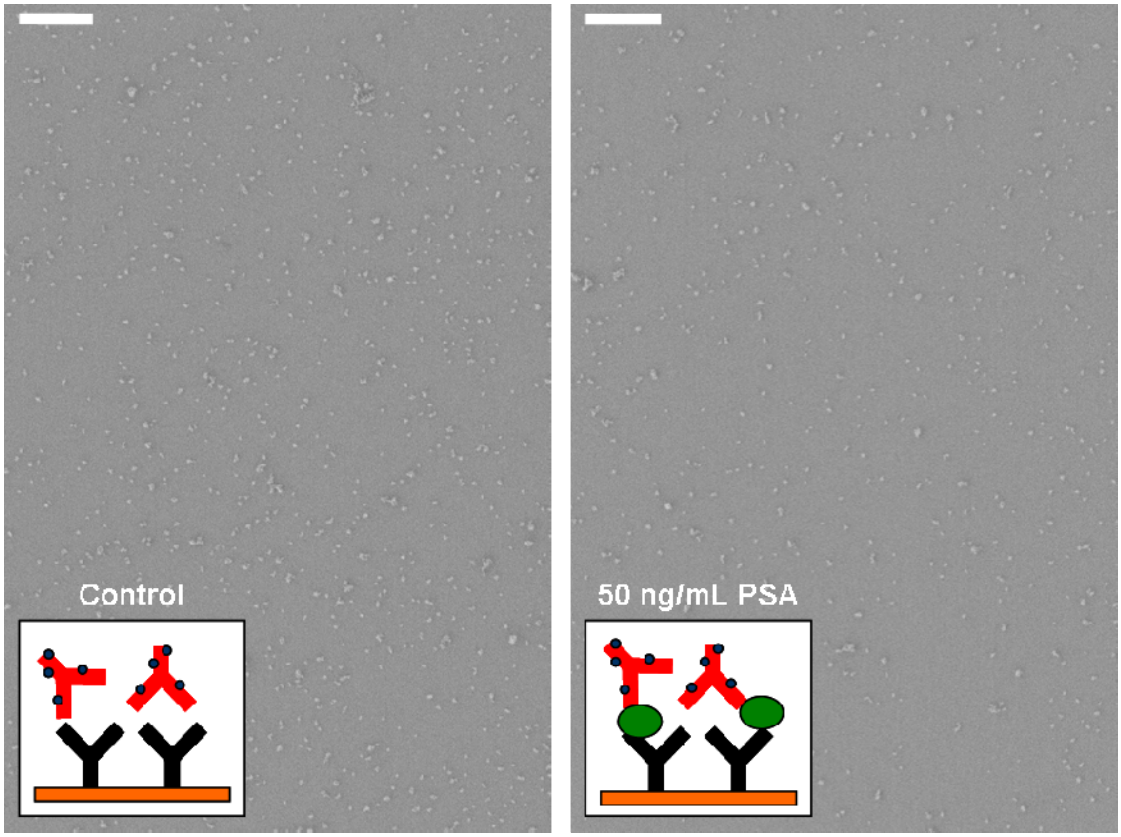

Figure 5-10. Test results from the addition of 0.05% Tween-20 to the first part of all washing steps, showing that it is ineffective at decreasing the amount of nonspecific binding.

Following the demonstrated inability of Tween-20 to reduce nonspecific binding, it was thought that the blocking chemistry was inappropriate for these reagents. As a result, two other commonly used blocking agents were prepared for use in the protocols. Chicken egg albumin and salmon plasma were both diluted to 1% in PBS buffer and filtered through a 0.2 μm filter, just as the BSA blocking solution was prepared. However, neither of these new blocking agents made a difference in the nonspecific binding (SEM images not shown).

The next step taken was to see how the nanoparticles responded to unlabeled antibodies. Secondary polyclonal antibodies were used here as received, with no biotin added. After incubation with the NPs, the chips were observed in an SEM. Representative images from the chips are shown in Figure 5-11, where very few nanoparticles are present in either situation. These observations essentially exonerate the nanoparticles—nonspecific binding must be happening at another level in the surface chemistry.

One possibility was that the secondary antibodies were nonspecifically binding due to some property of the polyclonal antibodies. Therefore, a second monoclonal antibody to PSA (epitope 3) was obtained (Meridian Life Science, Cincinnati, OH) and biotinylated in the same way as the polyclonal antibodies. These new antibodies were used in a full assay and again SEM images were taken after incubation with NPs. These results, shown in Figure 5-12, were essentially identical to those for the biotinylated polyclonal antibodies, the results of which are shown in Figure 5-9. Nanoparticles where still binding everywhere.

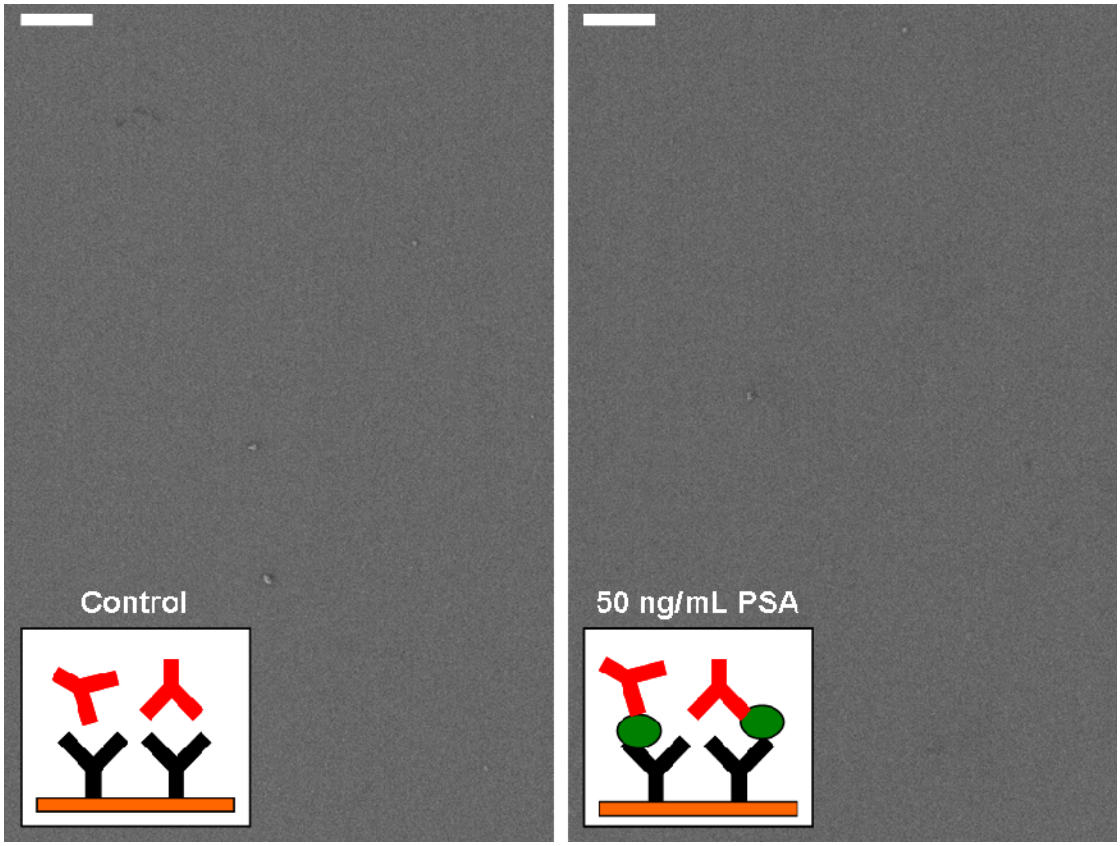

Figure 5-11. SEM comparison of chips with and without PSA using unlabeled secondary antibodies, where very few nanoparticles bound to the surface. Scale bars are 2 μm.

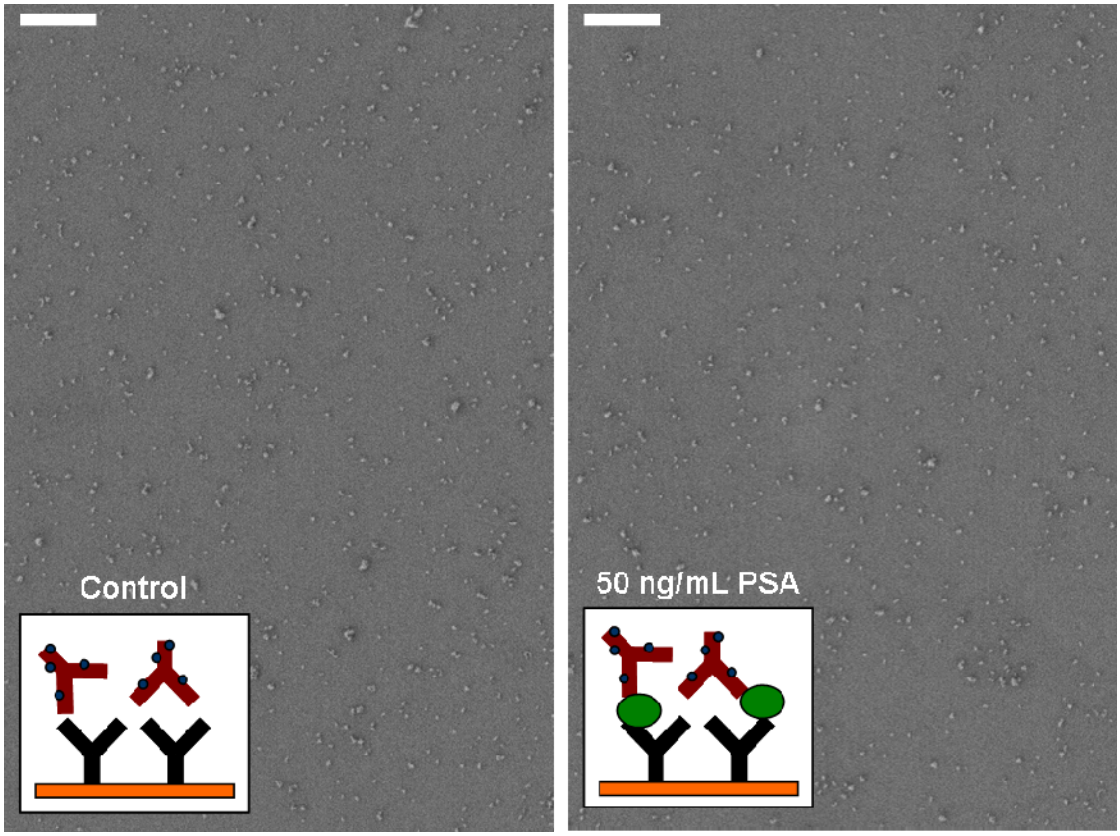

Figure 5-12. SEM images from sandwich assays using an alternate secondary antibody (monoclonal, specific to epitope 3) that was biotinylated in the same way as the initial ones, but with no reduction in nanoparticle binding. Scale bars are 2 μm.

At this point, it appeared that the biotinylation process somehow strongly encouraged the nonspecific binding of the labeled secondary antibodies to the surface. Only one question was left to answer: was there something wrong with the biotinylation process that introduced a huge background of free biotin to the chips that would then bind any and all nanoparticles that reach the surface? The labeled antibodies were dialyzed for very long periods of time (> 24 hours) in order to purify them from free biotin. To check if this were possible, a 1 mg/mL solution of biotin (~4.1 mM) was prepared in PBS buffer and incubated for an hour on the silicon nitride chips after PSA, and no secondary antibodies were used. SEM images, shown in Figure 5-13, revealed that very few nanoparticles bound to the chips, nowhere near the numbers shown in several of the previous figures.

It then became clear that an alternate surface chemistry should be used. If the sandwich assay were turned upside down, so to speak, then the streptavidin-coated nanoparticles could be replaced by ones functionalized with goat anti-mouse IgG antibodies. This is shown schematically in Figure 5-8(b). While this would not have been feasible with the prion protein assay in Section 5.2 since both primary and secondary antibodies were from mice, it is plausible in this case because only the secondary antibody (to which it should bind) is a mouse antibody. In addition to repeating the above tests with and without PSA present, another control was performed where only the new primary (goat) antibodies were present on device surfaces to ensure no cross-reactivity. These results are shown in Figure 5-14. After finding nearly no nanoparticles on the first control (no secondary antibody or PSA) and very few on the second (no PSA), there were many present on the PSA chip.

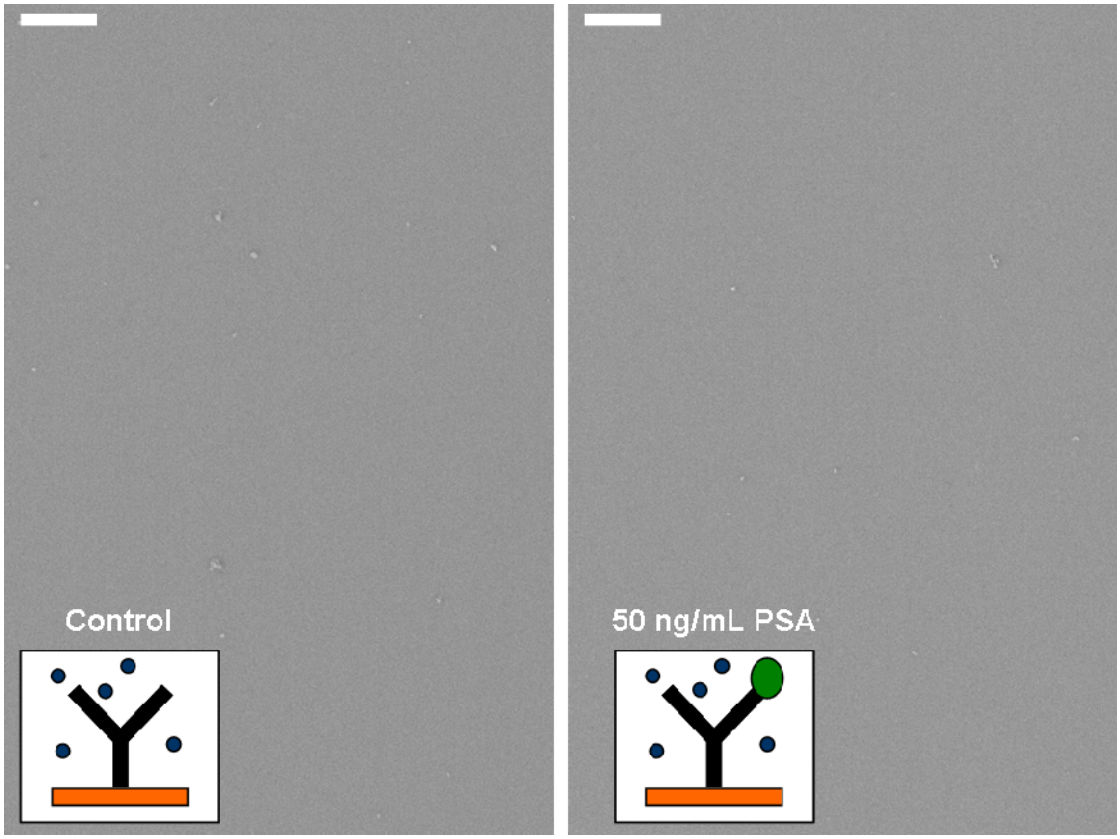

Figure 5-13. Representative SEM images from chips incubated with a high concentration (1 mg/mL) of free biotin, to simulate failed dialysis during biotinylation. However, very few nanoparticles bound to either chip. No secondary antibodies were used in this test. Scale bars are 2 μm.

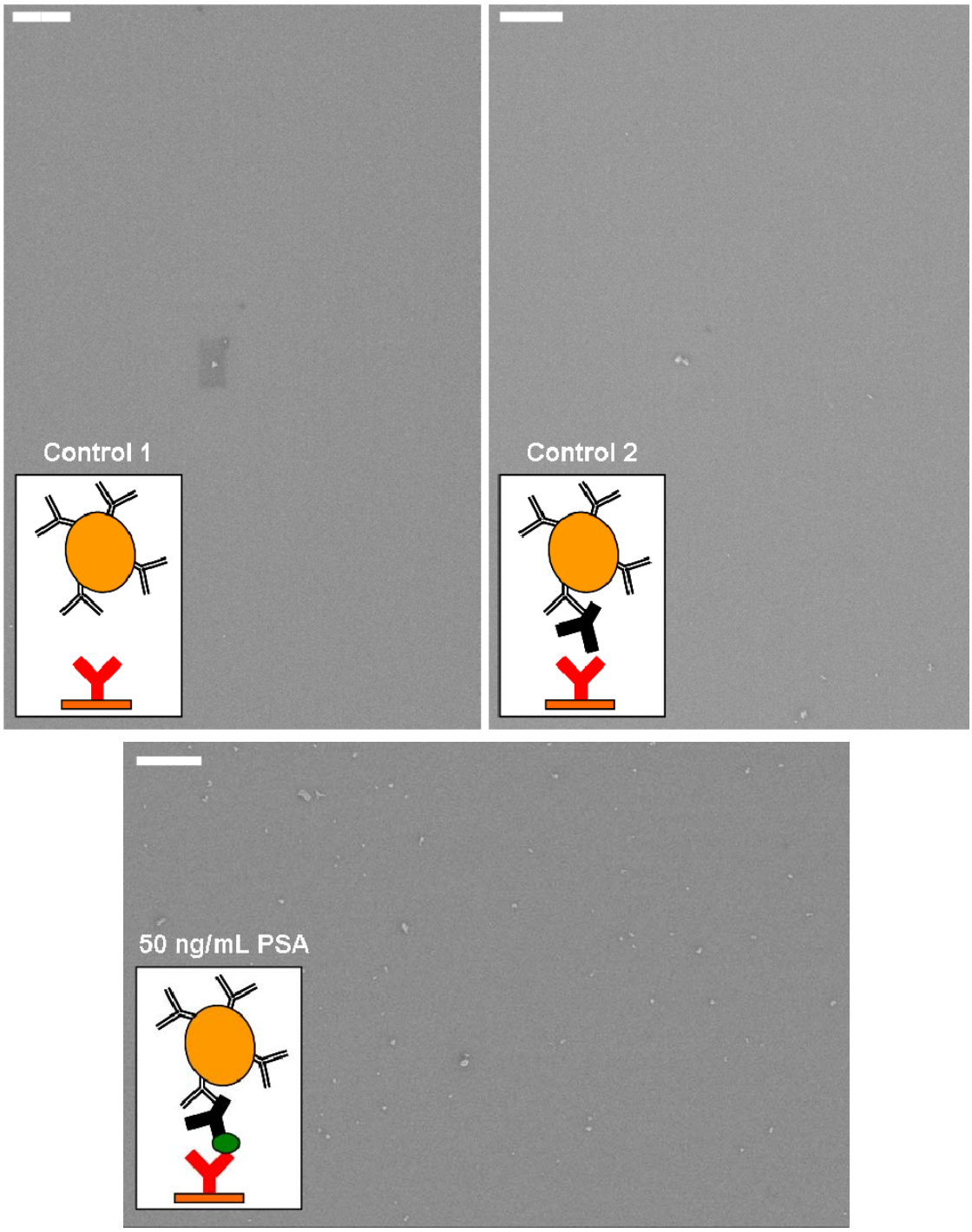

Figure 5-14. Experimental results from new protocol based on antibody-coated nanoparticles, including an addition control demonstrating no cross-reactivity between the capture antibodies and NPs. Scale bars are 2 μm.

5.6.4 Prostate Specific Antigen Detection in Serum

After resolving the issues of non-specific binding, the new sandwich assay was adopted for all further use. However, the biotin-streptavidin linking chemistry did have the benefit of being a fast and strong interaction, while antibody binding processes typically require longer times to specifically bind. As a result, the incubation time for nanoparticles was increased to 90 minutes from the 30 used previously. In order to assess the effect of fetal bovine serum on the assay, we tested the detection of 50 pg/mL PSA diluted in PBS and serum. For both media, a control chip was used with no spiked PSA present in order to determine the background effects of the buffer and serum. The results are shown in Figure 5-15, where only a small increase in background was observed for the chips exposed to FBS. This corresponded with a slightly decreased difference between control and sample, however, the two frequency responses were within error of each other. These results indicate that the blocking and washing procedures are effective and that the detection of PSA in the presence of serum does not strongly affect the frequency responses due to the binding of nanoparticle labels later in the assay protocol.

Additional PSA concentrations ranging from 50 ng/mL to 50 fg/mL were tested, and the frequency responses due to nanoparticle addition are shown in Figure 5-16. In order to compare the responses from experiments performed on different days, the control frequency shift was subtracted from all other shifts from that day in order to determine and compare the portions of the frequency shifts associated with mass specifically added to resonators. This differential shift takes into account the variations in environmental conditions, surface functionalization, and nonspecific binding from day to day. The control frequency responses typically ranged from 0 to -1 x 10^{-3}. This variability is attributed to changes in environmental conditions that

occur between the frequency readings. To illustrate, several controls from the above data are shown in the inset of Figure 5-16. The 50 fg/mL frequency shift was found to be significantly different from a null shift ($P < 0.0005$) using a one-tailed, student's t-test. Similarly, the frequency shifts for all concentrations were found to be significantly different from neighboring concentrations ($P < 0.001$).

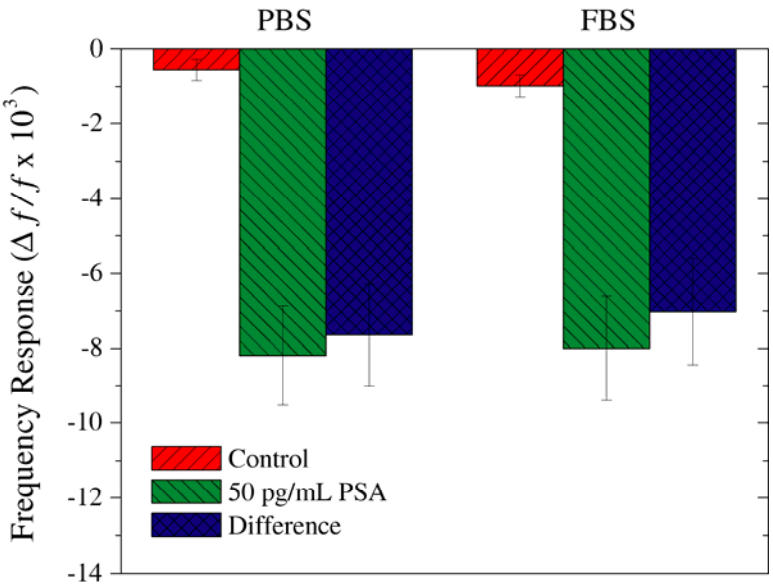

Figure 5-15. Comparison of resonant frequency responses in the detection of PSA at 50 pg/mL in PBS buffer and fetal bovine serum (FBS). While a small amount of non-specific binding is evident from the increased FBS control, the two differential signals are still within error of each other.

To illustrate nanoparticle binding, SEM micrographs were taken of the devices, and representative images at several concentrations are shown in Figure 5-17. For lower concentrations of PSA, fewer nanoparticles were bound to the resonators. Note that nanoparticles should also be bound to the bottom of the trampoline, as all device surfaces were functionalized. In this case, the assumption of mass addition as a uniform layer breaks down, and the nanoparticles behave essentially as point masses.

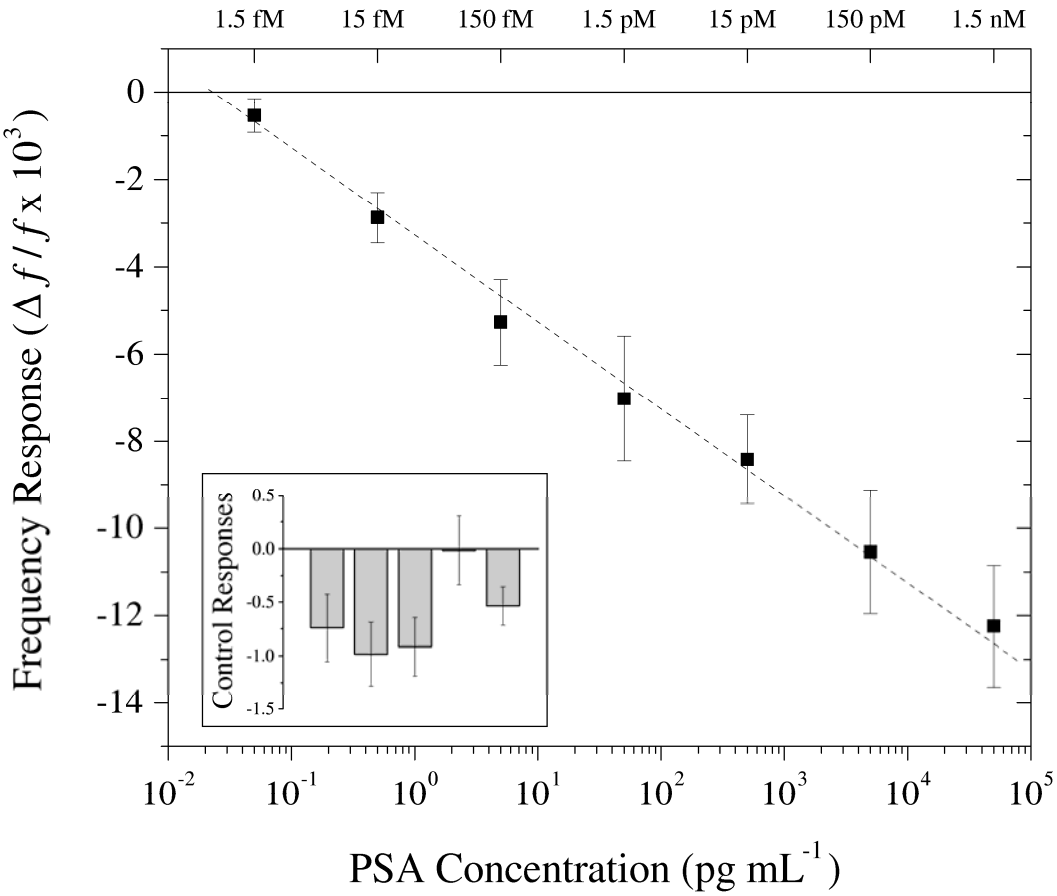

Figure 5-16. Frequency response of resonant sensors due to the addition of nanoparticles for different PSA concentrations, demonstrating a concentration sensitivity of 50 fg/mL. The inset shows control responses observed during the tests performed at different concentrations, demonstrating consistent but slightly varying background signals due to variations in non-specific binding and environmental conditions from day-to-day.

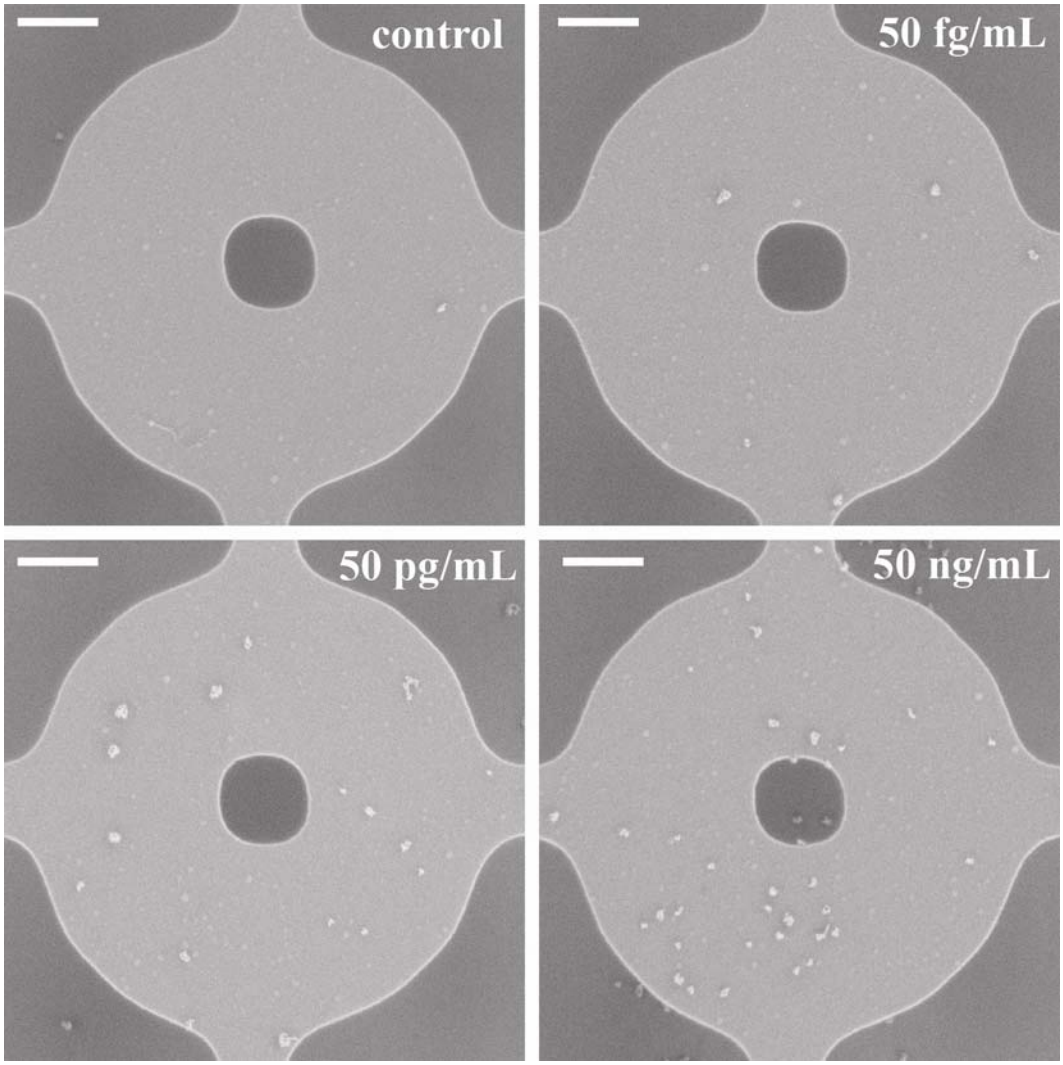

Figure 5-17. Representative SEM images of trampoline resonators showing that the number of nanoparticles bound to devices scales with PSA concentration. Scale bar represents 1 μm.

From the low binding densities of nanoparticles at these concentrations, it becomes evident that these trampoline resonators are more sensitive than previously used paddlever resonators. If the same nanoparticle binding density were present on the smaller paddlever devices, they would likely have fewer nanoparticles bound to them at such low PSA concentrations, resulting in a reduced detection limit even if they were of the same thickness. That said, the 90 nm thickness of silicon nitride improves sensitivity over previously 150 nm thick resonators. On the other hand, if a cantilever with the same surface area as the circular trampolines used in the present work, roughly the same number of nanoparticles would be bound to it, but the highly non-uniform frequency response of cantilevers along their length would likely increase the standard deviations for each concentration by a significant amount, also reducing sensitivity.

There are several ways in which the present assay could be improved. First, in order to achieve high quality factor resonances of the devices, all frequency measurements are taken in vacuum, which presents some challenges to use in a clinical laboratory setting. While it is unlikely that these nanomechanical resonant sensors and similar devices could be used with high sensitivity in liquid due to the very strong effects of viscous damping, it would be feasible with proper optimization to measure the resonant frequencies of some devices in air, where quality factors on the order of 100-1000 have been demonstrated,[48,49] including the work discussed in Section 4.4.2. In addition, the standard deviations shown in Figure 5-16, representing the device-to-device variability of the frequency shift, are affected by several factors, including nonspecific binding and the nature of nanoparticles used. For instance, the use of nanoparticles with reduced polydispersity would decrease the variations in frequency shift due to variable nanoparticle size and composition. In addition, further optimizing the blocking and washing protocols could improve the uniformity of the

assay and reduce the standard deviations. Also, device sensitivity may be improved by increasing the concentration of nanoparticles in order to increase the number bound for each PSA concentration using the same incubation time, as long as they do not nonspecific bind and increase the control frequency shifts proportionately.

REFERENCES

1. M. Varshney, P.S. Waggoner, C.P. Tan, K. Aubin, R.A. Montagna, and H.G. Craighead, "Prion Protein Detection Using Nanomechanical Resonator Arrays and Secondary Mass Labeling," *Anal. Chem.* **80** (2008) 2141-2148.

2. M. Varshney, P.S. Waggoner, R.A. Montagna, and H.G. Craighead, "Prion Protein Detection in Serum Using Micromechanical Resonator Arrays," *Talanta* **80** (2009) 593.

3. P.S. Waggoner, M. Varshney, and H.G. Craighead, "Detection of prostate specific antigen with nanomechanical resonators," *Lab Chip* **9** (2009) 3095-3099.

4. J. Fritz, M. K. Baller, H. P. Lang, H. Rothuizen, P. Vettiger, E. Meyer, H.-J. Güntherodt, Ch. Gerber, and J. K. Gimzewski, "Translating Biomolecular Recognition into Nanomechanics," *Science* **288** (200) 316.

5. A. Subramanian, P. I. Oden, S. J. Kennel, K. B. Jacobson, R. J. Warmack, T. Thundat, and M. J. Doktycz, "Glucose biosensing using an enzyme-coated microcantilever," *Appl. Phys. Lett.* **81**(2) (200) 385.

6. S.-J. Hyun, H.-S. Kim, Y.-J. Kim, and H.-I. Jung, "Mechanical detection of liposomes using piezoresistive cantilever," *Sens. Actuators, B* **117** (2006) 415.

7. C. A. Savran, S. M. Knudsen, A. D. Ellington, and S. R. Manalis, "Micromechanical Detection of Proteins Using Aptamer-based Receptor Molecules," *Anal. Chem*. **76**(11) (2004) 3194.

8. S. S. Iqbal, M. W. Mayo, J. G. Bruno, B. V. Bronk, C. A. Batt, and J. P. Chambers, "A review of molecular recognition technologies for detection of biological threat agents," *Biosens. Bioelectron*. **15** (2000) 549.

9. T. Braun, M. K. Ghatkesar, N. Backmann, W. Grange, P. Boulanger, L.Letellier, H.-P. Lang, A. Bietsch, C. Gerber, and M. Hegner, "Quantitative time-resolved measurement of membrane protein-ligand interactions using microcantilever array sensors," *Nature Nanotechnol.* **4** (2008) 179.

10. H. Xu, X. Zhao, C. Grant, J. R. Liu, D. E. Williams, and J. Penfold, "Orientation of a Monoclonal Antibody Adsorbed at the Solid/Solution Interface: A Combined Study Usign Atomic Force Microscopy and Neutron Reflectivity," *Langmuir* **22**(14) (2006) 6313.

11. B. Lu, M. R. Smyth, and R. O'Kennedy, "Oriented Immobilization of Antibodies and its Application in Immunoassays and Immunosensors," *Analyst* **121** (1996) 29R.

12. M. Friedel, A. Baumketner, and J.-E. Shea, "Effects of surface tethering on protein folding mechanisms," *Proc. Natl. Acad. Sci. USA* **103**(22) (2006) 8396.

13. R. A. Vijayendran and D. E. Leckband, "A Quantitative Assessment of Heterogeneity for Surface-Immobilized Proteins," *Anal. Chem*. **73**(3) (2001) 471.

14. G. Y. Kang, G. Y. Han, J. Y Kang, I.-H. Cho, H.-H. Park, S.-H. Paek, T. S. Kim, "Label-free protein assay with site-directly immobilized antibody using self-actuating PZT cantilever," *Sens. Actuators, B* **117** (2006) 332.

15. N. Backmann, C. Zahnd, F. Huber, A. Bietsch, A. Plückthun, H.-P. Lang, H.-J. Güntherodt, M. Hegner, and Ch. Gerber, "A label-free immunosensor array using single-chain antibody fragments," *Proc. Natl. Acad. Sci. USA* **102**(41) (2005) 14587.

16. P. Peluso, D. S. Wilson, D. Do, H. Tran, M. Venkatasubbaiah, D. Quincy, B. Heidecker, K. Poindexter, N. Tolani, M. Phelan, K. Witte, L. S. Jung, P. Wagner, and S. Nock, "Optimizing antibody immobilization strategies for the construction of protein microarrays," *Anal. Biochem*. **312** (2003) 113.

17. C. Wingren, C. Steinhauer, J. Ingvarsson, E. Persson, K. Larsson, and C. A. K. Borrebaeck, "Microarrays based on affinity-tagged single-chain Fv antibodies: Sensitive detection of analyte in complex proteomes," *Proteomics* **5** (2005) 1281.

18. H.-F. Ji, K. M. Hansen, Z. Hu, and T. Thundat, "Detection of pH variation using modified microcantilever sensors," *Sens. Actuators, B* **72** (2001) 233.

19. J. A. Howarter and J. P. Youngblood, "Optimization of Silica Silanization by 3-Aminopropyltriethoxysilane," *Langmuir* **22** (2006) 11142.

20. J. A. Henry, Y. Wang, and M. A. Hines, "Controlling energy dissipation and stability of micromechanical silicon resonators with self-assembled monolayers," *Appl. Phys. Lett.* **84**(10) (2004) 1765.

21. A. M. Richter, D. Sengupta, and M. A. Hines, "Effect of surface chemistry on mechanical energy dissipation: Silicon oxidation does not inherently decrease the quality factor," *J. Phys. Chem. C* **112** (2008) 1473.

22. M. Su, S. Li, and V. P. Dravid, "Microcantilever resonance-based DNA detection with nanoparticle probes," *Appl. Phys. Lett.* **82**(20) (2003) 3562.

23. S.B. Prusiner, "Novel proteinaceous infectious particles cause scrapie," *Science* **216** (1982) 136.

24. S. B. Prusiner, "Prion Diseases and the BSE Crisis," *Science* **278** (1997) 245.

25. C. Soto, "Diagnosing prion diseases: needs, challenges and hopes," *Nat. Rev. Microbiol*. **2** (2004) 809.

26. P. C. Lourenco, M. J. Schmerr, I. MacGregor, R. G. Will, J. W. Ironside, and M. W. Head, "Application of an immunocapillary electrophoresis assay to the detection of abnormal prion protein in brain, spleen and blood specimens from patients with variant Creutzfeldt–Jakob disease," *J. Gen. Virol*. **87** (2006) 3119.

27. A. Sakuda, I. Nakamura, K. Ikuta and T. Onodera, "Recent Developments in Prion Disease Research: Diagnostic Tools and In Vitro Cell Culture Models," *J. Vet. Med. Sci.* **69** (2007) 329.

28. N. Hunter, J. Foster, A. Chong, S. McCutcheon, D. Parnham, S. Eaton, C. MacKenzie and F. Houston, "Transmission of prion diseases by blood transfusion," *J. Gen. Virol.* **83** (2002) 2897.

29. P. Brown, "Blood infectivity, processing and screening tests in transmissible spongiform encephalopathy," *Vox Sang.* **89** (2005) 63.

30. F. Houston, J.D. Foster, A. Chong, N. Hunter and C.J. Bostock, "Transmission of BSE by blood transfusion in sheep," *Lancet* **356** (2000) 999.

31. P. Brown, L. Cervenakova and H. Diringer, "Blood infectivity and the prospects for a diagnostic screening test in Creutzfeldt-Jakob disease," *J. Lab. Clin. Med*. **137** (2001) 5.

32. C.A. Llewelyn, P.E. Hewitt, R.S. Knight, K. Amar, S. Cousens, J. Mackenzie and R.G. Will, "Possible transmission of variant Creutzfeldt-Jakob disease by blood transfusion," *Lancet* **363** (2004) 417.

33. A.H. Peden, M.W. Head, D.L. Ritchie, J.E. Bell and J.W. Ironside, "Preclinical vCJD after blood transfusion in a *PRNP* codon 129 heterozygous patient," *Lancet* **364** (2004) 527.

34. Q. Schiermeier, "Testing times for BSE," *Nature* **409** (2001) 658.

35. L. Ingrosso, V. Vetrugno, F. Cardone and M. Pocchiari, "Molecular diagnostics of transmissible spongiform encephalopathies," *Trends Mol. Med*. **8** (2002) 273.

36. P. Saa, J. Castilla and C. Soto, "Presymptomatic Detection of Prions in Blood," *Science* **313** (2006) 92.

37. L. Trieschmann, A.N. Santos, K. Kaschig, S. Torkler, E. Maas, H. Schatzl and G. Bohm, "Ultra-sensitive detection of prion protein fibrils by flow cytometry in blood from cattle affected with bovine spongiform encephalopathy," *BMC Biotechnol*. **5** (2005) 26.

38. P. Wu, H. Koistinen, P. Finne, W.-M. Zhang, L. Zhu, J. Leinonen, and U.-H. Stenman, "Advances in Prostate-Specific Antigen Testing," *Adv. Clin. Chem.* **41** (2006) 231.

39. S. P. Balk, Y.-J. Ko, and G. J. Bubley, "Biology of Prostate-Specific Antigen," *J. Clin. Oncology* **21**(2) (2003) 383.

40. W. J. Catalona, P. C. Southwick, K. M. Slawin, A. W. Partin, M. K. Brawer, R. C. Flanigan, A. Patel, J. P. Richie, P. C. Walsh, P. T. Scardino, P. H. Lange, G. H. Gasior, K. G. Loveland, and K. R. Bray, "Comparison of percent free PSA,

PSA density, and age-specific PSA cutoffs for prostate cancer detection and staging," *Urology* **56**(2) (2000) 255.

41. G. Wu, R. H. Datar, K. M. Hansen, T. Thundat, R. J. Cote, and A. Majumdar, "Bioassay of prostate-specific antigen (PSA) using microcantilevers," *Nat. Biotechnol*. **19** (2001) 856-860.

42. M. Yue, J. C. Stachowiak, H. Lin, R. Datar, R. Cote, and A. Majumdar, "Label-Free Protein Recognition Two-Dimensional Array Using Nanomechanical Sensors," *Nano Lett.* **8**(2) (2008) 520.

43. K. S. Hwang, J. H. Lee, J. Park, D. S. Yoon, J. H. Park, and T. S. Kim, "*In-situ* quantitative analysis of a prostate-specific antigen (PSA) using a nanomechanical PZT cantilever," *Lab Chip* **4** (2004) 547.

44. S. Lee, K. S. Hwang, H. Yoon, D. S. Yoon, S. K. Kim, Y. Lee, and T. S. Kim, "Sensitivity enhancement of a dynamic mode microcantilever by stress inducer and mass inducer to detect PSA at low picogram levels," *Lab Chip* **9** (2009) 2683.

45. M. J. Lachut and J. E. Sader, "Effect of Surface Stress on the Stiffness of Cantilever Plates," *Phys. Rev. Lett.* **99** (2007) 206102.

46. K. S. Hwang, H. K. Jeon, S.-M. Lee, S. K. Kim, and T. S. Kim, "Quantification of disease marker in undiluted serum using an actuating layer-embedded microcantilever," *J. Appl. Phys.* **105** (2009) 102017.

47. C. Vancura, Y. Li, J. Lichtenberg, K. Kirstein, and A. Hierlemann, "Liquid-Phase Chemical and Biochemical Detection Using Fully Integrated Magnetically Actuated Complementary Metal Oxide Semiconductor Resonant Cantilever Sensor Systems," *Anal. Chem.* **79** (2007) 1646.

48. J. W. M. Chon, P. Mulvaney, and J. E. Sader, "Experimental validation of theoretical models for the frequency response of atomic force microscope cantilever beams immersed in fluids," *J. Appl. Phys.* **87**(8) (2000) 3978.

49. J. F. Vignola, J. A. Judge, J. Jarzynski, M. Zalalutdinov, B. H. Houston, and J. W. Baldwin, "Effect of viscous loss on mechanical resonators designed for mass detection," *Appl. Phys. Lett.* **88** (2006) 041921.

CHAPTER 6

CONCLUSIONS AND FUTURE CHALLENGES

A key theme in this work is the behavior of resonant mechanical sensors used near the limits of their sensitivity. The high sensitivity regime is interesting and makes this technology appealing for novel applications and encourages its growth into the medicine and other fields. Because high sensitivity is synonymous with incomplete films and single or a handful of isolated binding events, stiffness effects should not arise, which simplifies the system. In addition, while the effect of surface stress on the resonant frequency of cantilevers is debatable and recent research has presented the most convincing arguments against it so far,[1,2] it remains that isolated binding events will not create a surface stress, even on doubly-clamped beams that may be better suited to detect surface stresses.[3] Therefore, as long as the thickness of captured analytes and biological coatings does not approach let alone exceed that of the resonator, mass should remain the dominant effect.

However, having mass changes as the dominant effect presents a problem in that the biomolecular masses are typically extremely small. This work has demonstrated a way around this that does not require chemical modification of the analyte and also inherently makes these assays more specific to the analyte. With the help of this secondary mass labeling procedure, detection of low concentrations of prion protein and prostate specific antigen were demonstrated not just from buffer but from undiluted fetal bovine serum, suggesting that these devices can handle real serum samples from patients.

Not only is this important, but take for instance the PSA sensitivity, demonstrated to be around or just under 50 fg/mL or 1.5 fM in Section 5.6.4—commercially available ELISA tests offer sensitivity to concentrations anywhere from

roughly 0.05 to 1 ng/mL. This opens the door to studying the onset or monitoring regression of prostate cancer, or any such disease (with an accepted biomarker) for that matter, because these cases often feature currently undetectable amounts of free PSA. With concentration sensitivity so low, it then becomes possible to watch the concentration either continue to go down, or possibly begin to increase again, giving a much earlier warning of the reappearance of cancer. Another potential advantage of such sensitivity is that the levels of PSA can be explored in other bodily fluids such as urine or saliva, which are less invasive to obtain as compared to blood samples.

In tethering relatively heavy nanoparticle masses to captured analyte, it became evident that the effect of binding location would become an important question. This was addressed experimentally and analytically, leading to some interesting insights into localized binding and how any type of resonant sensor should be designed. Perhaps the most interesting results from these investigations were that cantilevers are not always the most sensitive or repeatable devices to use either when random binding occurs or even in some cases of localized binding. Ideally, one would like a resonating device with completely uniform motion with minimal to no bending, though this is not realistic.

Featuring a large central paddle supported by four flexible supports, the trampoline-like resonators discussed throughout this work may very well be the closest one can come to such a device, especially as the ratio of center paddle area to support arm area increases. This must of course be balanced with stiction concerns that increase with thinner and more flexible supports. With more uniform responses to the mass binding as a function of position, the standard deviation of the frequency responses from an array of devices decreases as the effective noise of random binding is reduced. These trampoline resonators break the cantilever mold from which the vast majority of devices used in this field originate. While they are complex and hard

to analytically model, their behavior simplifies in situations where they are most useful, in the high sensitivity regime where analytes will be dilutely bound to the sensor and only change the device mass.

Despite the knowledge obtained about resonant micro- and nanomechanical sensors and their encouraging results in biosensing applications presented in this thesis, there are many challenges still facing this technology. The transition from research facility to clinical lab or even "the field" presents the most significant limitation. Common criticisms of the technique often aim at the optical bench with associated electronics or vacuum requirements.

Miniaturization of the excitation and readout system could conceivably be straightforward. Optical readout of the devices could essentially be carried out by a CD or DVD reader, which uses a diode laser and detector to quickly scan over discs, reading in reflectivity changes as data. With standardized chip sizes and device types, aligning to known positions of arrays should be within reason, and minimal electronics should be able to replace a spectrum analyzer since the frequency range of the particular resonator geometry used should be well known and characterized. The uniform excitation of all devices by a single piezoelectric element is also amenable to miniaturization and removes the problem of aligning a second, modulated excitation laser to the devices.

Typical operation in vacuum is another issue that must be addressed. There are two options which are both feasible. First, the vacuum chamber could be minimized such that only the smallest chamber surrounds it, allowing miniaturized vacuum pumps to pump out such small volumes quickly. From experience as well as the work discussed in Section 4.4.2, pressures below 1 mTorr show essentially no effects of viscous damping, while some higher modes (in-plane modes, for instance) preserve their vacuum quality factors up to nearly 1 Torr, which reduces the

constraints on vacuum pumps. The other possibility would be to take advantage of in-plane resonant modes and their relatively high quality factors in air, and use this advantage to measure them in air. One challenge here, however, is humidity control, because if the surfaces are hydrophilic they will adsorb water vapor depending on the relative humidity, which introduces another environmental variable to the system.

True utilization of the small-scale, resonator arrays in multiplexed, lab-on-a-chip detection schemes remains to be demonstrated. Several functionalization techniques are potential suitors, including microfluidic patterning using laminar flows to functionalize rows of arrays differently. Another possibility includes microarray spotting, although pin-tip spotters could potentially destroy devices with excessive physical contact. Inkjet printing is a promising technique that could be used to place droplets of solution on entire arrays and functionalize each one separately from its neighbor. These technologies would allow resonant sensors to approach the multiplexing levels of microarray technologies, however readout of arrays, even with the rapid automation developed in this work, is unlikely to compete with the speed of optical readout capabilities used typically with microarrays. However, they should make up for that with their sensitivity.

All things considered, micro- and nanomechanical resonant sensors are a promising technology with a great deal of potential. While the present work has shed light on the sensor design and especially their application as biosensors, further engineering and miniaturization is needed to decrease apparatus size and increase desirability and ease of use in clinical or commercial settings. Integration into "lab-on-a-chip" systems is within reach, and further breakthroughs in sensor design or resonant mode engineering may even allow devices to work within reason in fluidic environments. These devices are robust, have demonstrated high sensitivity, and are extremely versatile in terms of design parameters, actuation and detection

mechanisms, and especially in functionalization for use with any analyte of choice that specifically binds to some molecule or material. In today's sensor age, such qualities are highly valued and will likely lead to many exciting and revolutionary applications of this technology and make a significant impact in medicine, defense, and many other fields.

REFERENCES

1. M. J. Lachut and J. E. Sader, “Effect of Surface Stress on the Stiffness of Cantilever Plates,” *Phys. Rev. Lett.* **99** (2007) 206102.

2. M. J. Lachut and J. E. Sader, “Effect of surface stress on the stiffness of cantilever plates: Influence of cantilever geometry,” *Appl. Phys. Lett.* **95** (2009) 193505.

3. J. W. Ndieyira, M. Watari, A. D. Barrera, D. Zhou, M. Vogtli, M. Batchelor, M. A. Cooper, T. Strunz, M. A. Horton, C. Abell, T. Rayment, G. Aeppli and R. A. McKendry, “Nanomechanical detection of antibiotic-mucopeptide binding in a model for superbug drug resistance,” *Nat. Nanotechnol.* **3** (2008) 691–696.